

**Probing and Controlling Many-Body Interactions in a Simple  
Cubic Optical Lattice Clock**

by

**R. B. Hutson**

B.A., University of California, Berkeley, 2013

A thesis submitted to the  
Faculty of the Graduate School of the  
University of Colorado in partial fulfillment  
of the requirements for the degree of  
Doctor of Philosophy  
Department of Physics  
2023

Committee Members:

Jun Ye, Chair

Ana Maria Rey

James K. Thompson

Eric A. Cornell

Shi-Wei Huang

Hutson, R. B. (Ph.D., Physics)

Probing and Controlling Many-Body Interactions in a Simple Cubic Optical Lattice Clock

Thesis directed by Prof. Jun Ye

We describe recent developments in the operation of an optical atomic clock at unprecedentedly high atomic densities. Frequency measurements are performed primarily on a band-insulating quantum-degenerate Fermi-gas of neutral strontium-87 loaded into a three-dimensional optical lattice with a simple cubic geometry. Rapid production of such quantum states of matter are enabled by novel techniques in neutral atom cooling and trapping while precise frequency measurements rely on both state-of-the-art optical reference cavities and imaging techniques which significantly suppress residual laser phase noise. The observed frequency shifts about the mHz-wide clock transition are attributable to various many-body interactions involving Fermi-Hubbard physics and long-range interactions between electric dipoles. Using accurate models of the observed phenomena, we anticipate both challenging systematic effects and novel opportunities to generate spin-squeezed states in future generations of atomic clocks operating at similarly high atomic densities.

## Dedication

To my parents, Don and Karlene

## Contents

### Chapter

<b>1</b>	<b>Introduction</b>	<b>1</b>
1.1	What is a clock? It measures time! . . . . .	1
1.2	What even is time? It's what a clock measures! . . . . .	4
1.3	Simple cubic optical lattice clock . . . . .	4
<b>2</b>	<b>Making, probing, and understanding atomic clocks</b>	<b>7</b>
2.1	Discrete systems coupled to a continuum . . . . .	7
2.1.1	Interacting with the vacuum . . . . .	9
2.1.2	Atomic level structure of strontium-87 . . . . .	12
2.1.3	Interacting with coherent states of light . . . . .	17
2.2	Degenerate Fermi Gasses . . . . .	19
2.2.1	Phase-space densities . . . . .	20
2.2.2	Ultra-cold collisions . . . . .	21
2.3	Experimental procedure . . . . .	24
2.3.1	Hot atomic vapor . . . . .	24
2.3.2	Zeeman Slower . . . . .	27
2.3.3	Two-Dimensional Magneto-Optical Trap . . . . .	27
2.3.4	"Blue" MOT . . . . .	27
2.3.5	Far-off-resonant optical trapping . . . . .	29

2.3.6	Evaporative cooling . . . . .	33
2.3.7	Spin-state manipulation . . . . .	35
2.3.8	Optical lattices . . . . .	36
2.3.9	Clock spectroscopy . . . . .	42
2.3.10	Imaging spectroscopy . . . . .	45
<b>3</b>	<b>Spectroscopy of atomic collisions</b>	<b>49</b>
3.1	Theoretical background . . . . .	49
3.2	Effective Multi-body interactions . . . . .	52
3.3	Molecular three-body interactions . . . . .	58
<b>4</b>	<b>Engineering quantum states of matter</b>	<b>61</b>
4.1	Off-resonant two-photon scattering . . . . .	63
4.2	Motional dephasing in shallow lattices . . . . .	67
4.3	Accordion lattice . . . . .	67
4.3.1	Line pulling . . . . .	68
4.3.2	Collisional effects . . . . .	73
4.4	Alternative methods of reducing Raman scattering . . . . .	75
4.4.1	Blue-detuned lattice . . . . .	75
4.4.2	Floquet Engineering . . . . .	75
4.4.3	Accelerated lattice . . . . .	76
<b>5</b>	<b>Resonant Dipole-Dipole Interactions</b>	<b>77</b>
5.1	Theoretical background . . . . .	78
5.1.1	Classical Electric Field of Oscillating Point Dipole . . . . .	78
5.1.2	Interactions Between Classical Oscillating Point Dipoles . . . . .	79
5.1.3	Interactions Between quantum Dipoles . . . . .	81
5.1.4	First-order time-expansion of resonant dipole-dipole dynamics . . . . .	83

5.1.5	Resonant dipole-dipole interactions in a Ramsey interferometer . . . . .	85
5.1.6	Bragg enhancement of cooperative Lamb shifts . . . . .	88
5.2	Measurement of cooperative Lamb shifts . . . . .	88
5.2.1	Analysis of results . . . . .	88
5.3	Future directions . . . . .	92
<b>6</b>	<b>Conclusion</b>	<b>95</b>
	<b>Bibliography</b>	<b>101</b>
	<b>Appendix</b>	
<b>A</b>	<b>Symbolic conventions</b>	<b>107</b>
<b>B</b>	<b>Heating processes in optical traps</b>	<b>108</b>
B.0.1	Time Dependent Perturbation Theory . . . . .	108
B.0.2	Sinusoidal Potential . . . . .	110
B.0.3	The Harmonic Limit . . . . .	111

## Tables

### Table

2.1	Line strengths for $5s5s\ ^1S_0$ polarizability calculation. . . . .	29
2.2	Line strengths for $5s5p\ ^3P_0$ polarizability calculation. . . . .	29
2.3	Line strengths for $5s5p\ ^3P_1$ polarizability calculation. . . . .	31
3.1	Clock-state $s$ -wave scattering lengths. . . . .	52
3.2	Molecular loss rates . . . . .	60
A.1	Definitions of symbols. . . . .	107

## Figures

### Figure

1.1	Clock accuracy over the last millenium . . . . .	2
1.2	Simple cubic optical lattice clock. . . . .	5
1.3	Relative magnitudes of systematic clock shifts in a strontium-87 optical lattice clock. . . . .	6
2.1	Fine-structure energy-levels in neutral strontium. . . . .	15
2.2	Fine-structure energy-levels in neutral strontium-87. . . . .	16
2.3	Absorption imaging schematic. . . . .	18
2.4	Comparison of $s$ -wave interaction eigenstates. . . . .	23
2.5	Vacuum chamber schematic . . . . .	25
2.6	Laser layout: 650 THz. . . . .	26
2.7	Laser layout: 435 THz. . . . .	28
2.8	Ac polarizabilities for the $5s5s\ ^1S_0 \leftrightarrow 5s5p\ ^3P_1$ narrow-line cooling transition . . . . .	30
2.9	Laser layout: 282 THz. . . . .	32
2.10	Degenerate Fermi gas with ten spin components in time-of-flight. . . . .	34
2.11	Degenerate Fermi gas with a single spin components in time-of-flight. . . . .	35
2.12	Clock state polarizabilities . . . . .	36
2.13	Diagonalization of one-dimensional cosine lattice potential. . . . .	38
2.14	Lattice loading. . . . .	39
2.15	Lattice laser layout. . . . .	39

2.16	Band insulator density distribution. . . . .	40
2.17	Clock laser layout. . . . .	42
2.18	Rabi “flop” and quantum projection noise calibration. . . . .	44
2.19	Rabi linescan. . . . .	44
2.20	Ramsey linescans. . . . .	45
2.21	Imaging clock signals. . . . .	46
2.22	Imaging Ramsey and Rabi linescans. . . . .	46
2.23	Imaging differential ac Stark shifts. . . . .	47
2.24	Imaging differential clock shifts. . . . .	48
3.1	Doublon $s$ -wave collisional shifts. . . . .	51
3.2	$s$ -wave interaction energies for two atoms in a three-dimensional harmonic oscillator. . . . .	53
3.3	Multibody interaction spectrum . . . . .	54
3.4	Multibody shifts vs. $V_c$ . . . . .	56
3.5	Multibody shifts vs. $n$ . . . . .	57
3.6	Schematic for multibody lifetime measurements . . . . .	58
3.7	Determination of Molecular loss rates for multibody states. . . . .	59
4.1	Raman scattering of optical lattice photons . . . . .	62
4.2	Raman scattering rates out of $5s5p^3P_0$ vs. lattice wavelength . . . . .	64
4.3	Population dynamics due to Raman scattering . . . . .	66
4.4	Schematic of accordian optical lattice . . . . .	68
4.5	Hubbard parameters in a $3 \times \bar{V}_c = 12$ cubic accordian lattice . . . . .	69
4.6	Single particle energy spectrum in a in a $\bar{V}_c = 4$ one-dimensional accordian lattice . . . . .	70
4.7	Single atom Rabi couplings in a in a $\bar{V}_c = 4$ one-dimensional accordian lattice . . . . .	71
4.8	Upper bounds on line-pulling clock shifts in a $\bar{V}_c = 4$ one-dimensional accordian lattice . . . . .	72
4.9	Two-atoms in a double-well potential . . . . .	74

5.1	Resonant dipole-dipole interaction parameters . . . . .	80
5.2	Full-state time-evolution for nearest-neighbor, spin- $\frac{1}{2}$ , resonant dipole-dipole interactions in a qubic lattice . . . . .	82
5.3	Modeling spatial signal of cooperative Lamb shifts. . . . .	84
5.4	Scaling of cloud-averaged cooperative Lamb shift with system size. . . . .	89
5.5	Experimental parameters for measuring cooperative Lamb shifts . . . . .	90
5.6	Imaging cooperative Lamb shifts . . . . .	91
5.7	Controlling cooperative Lamb shifts. . . . .	93
5.8	Instability of cooperative Lamb shift measurement. . . . .	93
5.9	Enhancing resonant dipole-dipole interactions. . . . .	94
6.1	Zeroing leading order cooperative Lamb shifts in cubic “Bragg” lattice . . . . .	97
6.2	Van der Waals interaction energies at finite inter-atomic separation . . . . .	99
B.1	Intensity noise-induced heating . . . . .	109
B.2	Intensity noise-induced heating . . . . .	109

## Chapter 1

### Introduction

#### 1.1 What is a clock? It measures time!

Any clock can be considered as a device that measures the amount of elapsed time. For instance, if an observer  $A$  watches a pendulum oscillating at some frequency  $\nu$  then the time-interval  $\Delta t_{ji} = t_j - t_i$  between two events  $i$  and  $j$  may be determined by counting the number of oscillations  $N_{ji}$  occurring between the two events using the relation  $\Delta t_{ji} = N_{ji}/\nu$ . Of course, if two observers  $A$  and  $B$  with separate clocks wish to agree on the amount of elapsed time then the ratio of oscillation periods  $\nu_A/\nu_B$  must be well characterized. For an individual clock the relevant, dimensionless parameter for a clock's accuracy is then  $\delta\nu/\nu$ .

Prior to the twentieth century, all man-made clocks were less accurate than what can be achieved via astronomical observation, that is the sidereal day most stable oscillator limited by fluctuations in earth's rate of rotation to  $\delta\nu/\nu \approx 6 \times 10^{-8}$ . Nonetheless, mechanical clocks are of practical use, as evidenced by Fig. 1.1 which displays improvements in clock accuracy throughout the last millenium.

The most accurate mechanical clocks were produced in the early-mid 20<sup>th</sup> century, with fractional accuracies approaching the  $10^{-9}$  level [11]. The problem with such devices is that their oscillation frequencies are not constants of nature, *e.g* a pendulum's oscillation frequency depends on its length  $l$  and the local acceleration due to gravity  $g$  as  $\nu = \sqrt{g/l}/2\pi$ . If an experimenter, Alice, wished to communicate the results of an experiment which depends on the amount of elapsed time to another experimenter located at some far-away place, Bob, she would have no way of accurately communicating the oscillation period of her clock, without physically sending a length standard defining the physical dimensions of her

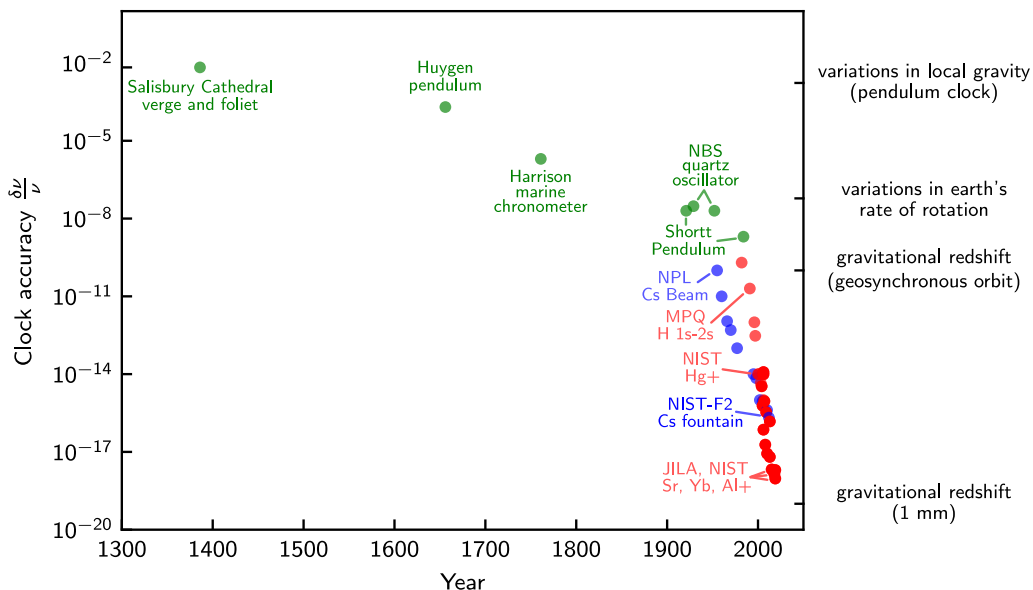


Figure 1.1: Clock accuracy over the last millenium, starting, with the oldest surviving mechanical clock up through the best modern atomic clocks. Mechanical devices are plotted in green, microwave atomic clocks in blue, and optical atomic clocks in red. One notices roughly exponential improvement in clock accuracy throughout each era, and an increasing time constants between each era. Data adapted from Refs. [1–10]

pendulum, and her local gravitational potential.

This was noted as early as the nineteenth century by James Clerk Maxwell [12], who then suggested that such issues can be avoided by using atoms to define oscillation period of a clock. The key insight is that all atoms of a given atomic species are identical and that the internal states of an atom are coupled to the electromagnetic field whereby the frequency of electromagnetic radiation that connects two internal levels of an atom can then be used as a clock's oscillator. In this way, the units with which time is measured can then be defined by purely non-physical means. Alice no longer needs to send Bob a physical copy of her pendulum, and instead can simply tell Bob to use the radiation emitted from, e.g. any neutral atom with 38 electrons and 87 nuclei.

Though this does not fully specify the unit of time. A Hydrogen atom in the Sun's core does not emit radiation at exactly the same frequency as a Hydrogen atom on earth. Atoms are still sensitive to external perturbations from electromagnetic fields. How then should Alice specify the ideal environment

of an atomic frequency reference? Perhaps Hans Dehmelt put it best,

*A Single Atomic Particle Forever Floating at Rest in Free Space* — Hans Dehmelt,  
1988 [13]

This leaves very little ambiguity as to how Alice defines her unit of time, but no such thing exists! The universe is full of “stuff” that is never infinitely far away from an experimenter’s atomic frequency reference, but Dehmelt’s ideal atom is still a useful notion for frequency metrologists. One never measures the true atomic resonance directly but rather assigns corrections to the measured resonance frequency and accordingly corrects the integrated time.

But this is only half the story. As will be described in more detail in Ch. 2, the quantized energy levels which make atoms such great frequency references also contribute a fundamental noise term which for a single atom can be given as

$$\frac{\delta\nu}{\nu} = \frac{1}{2\pi\nu\tau} \quad (1.1)$$

where  $\tau$  is the coherent interrogation period [14]. This then places one at a cross-roads. On one hand, simultaneously probing multiple atoms increases the rate at which frequency measurements can be made, while on the other, the presence of multiple atoms is a perturbation on top of the ideal single atom at rest in free space. These conflicting ideas have led to a rich history in the development of modern atomic clocks.

Enabled by the pioneering work of by Isidor Rabi, Norman Ramsey, and collaborators [15] in atomic beam-line microwave spectroscopy, the first atomic clock was constructed in 1955 at the National Physical Laboratory [2], claiming an accuracy of  $\delta\nu/\nu = 10^{-9}$ . The development of laser cooling dramatically enhanced achievable interaction times from  $\mathcal{O}(10 \text{ ms})$  to  $\mathcal{O}(1 \text{ s})$  [16], and correspondingly improved achievable accuracies [17, 18].

Further improvements in the accuracy of atomic clocks was spurred by advances in laser technology [19, 20], where the denominator in Eq. 1.1 could be increased by nearly  $10^5$  in *optical atomic clocks*.

## 1.2 What even is time? It's what a clock measures!

Thus far we treated time as some parameter in our equations of motion, but what does it represent? There quite some merit in taking a pragmatic approach in saying that time is whatever an *ideal* clock measures. Alice and Bob never actually directly observed time as a physical quantity, they simply measured the state of the pendulum and inferred what the parameter  $\bar{t}$  had to have been.

What good then is inferring the value of a non-physical quantity? Despite time being intangible, it is ubiquitous in physical descriptions of nature, from quantum mechanics to general relativity. Building better and better atomic clocks then allows one to test how good of a parameter time really is. It is a well known result from special and general relativity that time, as measured by a clock is not a global parameter of the universe, rather it depends on an observers frame of reference. Atomic clocks have enabled verification of these effects, beginning with the Hafele and Keating experiment in 1972 which observed relativistic time-dilation by flying around the world with commercial Cs beam clocks[21]. More recently, atomic clocks have been able to detect gravitational time-dilation on 1 m - 1 mm length scales [22, 23]. Given atomic clocks allow us to measure time to unprecedented and ever-increasing accuracies one expects tests of the fundamental laws of physics on ever finer timescales.

## 1.3 Simple cubic optical lattice clock

Being motivated by improving tests of fundamental physics, or more generally by the question “to how many significant digits can one measure a physical quantity?”, this thesis describes the development of an optical atomic clock which traps  $10 - 100 \times 10^3$  strontium-87 atoms in a cubic optical lattice (see Fig. 1.2) in an attempt to simultaneously probe as many-atoms as possible while also attempting to maintain Dehmelt's notion of an ideal atomic frequency reference.

In Ch. 2 we will provide a theoretical and technical foundation for understanding the basic principles of light-matter interactions and the operation of atomic clocks. We will describe how a neutral gas of fermionic atoms can be cooled into quantum degeneracy such that they naturally subside on individual lattice sites of the optical lattice, and how spatially resolved measurements of local frequency shifts can be

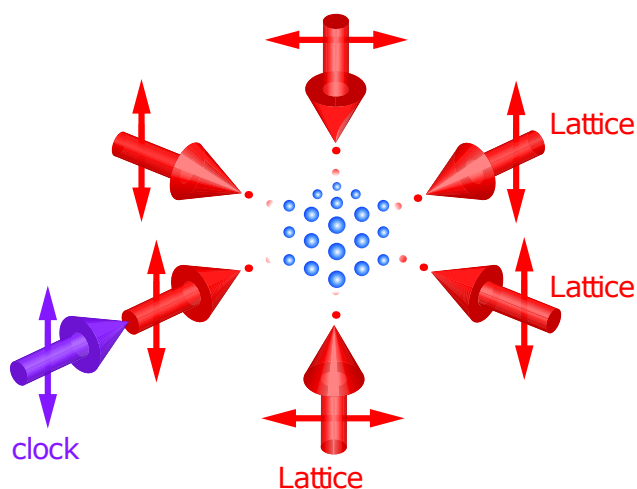


Figure 1.2: Simple cubic optical lattice clock. Atoms are trapped on individual lattice sites of a simple cubic optical lattice. Despite the relatively high atomic density  $n_0 \sim 10^{19} \text{ m}^{-3}$ , individual atoms are tightly confined such that their wave-packets do not overlap.

made using a high-resolution imaging objective. The highly ordered arrangement and tight confinement of atoms eliminates collisional interactions between lattice sites, an effect which has significantly affected previous atomic clocks operating with multiple neutral atoms [24–27].

In Ch. 3 we discuss further measurements involving ultra-cold collisions when multiple atoms are intentionally loaded into the same lattice site, allowing for the precise characterization of all interaction parameters.

In Ch. 4 we describe how Spontaneous Raman scattering of optical lattice photons produces a tradeoff between achievable optical coherence times and tunneling induced dephasing. We then use our quantitative understanding of these effects to propose alternative lattice geometries which are expected to enable coherent interrogation times approaching that of the 120 s natural lifetime of strontium-87 [28].

The unprecedentedly high density however, is shown to significantly enhance a new systematic effect, the Cooperative Lamb shift, as described in Ch. 5. We have been able to demonstrate a quantitative understanding of this effect in geometries which enhance clock shifts, while also show that they may be suppressed to below experimental detectability when more conventional spectroscopic methods are used. Nonetheless, these interactions pose an interesting question, what is the ultimate limit to how dense an atomic gas can be made before it stops acting as individual atoms infinitely far apart? While it is hard

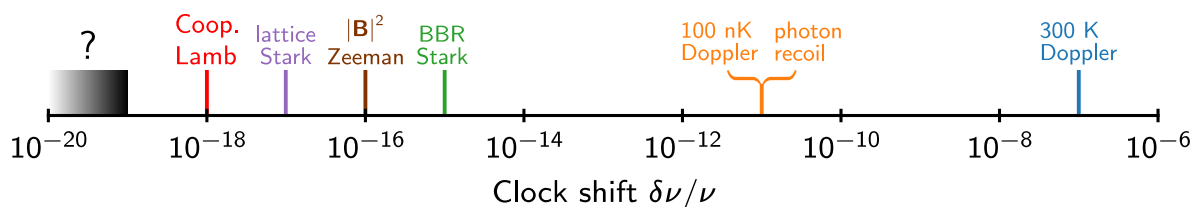


Figure 1.3: Relative magnitudes of systematic clock shifts in a strontium-87 optical lattice clock. The motional shifts (Doppler and photon recoil) are negated by trapping atoms in a deep optical lattice. The largest correction comes from the presence of photons in a room temperature black-body radiation (BBR) environment [29] A finite magnetic bias field is required to resolve individual hyperfine transitions in the clock state manifold such that even after averaging over transitions with opposite linear sensitivities ( $\delta\nu \propto \pm|\mathbf{B}|$ ) a residual shift proportional to  $|\mathbf{B}|^2$  on the order of  $\delta\nu/\nu \approx 10^{-16}$  remains. The optical frequency of the trapping potential is chosen to minimize the differential shift between clock states at the operational trap depth, extrapolating to zero trap depth requires a correction on the order of  $10^{-18}$  [30]

to make a more general statement, it does appear that, given a finite electromagnetic coupling strength between levels in an ensemble of two-level systems, there will be some limit to the maximum allowed density, given a desired limit to the associated clock shifts. Fig. 1.3 summarizes the approximate magnitudes of systematic clock shifts in a strontium-87 three-dimensional optical lattice clock, emphasizing that understanding cooperative Lamb shifts will be essential to pushing total systematic uncertainties below the  $10^{-18}$ -level.

The concluding remarks in Ch. 6 then discuss what can be done in the design of future clock experiments to diminish the effects of cooperative Lamb shifts, and alternatively what new physics can be studied in the context of many-body physics.

## Chapter 2

### Making, probing, and understanding atomic clocks

In this chapter we will lay the foundation for the experimental results in the following chapters. We begin with a general overview of atom-light interactions, describing how light can be used to precisely manipulate and extract information from atoms. We will then technically specify how this is done in the lab, starting with a chunk of metallic strontium to imaging spatially resolved frequency measurements, and refer the reader to Refs. [31–36] for additional details of the apparatus. A table summarizing the symbolic conventions used in this thesis is available in Appendix A.

#### 2.1 Discrete systems coupled to a continuum

As we discussed in the first chapter, an atom exhibits discrete energy levels  $i \in \{1, 2, \dots\}$  between which transitions can be mediated by the electromagnetic environment, which, in free space, contains a continuum of modes  $p \in [0, \infty)$ . In this section, we will emphasize how well known phenomena in the context of atomic physics, specifically *spontaneous emission* and *Lamb shifts*, are generic features of discrete systems coupled to a continuum of modes. While this firstly allows us to state useful formulae which we will refer to throughout this thesis, in Ch. 5 we will discuss multiple discrete-leveled systems interacting with a shared continuum of modes and see how spontaneous emission and Lamb shifts become *cooperative* effects, that is the dynamical evolution can not be treated as that of independent systems. In this way, we aim for some understanding of the fundamental limit to “how many ideal clocks can operate in a given volume of space?”

We begin by defining operators for the total system's energy  $\hat{H}_0$ , and momentum  $\hat{\mathbf{K}}_0$  as

$$\hat{H}_0 = \sum_i \omega_i \hat{P}_i + \sum_p \omega_p \hat{N}_p \quad \text{and} \quad \hat{\mathbf{K}}_0 = \sum_i \mathbf{k}_i \hat{P}_i + \sum_p \mathbf{k}_p \hat{N}_p, \quad (2.1)$$

where  $\omega_i$ ,  $\mathbf{k}_i$ , and  $\hat{P}_i$  are the energy, momentum, and projection operator corresponding to the  $i$ -th atomic state and  $\omega_p$ ,  $\mathbf{k}_p$ , and  $\hat{N}_p$  are the energy, momentum and number operator for the  $p$ -th photonic mode, respectively. For the system to preserve both energy and momentum, the Heisenberg-von Neumann equation then gives the time and position dependence of generic operators  $\hat{O}$  as

$$\frac{d}{dt} \hat{O} = \bar{\mathcal{H}}(\hat{H}_0 \hat{O}) + \frac{\partial}{\partial t} \hat{O} \quad \text{and} \quad \frac{d}{d\mathbf{r}} \hat{O} = \bar{\mathcal{H}}(\mathbf{K}_0 \hat{O}) + \frac{\partial}{\partial \mathbf{r}} \hat{O}, \quad (2.2)$$

where  $\bar{\mathcal{H}}(\hat{Q}) = i\hat{Q} + \text{H.c.}$  is  $i$  times the commutator when  $\hat{Q}$  is the product of two Hermitian operators<sup>1</sup>. These relations lead to trivial dynamics in the sense that atomic observables never depend on the photonic state, and *vice versa*. In describing generic interactions between the subsystems, we may form a power series in the creation  $\hat{C}_i^+$  ( $\hat{A}_p^+$ ) and annihilation  $\hat{C}_i^-$  ( $\hat{A}_p^-$ ) operators for an atom (photon) in state  $i$  ( $p$ ):

$$\hat{H}_{\text{int}} = \sum_i \sum_p g_{i,p} \hat{X}_i \hat{X}_p + \sum_{ij} \sum_p g_{ij,p} \hat{X}_{ij} \hat{X}_p + \sum_i \sum_{qp} g_{i,qp} \hat{X}_i \hat{X}_{qp} + \sum_{ij} \sum_{qp} g_{ij,qp} \hat{X}_{ij} \hat{X}_{qp} + \dots$$

where the operators

$$\begin{aligned} \hat{X}_i &= \mathcal{H}(\zeta_i \hat{C}_i^+), & \hat{X}_{ij} &= \mathcal{H}(\zeta_{ij} \hat{C}_i^+ \hat{C}_j^-), & \dots, \\ \hat{X}_p &= \mathcal{H}(\zeta_p \hat{A}_p^+), & \hat{X}_{qp} &= \mathcal{H}(\zeta_{qp} \hat{A}_p^+ \hat{A}_q^-), & \dots, \end{aligned} \quad (2.3)$$

where  $\mathcal{H}(Q) = Q + \text{H.c.}$  is the anti-commutator when  $\hat{Q}$  is the product of two Hermitian operators, emphasizing the coupling is between observable properties of either subsystem. The real numbers  $g$  characterize the coupling strengths, and the complex numbers  $\zeta$  are phase-factors<sup>2</sup> satisfying  $|\zeta|^2 = 1$ . Constraining our interaction to be perturbative  $\langle \hat{H}_{\text{int}} \rangle \ll \langle \hat{H}_0 \rangle$  and preserve the number of electrons  $\frac{d}{dt} \hat{C}_i^+ \hat{C}_i^- = \bar{\mathcal{H}}(\hat{C}_i^+ \hat{C}_i^- \hat{H}_{\text{int}}) = 0$ , we keep only the lowest order term which preserves electron number:

<sup>1</sup> This somewhat unconventional notation ensures all operators  $\bar{\mathcal{H}}(\hat{Q})$  are Hermitian without having to write "... + H.c." everywhere

<sup>2</sup> The phase factors  $\zeta$  could alternatively be absorbed into the operators  $\hat{C}_i^\pm$ ,  $\hat{A}_p^\pm$ , though the above construction will prove to be convenient in later analysis when separating "fast" and "slow" timescales.

$\hat{H}_1 \equiv \sum_{ij} \sum_p g_{ij,p} \hat{X}_{ij} \hat{X}_p$ . We may additionally determine the time and spatial dependencies of  $\hat{H}_1$  by requiring  $\frac{\partial}{\partial t} \hat{H}_1 = \bar{\mathcal{H}}(\hat{H}_1 \hat{H}_0)$ , and  $\frac{\partial}{\partial \mathbf{r}} \hat{H}_1 = \bar{\mathcal{H}}(\hat{H}_1 \hat{\mathbf{K}}_0)$  and solving the resulting partial differential equations for the quantities  $\zeta_{ij}$  and  $\zeta_p$ , term-by-term, in the sum over  $i$ ,  $j$ , and  $p$ . We then ensure spherical symmetry of the couplings by decomposing into spherical tensors, and thus obtain

$$\hat{H}_1(t) = \sum_{ij} \sum_p g_{ij,p} \zeta_{ij,p} \hat{S}_{ij} \hat{A}_p^+ + \text{H.c.} \quad (2.4)$$

where

$$\zeta_{ij,p} \equiv \prod_{\mu \in \{i,j,p\}} e^{i(\mathbf{k}_\mu \cdot \mathbf{r} - \omega_\mu t)}, \quad \hat{S}_{ij} \equiv \hat{C}_i^+ \hat{C}_j^- \quad \text{and} \quad g_{ij,p} \equiv d_{ij} E_p T_{ij,p}$$

Where  $d_{ij}$  and  $E_p$  are coupling strengths independent of their spatial orientations, we will refer to these as the electric dipole moment and electric field, respectively, although the above arguments apply more generally. The factor  $T_{ij,p}$ , satisfying  $\sum_{i, \hat{\mathbf{e}}_p} T_{ij,p} = \sum_{j, \hat{\mathbf{e}}_p} T_{ij,p} = 1$ , is a spherical tensor adding the photon's angular momentum to that of the atoms initial electronic state  $i$  to obtain the final electronic state  $j$ .

### 2.1.1 Interacting with the vacuum

There are a few key properties resulting from the coupling in Eq. 2.4 worth discussing for the vacuum state initial condition  $\langle \hat{N}_p \rangle = \langle \hat{A}_p^+ \hat{A}_p^- \rangle = 0$ . Time evolution under Eq. 2.2 produces *spontaneous emission* whereby electronic states  $\hat{P}_e$  emit a photon when decaying to states  $\hat{P}_g$  satisfying  $\omega_e > \omega_g$ , and additionally contributes a photon-number-preserving *Lamb shift* which renormalizes the atomic energy spectrum  $\omega_j$ . In future sections, accounting for spontaneous emission will be crucial for extracting information of atomic states while the Lamb shifts will simply be absorbed into the uncoupled Hamiltonian in Eq. 2.1. In Ch. 5 we will consider multiple atoms interacting with the photonic vacuum where cooperative analogues of these effects will be shown to be observable.

### 2.1.1.1 Spontaneous emission

The photonic number operator for the  $p^{\text{th}}$  mode evolves according to We may compute dynamics of the photonic number operator with respect to  $\hat{H}_1$  as

$$\frac{d}{dt}\hat{N}_p = \bar{\mathcal{H}}(\hat{H}_1\hat{N}_p) = - \sum_{ij} g_{ij,p} \bar{\mathcal{H}}(\zeta_{ij,p} \hat{S}_{ij} \hat{A}_p^+) \quad (2.5)$$

whose expectation value is initially zero given the vacuum initial condition  $\langle \hat{N}_p(t_0) \rangle = 0$ . To second order in  $\hat{H}_1$ , we obtain the following drive terms

$$\begin{aligned} \frac{d}{dt} \bar{\mathcal{H}}(\hat{H}_1\hat{N}_p) &= \sum_{imj} g_{mi,p} g_{mj,q} \mathcal{H}(\zeta_{ij} \hat{S}_{ij}) \mathcal{H}(\zeta_p \hat{A}_p^+) \mathcal{H}(\zeta_q \hat{A}_q^+) \\ &= \sum_{imj} \sum_p g_{mi,p} g_{mj,p} \mathcal{H}(\zeta_{ij} \hat{S}_{ij}) \quad \text{for } \langle \hat{N}_p \rangle = 0 \end{aligned} \quad (2.6)$$

which are non-zero for  $\langle \hat{S}_{ij}(t_0) \rangle \neq 0$ , and have explicit spatio-temporal oscillations at differences of transition energies  $\omega_{ij}$  and wave-vectors  $\mathbf{k}_{ij}$ . Our prior assumption in deriving Eq. 2.4 that the two systems are weakly coupled,  $\langle \hat{H}_1 \rangle \ll \langle \hat{H}_0 \rangle$  amounts to requiring  $g_{ij,p} \ll \omega_{ij}$ , in which case, the time-scale  $\tau_g \sim 2\pi/g_{ij,p}$  over which all meaningful changes in observables occur should be long compared to the time-scale  $\tau_\omega \sim 2\pi/\omega_{ij}$  associated with the explicit time-dependence of the drive term. We thus define the coarse-graining operation  $\mathcal{T}$

$$\mathcal{T}[\hat{H}(t)] \equiv \int_{\tau}^0 dt' \hat{H}(t-t') \quad (2.7)$$

such that we may approximate

$$\frac{d}{dt} \hat{O} = \mathcal{T} \left[ \frac{d}{dt} \bar{\mathcal{H}}(\hat{H}_n \hat{O}) \right] \approx \mathcal{H}[\mathcal{T}(\hat{H}_n) \hat{O} \hat{H}_n] - \mathcal{H}[\mathcal{T}(\hat{H}_n) \hat{H}_n \hat{O}] \equiv \mathcal{G}_n(\hat{O}) \quad (2.8)$$

when

$$\frac{d}{dt} \langle \bar{\mathcal{H}}(\hat{H}_n \hat{O}) \rangle \ll \frac{d}{dt} \langle \hat{H}_n \rangle$$

as our coarse-grained equation of motion.

In many instances the operation  $\mathcal{T}(\hat{H}_n)$  converges quickly, as compared to changes in the observable  $\hat{O}$ , such that the upper limit of the integral can be formally extended to all times  $\tau \rightarrow \infty$ . Subsequently taking the free-space limit,  $\omega_{ij,p} \gg \omega_V$  where  $\omega_V$  is the lowest allowable photon energy of the sum over

photonic degrees of freedom completes the so-called *Born-Markov* approximation where the following identities can be used

$$\sum_p \rightarrow \int \mathcal{D}_p \equiv \frac{1}{8\omega_V^3} \int_{\omega_V}^{\omega_\Lambda} d\omega_p \omega_p^2 \int_{\hat{\mathbf{e}}_p \perp \hat{\mathbf{k}}_p} d^2 \hat{\mathbf{k}}_p \sum_{\hat{\mathbf{e}}_p \perp \hat{\mathbf{k}}_p}, \quad (2.9)$$

$$\mathcal{T}(\zeta_{ij,p}) = \zeta_{ij,p} \frac{\sin(\omega_{ij,p}\tau) + i[\cos(\omega_{ij,p}\tau) - 1]}{\omega_{ij,p}} \rightarrow \zeta_{ij,p} \left[ \pi \delta(\omega_{ij,p}) - i\mathcal{P} \frac{1}{\omega_{ij,p}} \right].$$

Here,  $\delta$  is the Dirac delta function,  $\mathcal{P}$  denotes taking the Cauchy principal value in the integral over  $\omega_p$ , and  $\omega_\Lambda$  is a high-frequency cutoff above which our perturbative expansion in Eq. 2.3 is invalid. The normalization constant given in the continuum limit of the sum over photonic modes is chosen such that there are  $(\pi/3)(\omega_\Lambda/\omega_V)^3$  modes with energy  $\omega_p \leq \omega_\Lambda$  in a (real space) spherical quantization volume of radius  $\pi c/\omega_V$ .

We finally arrive at the following expression for  $\mathcal{G}_1$ ,

$$\mathcal{G}_1(\hat{O}) = \sum_{imj} \sum_{pq} \pi \delta(\omega_{im,p}) g_{im,p} g_{mj,q} \{ \mathcal{H}(\hat{X}_{im,p} \hat{O} \hat{X}_{mj,q}) - \delta_{mn} \mathcal{H}[\hat{X}_{imj,pq} \hat{O}] \} \quad \text{for } \langle \hat{N}_p \rangle = 0. \quad (2.10)$$

Returning to our discussion of the intensity of the emitted radiation, we now have

$$\begin{aligned} \frac{d}{dt} \hat{N}_p &\approx \mathcal{G}_1(\hat{N}_p) \\ &= \sum_{imj} 2\pi g_{im,p} g_{mj,p} \delta(\omega_{im,p}) \mathcal{H}(\zeta_{ij} \hat{S}_{ij}) \mathcal{H}(\zeta_p \hat{A}_p^+) \mathcal{H}(\zeta_p \hat{A}_p^+) \\ &= \sum_{ij} 2\pi g_{ij,p}^2 \delta(\omega_{ij,p}) \hat{P}_i \quad \text{for } \langle \hat{S}_{ij} \rangle = \delta_{ij} \langle \hat{P}_i \rangle \quad \text{and} \quad \langle \hat{N}_p \rangle = 0 \end{aligned} \quad (2.11)$$

Similarly, for the atomic populations  $\hat{P}_i$ , we have

$$\begin{aligned} \frac{d}{dt} \hat{P}_i &\approx \mathcal{G}_1(\hat{P}_i) \\ &= \sum_{mj} \sum_p \pi [g_{ji,p} g_{im,p} \delta(\omega_{ji,p}) \mathcal{H}(\zeta_{ji}^* \zeta_{im} \hat{S}_{jm}) - g_{jm,p} g_{mi,p} \delta(\omega_{jm,p}) \mathcal{H}(\zeta_{jm}^* \zeta_{mi} \hat{S}_{ji})] \\ &= \sum_j \gamma_{ij} [\Theta(\omega_{ji}) \hat{S}_{jj} - \Theta(\omega_{ij}) \hat{S}_{ii}] \quad \text{for } \langle \hat{S}_{mn} \rangle = \delta_{mn} \langle \hat{P}_m \rangle \quad \text{and} \quad \langle \hat{N}_p \rangle = 0 \end{aligned} \quad (2.12)$$

where

$$\gamma_{ij} \equiv \frac{2\pi^2 \omega_{ij}^3 g_{ij,p}^2}{3 \omega_V^3 \omega_p}$$

is the spontaneous emission rate, and  $\Theta$  is the Heaviside step function<sup>3</sup>.

<sup>3</sup> In this derivation, there is some ambiguity in which factor  $\times$  in the expression  $(|\omega_{ij}|/\omega_p)^\times | \omega_p = |\omega_{ij}|$  to take in decomposing  $g_{ij,p}$ . This will be cleared up in CH. 5 by insisting  $\hat{H}_1 = -\mathbf{d} \cdot \mathbf{E}$  and  $H_0 \supset |\mathbf{E}|^2$ .

### 2.1.1.2 Lamb shift

The coherent part of the atomic evolution may be obtained from the coarse-grained, effective Hamiltonian

$$\begin{aligned}
\hat{H}_2(t) &\equiv \tilde{\mathcal{H}}[\mathcal{T}(\hat{H}_1)\hat{H}_1] \\
&\rightarrow \sum_{imj} \sum_{pq} g_{im,p} g_{mj,q} \hat{S}_{ij} \left[ \left( \frac{1}{\omega_{mi,p}} + \frac{1}{\omega_{mj,q}} \right) \zeta_{mi,p}^* \zeta_{mj,q} \hat{A}_p^- \hat{A}_q^+ \right. \\
&\quad - \left( \frac{1}{\omega_{im,p}} + \frac{1}{\omega_{jm,q}} \right) \zeta_{im,p} \zeta_{jm,q}^* \hat{A}_p^+ \hat{A}_q^- \\
&\quad + \left( \frac{1}{\omega_{ji,p}} - \frac{1}{\omega_{jm,q}} \right) \zeta_{mi,p}^* \zeta_{jm,q}^* \hat{A}_p^- \hat{A}_q^- \\
&\quad \left. - \left( \frac{1}{\omega_{im,p}} - \frac{1}{\omega_{mj,q}} \right) \zeta_{im,p} \zeta_{mj,q} \hat{A}_p^+ \hat{A}_q^+ \right]
\end{aligned} \tag{2.13}$$

Where we then have each electronic state experiencing a time-averaged energy shift

$$\begin{aligned}
\hat{\delta}_i &\equiv \hat{P}_i \hat{H}_2 \hat{P}_i \\
&= - \sum_j \sum_p \frac{g_{ij,p}^2}{\omega_{ji,p}} \hat{P}_i \\
&\approx \sum_j \gamma_{ij} \log\left(\frac{\omega_\Lambda}{\omega_{ij}}\right) \hat{P}_i \quad \text{for } \langle \hat{N}_p \rangle = 0
\end{aligned} \tag{2.14}$$

As first proposed by Hans Bethe [37], in order to explain the observed  $2^2S_{1/2} \leftrightarrow 2^2P_{1/2}$  level splitting in atomic Hydrogen by Lamb and Rutherford in 1947 [38], taking the electron Compton frequency as the cutoff  $\omega_\Lambda = mc^2/\hbar$  gives  $\delta_S - \delta_P \approx 2\pi \times 1.076$  GHz, which is within 2% of the observed value of  $2\pi \times 1.057$  GHz. This is rather remarkable in the sense that such an accurate result is achieved given the relative conceptual simplicity as compared to the subsequent microscopic explanation by Whelton [39]. That is to say, Lamb shifts, as well as spontaneous emission, are generic features of discrete-leveled systems coupled to a continuum of modes, and these are remarkably accurate approximations in describing the behavior of atoms.

### 2.1.2 Atomic level structure of strontium-87

As we have just shown, the interaction Hamiltonian  $\hat{H}_1$  can be parameterized by two quantities for each pair of electronic states ( $e, g$ ): the transition frequency  $\omega_{eg}$  and the natural lifetime  $\gamma_{eg}$ . While it

is far beyond the scope of this thesis to attempt to calculate these parameters *ab initio* [40], we attempt to give some microscopic intuition for why particular values of  $\omega_{eg}$  and  $\gamma_{eg}$  are what they are in neutral strontium-87.

The motional states of electrons bound to atoms are solutions to the Schrödinger equation with an external Hamiltonian

$$h_i = c\boldsymbol{\alpha}_i \cdot \mathbf{k}_i + \beta_i mc^2 + V_i(\mathbf{r}_i, \mathbf{k}_i) \quad (2.15)$$

is the quasi-relativistic Hamiltonian of an electron with  $V_i$  the potential energy due to interactions with the spin and electric charge of the nucleus and all other electrons [40]. The quantities  $\boldsymbol{\alpha}$  and  $\beta$  are Dirac matrices characterizing the relativistic kinetic energy of the electron, and  $V_i$  is the potential energy due to interactions with the spin and electric charge of the nucleus and all other electrons [40]. The various terms of the above equation produce a hierarchy of energy scales such that they successively provide convenient labels for individual energies  $\omega_i$ . The dominant contribution to the single-particle potential term is the Coulomb interaction energy  $V_i^{\text{Cou.}} \propto r_i$ , yields the principal quantum number  $n_i$ , and the azimuthal quantum number  $l_i$  satisfying  $|l_i|^2 = l_i(l_i + 1)$ , while preserving the electron spin  $\mathbf{s}_i$  with  $|s_i|^2 = s_i(s_i + 1)$ . These states are historically labeled  $nl^*$  where  $l^* = s, p, d, \dots$  for  $l = 0, 1, 2, \dots$

Electrons are bound to atoms with  $\langle\langle k_{ij}r \rangle\rangle \sim \alpha \ll 1$ , where  $\alpha \approx 1/137$  is the fine-structure constant and  $k_{ij} = |\mathbf{k}_i - \mathbf{k}_j|$ , which validates our perturbative expansion in Eq. 2.3. Taylor-expanding the momentum-conservation term,  $\mathbf{r} \cdot \frac{\partial}{\partial \mathbf{r}} \zeta_p T_{ij,p} \propto (1 - i\mathbf{k}_p \cdot \mathbf{r})(\hat{\mathbf{e}}_p \cdot \hat{\mathbf{r}})$  in the microscopic expression for the coupling strength,

$$g_{ij,p} \propto \int d\mathbf{r} \psi_i(\mathbf{r})^* \psi_j(\mathbf{r}) \hat{\mathbf{e}}_p \cdot \hat{\mathbf{r}}, \quad (2.16)$$

where  $\psi_i$  is the real-space electronic wavefunction for an atom in state  $i$ , we see that, to leading order in  $k_p r$ , the coupling strength is significant only between states with opposite parity with respect to  $\hat{\mathbf{e}}_p \cdot \hat{\mathbf{r}}$ .

<sup>4</sup> This is the *parity* selection rule and requires  $(\sum_i l_i + \sum_j l_j) \bmod 2 = 1$ .

The *fine-structure* term  $V_i^{\text{fs}} \propto \mathbf{l}_i \cdot \mathbf{s}_i$  couples an electron's spin  $\mathbf{s}_i$  to its orbital angular momentum  $\mathbf{l}_i = \tilde{\mathbf{k}}_i \times \tilde{\mathbf{r}}_i$ , resulting in conservation of the quantum number  $\mathbf{J}_i = \mathbf{L}_i + \mathbf{S}_i$ , where  $\mathbf{L}_i$  and  $\mathbf{S}_i$  are the

<sup>4</sup> This leading-order expansion gives rise to "electric dipole" transitions. Higher-order expansions lead to "magnetic dipole", "electric quadrupole", etc transitions which will largely be neglected.

total orbital and spin angular momentum for *all* electrons corresponding to the state *i*. This interaction splits states in the principal manifold which are then labeled  $nl^{(2S+1)}L_J$ .

Associated with this fine-structure splitting, states labeled with different  $\mathbf{S}_i$  and  $\mathbf{L}_i$  but with the same  $\mathbf{J}_i$  are weakly “mixed” according to  $\hat{P}_i^{\text{fs}} \rightarrow \hat{P}_i^n + \epsilon_{ij}^{\text{fs}} \hat{P}_j^n$  for  $\epsilon_{ij}^{\text{fs}} \sim V_{ij}^{\text{fs}}/2\omega_{ij}$  and  $\hat{P}_i^n$  being the state projector in the absence of the fine-structure coupling. The coupling coefficients  $g_{ij}^0$  can be decomposed in to

$$g_{ij}^{f,s} = g_{ij}^0 (-1)^{J_i} \sqrt{(2J_g + 1)} \begin{Bmatrix} L_j & L_i & 1 \\ J_i & J_j & S \end{Bmatrix} \quad (2.17)$$

where the term in curly brackets is a *Wigner six-j* symbol. The energy levels and decay rates values are displayed in Fig. 2.1 for experimentally relevant fine-structure manifolds in neutral strontium-87. With its two valence electrons in the 5s-shell, strontium is helium-like. Out of the  $5s5s^1S_0$  ground state, the strongest transition is to the  $5s5p^1P_1$  state at an energy difference of  $\omega_{\text{blue}}/2\pi \approx 650$  THz (hence the colloquial term “blue”) and a decay rate of  $\gamma_{\text{blue}}/2\pi \approx 30.2$  MHz. This transition is used for initial laser cooling and imaging.

The  $5s5s^1S_0 \leftrightarrow 5s5p^3P_1$  “red”-transition at  $\omega_{\text{red}}/2\pi \approx 435$  THz is electric-dipole forbidden in the absence of fine-structure coupling. However, the  $\mathbf{l} \cdot \mathbf{s}$  interaction mixes in  $\epsilon_{ij} \approx 1 \times 10^{-3}$  of the  $5s5s^1P_1$  state, resulting in a finite  $\gamma_{\text{red}}/2\pi \approx 7.48$  kHz electric-dipole coupling strength to the ground state.

In addition to the previously described parity selection rules, the angular momentum coupling coefficients  $T_{ij,p}$  are zero for  $\mathbf{J}_i = \mathbf{J}_j = 0$  and  $|\mathbf{J}_i - \mathbf{J}_j| > s_p$  where  $s_p = 1$  is the photon-spin angular momentum.

*Hyperfine-structure*—The atomic nucleus of strontium-87 has a spin  $|\mathbf{I}|^2 = I(I + 1)$  with  $I = 9/2$  and a magnetic moment  $\mu_I \approx -1.835$  kHz/mT. The *hyperfine* interaction  $V_i^{JI} \propto \mathbf{J} \cdot \mathbf{I}$  suggests an additional quantum number  $\mathbf{F} = \mathbf{J} + \mathbf{I}$ .

The hyperfine splittings and magnetic sensitivities for four experimentally relevant fine-structure manifolds:  $^1S_0$ ,  $^1P_1$ ,  $^3P_0$  and  $^3P_1$ , are shown in Fig. 2.2.

Although this greatly complicates the level structure of strontium-87, as compared to bosonic

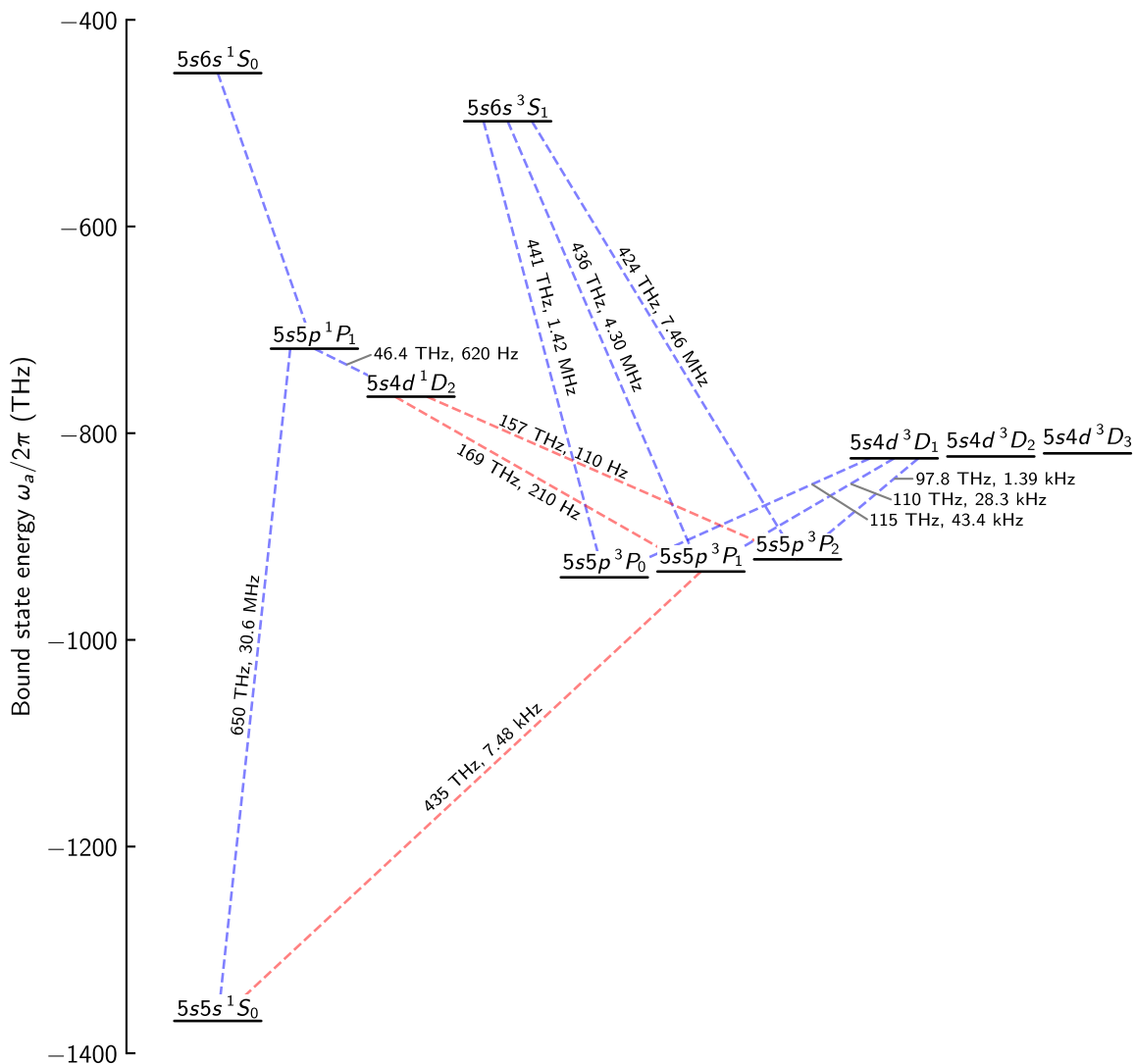


Figure 2.1: Fine-structure energy-levels in neutral strontium. Levels are displayed as solid black lines for the eleven lowest Fine-structure manifolds, with vertical positions corresponding to bound state energies with respect to the ionization threshold. Dashed lines display transitions between levels relevant to the presented work. The blue (red) dashed lines denote dipole allowed (forbidden) transitions, in the absence of Fine-structure coupling. Transitions are labeled by the pair of numbers  $(\omega_{ab}/2\pi, \gamma_{ab}/2\pi)$  where  $\omega_{ab}$  and  $\gamma_{ab}$  are the energy difference and natural decay rate, respectively.

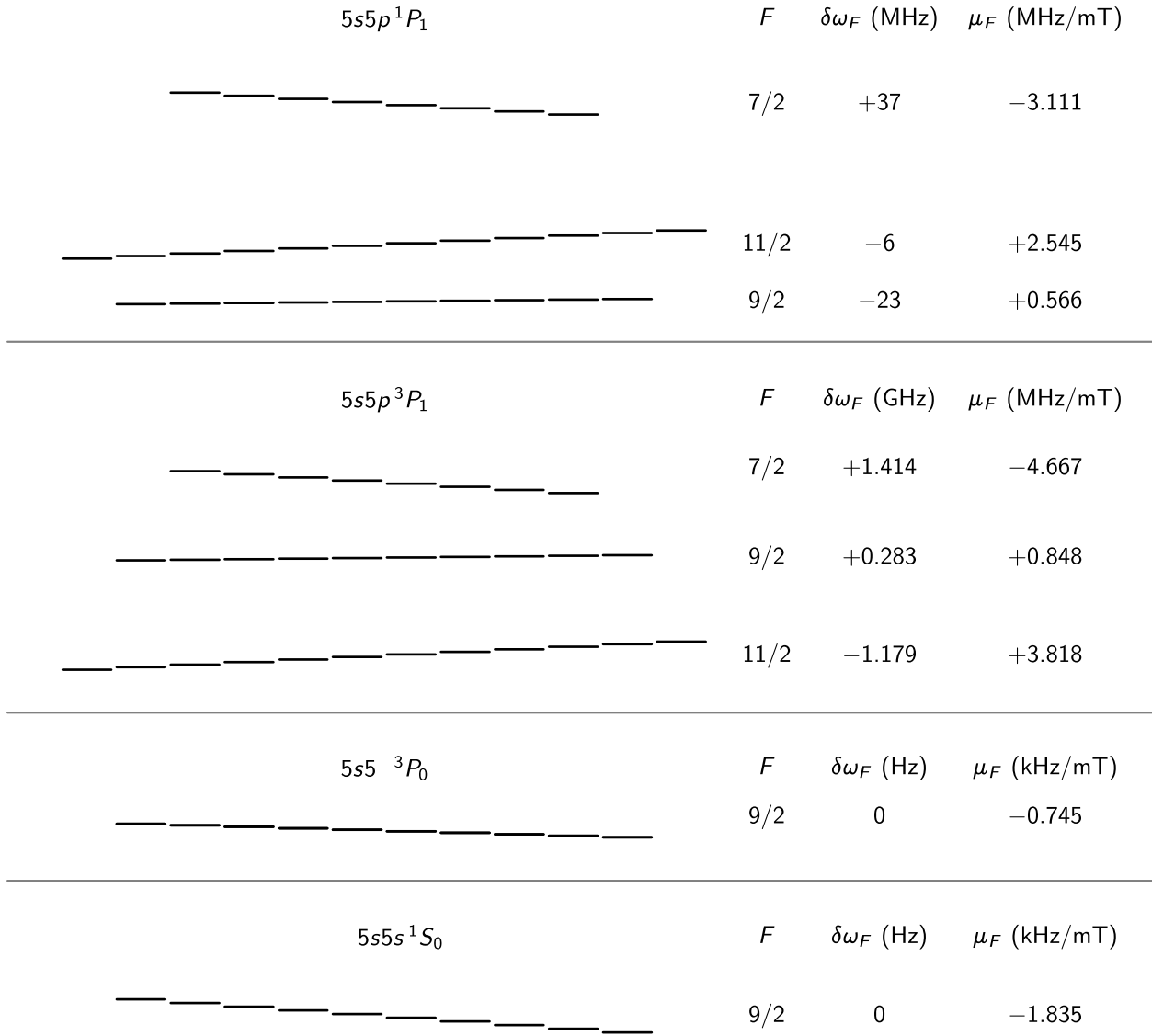


Figure 2.2: Fine-structure energy-levels in neutral strontium-87 for the four fine-structure manifolds:  $5s5p^1P_1$ ,  $5s5p^3P_1$ ,  $5s5p^3P_0$  and  $5s5s^1S_0$ . Magnetic sub-levels  $m_F \in \{-F, -F+1, \dots, F\}$ , are displayed as solid black lines. The hyperfine interaction generates an  $F$ -dependent shift  $\delta\omega_F$  within a given fine-structure manifold, as well as modifying the linear magnetic sensitivity  $\delta\omega_{m_F} = \mu_F m_F B$ .

isotopes with  $\mathbf{I} = 0$ , the mixing of levels with identical  $\mathbf{F}_i = \mathbf{F}_j \neq 0$ , results in the weakly allowed  $5s5s \ ^1S_0 \leftrightarrow 5s5p \ ^3P_0$  *clock transition* at  $\omega_{eg}^{\text{clock}}/2\pi \approx 429$  THz with an excited state lifetime of  $\gamma_{eg}^{\text{clock}}/2\pi \approx 1.35(x)$  mHz [28], not significantly larger than coherence times of state-of-the-art optical resonators [41, 42]. It is then a main challenge to manipulate the external degrees of freedom of the atoms such that all motional effects are insignificant with respect to this energy scale. Thus coherent state interactions are useful tools.

### 2.1.3 Interacting with coherent states of light

In this section we extend the previous results by considering photonic states with specific modes, labeled  $c$ , containing coherent radiation  $\langle \mathcal{H}(\zeta_c \hat{A}_c^+) \rangle = \zeta_p A_c + \text{c.c.}$ , with precisely defined intensities  $I_c \equiv g_c^2 |A_c|^2$ , where  $g_c^2 \equiv 3\omega_V^3 \omega_c / \pi$ , and phases  $\phi_c \equiv \arg(A_c)$ . Such states of light can be generated in the laboratory and, as we shall see, are highly useful for manipulating internal and external degrees of freedom of electrons bound to atoms.

For finite  $A_c$ , atomic operators  $\hat{S}_{ij}$  evolve to first order in  $\bar{\mathcal{H}}(\hat{H}_1 \hat{S}_{ij}) \neq 0$  such that, in the near-resonant limit <sup>5</sup>  $|\omega_{eg,c}| \sim |g_{eg,c}| \ll |\omega_{ij,c}|$  for all  $ij \neq eg$ , we may make the *rotating wave* approximation and keep only terms proportional to  $\zeta_{eg} \zeta_c^* = e^{-i\omega_{eg,c}t}$  to obtain the analytically-solvable closed-set of differential equations for the electronic state

$$\begin{aligned} \frac{d}{dt} \hat{X}_{eg,c} &\approx +\omega_{eg,c} \hat{Y}_{eg,c} - \gamma_{eg} \hat{X}_{eg,c} \\ \frac{d}{dt} \hat{Y}_{eg,c} &\approx -\omega_{eg,c} \hat{X}_{eg,c} - \Omega_{eg,c} \hat{Z}_{eg,c} - \gamma_{eg} \hat{Y}_{eg,c} \\ \frac{d}{dt} \hat{Z}_{eg,c} &\approx +\Omega_{eg,c} \hat{Y}_{eg,c} - \gamma_{eg} (\hat{Z}_{eg,c} + 1) \end{aligned} \quad (2.18)$$

where

$$\hat{X}_{eg,c} \equiv \mathcal{H}[\zeta_{eg} \zeta_c \text{sgn}(A_c) \hat{S}_{eg}], \quad \hat{Y}_{eg,c} \equiv \bar{\mathcal{H}}[\zeta_{eg} \zeta_c \text{sgn}(A_c) \hat{S}_{eg}], \quad \hat{Z}_{eg,c} \equiv \hat{P}_e - \hat{P}_g$$

and  $\Omega_{eg,c} \equiv \gamma_{eg} \sqrt{2s_{eg,c}}$  is the coherent Rabi frequency, and  $s_{eg,c} = 2|A_c|^2 |g_c|^2 / \gamma_{eg}^2$  is the saturation parameter.

<sup>5</sup> We will index transitions  $eg$  when it is implied that the state  $e$  has a higher internal state energy than the state  $g$ .

### 2.1.3.1 Resonant Absorption Imaging

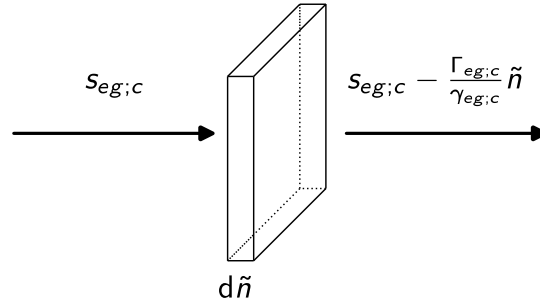


Figure 2.3: Absorption imaging schematic. Coherent light of intensity  $s_{eg,c}$  passes through a slab of two-level atoms, from which  $\frac{\Gamma_{eg,c}}{\gamma_{eg,c}} \tilde{n}$  are scattered into all other modes according to the radiation pattern of the transition  $eg$ .

For a two-level atom, subject to a resonant, coherent radiation field  $A_c$ , we may approximate the time-averaged atomic state by setting the dynamical evolution under Eq. 2.18 equal to zero, giving

$$P_e \rightarrow \frac{1}{2} \frac{s_{eg,c}}{1 + s_{eg,c}} \quad (2.19)$$

Such that photons are scattered out of the coherent field into all other modes, according to Eq. 2.11 at a rate

$$\Gamma_{eg,c} \equiv \int \mathcal{D}_p \frac{d}{dt} N_p \approx \frac{1}{2} \frac{s_{eg,c}}{1 + s_{eg,c}} \gamma_{eg} \quad (2.20)$$

Assuming there are  $d\tilde{n}$  atoms over the interval  $\gamma_{eg} dt/2$ , and assigning  $ds_{eg,c} = \Gamma_{eg,c}/\gamma_{eg} d\tilde{n}$  gives the following differential equation for the total number of atoms  $\tilde{n}$  as a function of  $s_{eg,c}$ .

$$\begin{aligned} ds_{eg,c} &= \frac{s_{eg,c}}{1 + s_{eg,c}} d\tilde{n} \\ \Rightarrow \tilde{n} &= \int_{s_{eg,c}^{\text{in}}}^{s_{eg,c}^{\text{out}}} ds_{eg,c} \frac{1 + s_{eg,c}}{s_{eg,c}} \\ &= \log \left( \frac{s_{eg,c}^{\text{in}}}{s_{eg,c}^{\text{out}}} \right) + (s_{eg,c}^{\text{out}} - s_{eg,c}^{\text{in}}) \end{aligned} \quad (2.21)$$

This relation, as schematically represented in Fig. 2.3 then allows for the atom number to be extracted from absorption images, whereby an atomic cloud is imaged onto a camera and the number of missing photons, as compared to a reference frame taken in the absence of atoms, are counted.

### 2.1.3.2 Ac Stark shift

The presence of a coherent state also modifies the energy spectrum of Eq. 2.14,

$$\hat{\delta}_i = \hat{P}_i \hat{H}_2 \hat{P}_i \approx -\alpha_{i,c} I_c \hat{P}_i$$

where

$$\alpha_{i,c} \equiv \sum_j \frac{\gamma_{ij}}{\omega_{ij}^2 (\omega_{ij}^2 - \omega_c^2)} \frac{T_{ij,c}^2}{2\pi} \quad (2.22)$$

In the laboratory, atoms are subjected to coherent-states of light generated by Gaussian laser-beams, which can be represented mathematically as a sum over plane-wave coherent states:

$$I_c(\mathbf{r}) = I_c(\mathbf{r}_c) \frac{q_{c,x}^i q_{c,y}^i}{|q_{c,x}| |q_{c,y}|} \exp \left\{ -k_c \left[ q_{c,x}^i \frac{x_c^2}{|q_{c,x}|^2} + q_{c,y}^i \frac{y_c^2}{|q_{c,y}|^2} \right] \right\} \quad (2.23)$$

where

$$q_{c,\cdot} = z_c + \frac{i}{2} k_c w_{c,\cdot}^2, \quad q_{c,\cdot}^i = \text{Im}[q_{c,\cdot}]$$

and the spatial coordinates  $\mathbf{x}_c, \mathbf{y}_c, z_c$  represent displacements from the focus at  $\mathbf{r} = \mathbf{r}_c$ , and with orientations determined by  $\mathbf{z}_c \parallel \mathbf{k}_c$  and the eigen-axes of the focal-plane beam waists  $w_{c,x}$  and  $w_{c,y}$ . Expressing a Gaussian beam in terms of the “complex beam parameter”  $q$  is convenient as the vector  $\begin{pmatrix} q \\ 1 \end{pmatrix}$  can be propagated through so-called “ray transfer” matrices  $\begin{pmatrix} A & B \\ C & D \end{pmatrix}$  to compute beam propagation over a distance  $d$  in free-space:  $\begin{pmatrix} 1 & d \\ 0 & 1 \end{pmatrix}$ , and through a thin lens with focal length  $f$ :  $\begin{pmatrix} 1 & 0 \\ -1/f & 1 \end{pmatrix}$ .

## 2.2 Degenerate Fermi Gasses

Up until now, we have effectively assumed that atoms have an infinite mass, such that the interaction  $\hat{H}_1$  did not change an atoms internal state. We now wish to describe multi-atom systems with finite masses.

### 2.2.1 Phase-space densities

We begin by decomposing the atomic projection operators  $\hat{P}_i$ , and uncoupled Hamiltonian  $\hat{H}_0$  into their phase-space distributions,

$$\begin{aligned}\hat{p}_i &= W_i \hat{P}_i \\ \hat{h}_0 &= \sum_i E_i \hat{P}_i \\ \hat{h}_1 &= \sum_{ij,p} g_{ij,p} \mathcal{H}(\Xi_{ij,p} \hat{S}_{ij} \hat{A}_p^+)\end{aligned}\quad (2.24)$$

where  $W_i$  is the Wigner quasi-probability distribution function [43],  $E_i = \omega_i + \hbar^2 |\mathbf{k}_i|^2 / 2m + V_i(\mathbf{r})$  is the sum of internal, kinetic and potential energies at the point  $(\mathbf{k}, \mathbf{r})$  in phase-space. We now have

$$\begin{aligned}\langle\langle \hat{p}_i(\mathbf{k}, \mathbf{r}) \rangle\rangle &\equiv \int d^3\mathbf{k} d^3\mathbf{r} \hat{p}_i(\mathbf{k}, \mathbf{r}) = \hat{P}_i \\ \langle\langle \hat{h}_0(\mathbf{k}, \mathbf{r}) \rangle\rangle &\equiv \int d^3\mathbf{k} d^3\mathbf{r} \hat{h}_0(\mathbf{k}, \mathbf{r}) = \hat{H}_0 - \sum_p \omega_p \hat{N}_p \\ \langle\langle \hat{h}_1(\mathbf{k}, \mathbf{r}) \rangle\rangle &\equiv \int d^3\mathbf{k} d^3\mathbf{r} \hat{h}_1(\mathbf{k}, \mathbf{r}) = \hat{H}_1\end{aligned}\quad (2.25)$$

In free space,  $W_i^0 = \delta(\boldsymbol{\kappa}_i - \mathbf{k}_i)$ , such that absorption of a photon  $p$  from state  $e$  into a state  $g$ , obtains a momentum dependence

$$\Xi_{ij,p}^{00} = W_j \star \zeta_{ij,p} \star W_i = \exp\left\{-i\left[\omega_{ij,p} - \frac{\hbar}{2m}\left(|\mathbf{k}_p|^2 + 2\mathbf{k}_i \cdot \mathbf{k}_p\right)\right]t\right\} \delta(\bar{\mathbf{k}}_i + \bar{\mathbf{k}}_p - \bar{\mathbf{k}}_j) \quad (2.26)$$

Thermodynamic equilibrium maximizes the entropy  $S_i = -P_i \log(P_i)$ , for fixed  $\langle\langle \hat{h}_0 \hat{P}_i \rangle\rangle = (\mathcal{N}/2)\beta^{-1} \hat{P}_i$ , where  $\mathcal{N}$  is the number of degrees of freedom in the index  $i$ , and  $\beta^{-1} = k_B T / \hbar \approx 2\pi T \times 20.9 \text{ GHz/K}$ .

These constraints on  $\langle\hat{P}_i\rangle$  may be solved for an ensemble of fermions by

$$W_i^T(\mathbf{k}, \mathbf{r}) = \left\{ \exp\left[\tilde{E}_i(\mathbf{k}, \mathbf{r}) - \tilde{\mu}\right] + 1 \right\}^{-1} \quad (2.27)$$

where  $\tilde{E}_i(\mathbf{k}, \mathbf{r}) \equiv \beta E_i(\mathbf{k}, \mathbf{r})$  and  $\tilde{\mu}$  are the dimensionless phase-space Hamiltonian, and chemical potential, respectively, normalized by  $\beta$ .

For a harmonically trapped gas, we may write

$$\tilde{E}_i(\mathbf{k}, \mathbf{r}) = \frac{1}{2} \tilde{\Lambda}_i \left[ |\bar{\mathbf{k}}_i|^2 + |\bar{\mathbf{r}}_i|^2 \right] \quad (2.28)$$

where  $\Lambda_i = m_i c^2 / \hbar$  ( $\lambda_i = \hbar / m_i c$ ) is the atomic Compton frequency (wavelength), and we have defined the dimensionless harmonic-oscillator coordinates, given trapping frequencies  $\epsilon_{i,\mu}$ :  $\bar{\mathbf{k}}_i = \lambda_i \mathbf{k}_i$  and  $\bar{\mathbf{r}}_{i,\mu} = (\epsilon_{i,\mu} / c) \mathbf{r}_{i,\mu}$ , and the temperature and trap-frequency normalized Compton frequencies:  $\tilde{\Lambda}_i = \beta \Lambda_i$ , and  $\bar{\Lambda}_i = \Lambda_i / \epsilon_{i,\mu}$ , respectively.

The momentum  $W_i(\bar{\mathbf{k}})$  and coordinate distributions  $W_i(\bar{\mathbf{r}})$  are obtained by integrating  $W_i(\bar{\mathbf{k}}, \bar{\mathbf{r}})$  over all displacements  $\bar{\mathbf{r}}$ , and momenta  $\bar{\mathbf{k}}$ , respectively.

$$\begin{aligned} W_i(\bar{\mathbf{k}}) &= \int d^3 \bar{\mathbf{r}} W_i(\bar{\mathbf{k}}, \bar{\mathbf{r}}) = \left( \frac{\tilde{\Lambda}_i}{\pi} \right)^{3/2} f_{3/2}[\tilde{\mu} - \tilde{E}_i(\bar{\mathbf{k}}, \mathbf{0})] / f_3[\tilde{\mu}] \\ W_i(\bar{\mathbf{r}}) &= \int d^3 \bar{\mathbf{k}} W_i(\bar{\mathbf{k}}, \bar{\mathbf{r}}) = \left( \frac{\tilde{\Lambda}_i}{\pi} \right)^{3/2} f_{3/2}[\tilde{\mu} - \tilde{E}_i(\mathbf{0}, \bar{\mathbf{r}})] / f_3[\tilde{\mu}] \end{aligned} \quad (2.29)$$

where we have defined

$$f_n(q) = \frac{1}{\pi^n} \int d^{2n} x f_0(x^2 + q) = -\text{Li}_n(-\exp(q)) . \quad (2.30)$$

where  $\text{Li}_i(q)$  is the poly-logarithm satisfying  $\text{Li}_0(q) = x/(1-x)$ .

### 2.2.2 Ultra-cold collisions

At second order in  $\hat{H}_2$ , two atoms  $i$  and  $j$ , in internal states with no intrinsic dipole moment  $g_{ij} = 0$ , can interact via

$$\begin{aligned} \hat{P}_{ij} \hat{H}_3^{\text{vac}} \hat{P}_{ij} &= \hat{P}_{ij} \mathcal{T} \{ \tilde{\mathcal{H}}[\hat{H}_2(t) \hat{H}_2(t_0)] \} \hat{P}_{ij} \\ &= \sum_{m,n} \sum_p g_{im,p}^2 g_{jn,p}^2 \frac{\omega_{im} \omega_{jn}}{(\omega_{im}^2 - \omega_p^2)(\omega_{jm}^2 - \omega_p^2)} \hat{P}_{ij} \\ &\rightarrow -\frac{C_{ij}^{(6)}}{r_{ij}^6} \end{aligned} \quad (2.31)$$

where

$$C_{ij}^{(6)} = \frac{3}{2} \sum_{mn} \frac{\gamma_{im} \gamma_{jn}}{\omega_{im}^3 \omega_{jn}^3 (\omega_{im} + \omega_{jn})} \sum_{\hat{\mathbf{e}}_p} (T_{im,p} T_{nj,p})^2 \quad (2.32)$$

is the dipole-dipole van der Waals coefficient. The Hamiltonian of two colliding atoms, in the center-of-mass frame can be written as [44]

$$\hat{h}_0 + \hat{h}_3 = \Lambda_{ij} \left( |\bar{\mathbf{k}}_{ij}|^2 - \frac{\bar{C}_{ij}^{(6)}}{\bar{\mathbf{r}}_{ij}^6} \right) \hat{p}_{ij} \quad (2.33)$$

Where we have normalized  $C_{ij}^{(6)} = \bar{C}_{ij}^{(6)} \Lambda_{ij} \lambda_{ij}^6$ , with  $\Lambda_{ij} = (\Lambda_i \Lambda_j) / (\Lambda_i + \Lambda_j)$  and  $\lambda_{ij} = c / \Lambda_{ij}$ . Low energy collisions are characterized by  $\langle \bar{\mathbf{k}}_{ij} \cdot \bar{\mathbf{r}}_{ij} \rangle \ll 1$ , such that the finite range of the interaction  $\hat{h}_3 \sim \bar{r}_{ij}^6$  can be replaced by a contact interaction  $\hat{h}_3^{\text{eff}} = 4\pi \bar{a}_{ij} \delta(\bar{\mathbf{r}}_{ij})$  where the *scattering-length*  $a_{ij}$  is obtained by matching the far-field  $\bar{r}_{ij} \rightarrow \infty$  solutions to the respective radial Schrödinger equations. For the van der Waals interaction,

$$\left[ \frac{\partial^2}{\partial \bar{r}_{ij}^2} + \frac{\bar{C}_{ij}}{\bar{r}_{ij}^6} \right] u_C(\bar{r}_{ij}) \approx 0,$$

giving

(2.34)

$$u_C(\eta_{ij}) \propto \Gamma\left(\frac{3}{4}\right) \left(\frac{\eta_{ij}^2}{2}\right)^{\frac{1}{4}} \left[ I_{-\frac{1}{4}}(\eta_{ij}^{-2}) - I_{\frac{1}{4}}(\eta_{ij}^{-2}) \frac{I_{-\frac{1}{4}}(\eta_{ij,0}^{-2})}{I_{\frac{1}{4}}(\eta_{ij,0}^{-2})} \right]$$

where  $\eta_{ij}^2 = \bar{r}_{ij}^2 / (\bar{C}_{ij}^{(6)} / 4)^{1/2}$ , and we have used the initial condition  $u_C(\bar{r}_{ij,0}) = 0$ . For pure van der Waals interactions one should take the limit  $\bar{r}_{ij,0} \rightarrow 0$ . However, the true molecular potential at short distances deviates from  $\hat{h}_3$  such that finite  $\bar{r}_{ij,0}$  serves as a proxy for short-range interactions [45]. In the far-field, yet still low-energy, limit,  $1 \ll \eta_{ij} \ll r_{ij} k_{ij}$

$$u_C(\eta_{ij}) \rightarrow \eta_{ij} - 2^{-\frac{1}{2}} \frac{I_{-\frac{1}{4}}(\eta_{ij,0}^{-2})}{I_{\frac{1}{4}}(\eta_{ij,0}^{-2})} \frac{\Gamma(\frac{3}{4})}{\Gamma(\frac{5}{4})} \quad \text{for } \eta_{ij} \rightarrow \infty \quad (2.35)$$

For the effective interaction  $\hat{h}_3^{\text{eff}}$ , replacing the point potential with a spherical shell  $\delta(\bar{\mathbf{r}}_{ij}) \rightarrow \lim_{\bar{r}_{ij,0} \rightarrow 0} \delta(\bar{\mathbf{r}}_{ij} - \bar{\mathbf{r}}_{ij,0}) / 4\pi r_{ij,0}^2$ ,

$$\left[ \frac{\partial^2}{\partial \bar{r}_{ij}^2} + \frac{\bar{a}_{ij}}{\bar{r}_{ij,0}^2} \delta(\bar{r}_{ij} - \bar{r}_{ij,0}) \right] u_\delta(\bar{r}_{ij}) = 0,$$

(2.36)

$$u_\delta(\eta_{ij}) \sim \eta_{ij} - \left( \frac{4}{\bar{C}_{ij}^{(6)}} \right)^{\frac{1}{4}} \bar{a}_{ij} \quad \text{for } \bar{r}_{ij,0} \rightarrow 0$$

Matching the two solutions in the limit  $\eta_{ij} \rightarrow \infty$ , we may identify

$$\bar{a}_{ij} = 2^{-\frac{1}{2}} \left( \frac{\bar{C}_{ij}^{(6)}}{4} \right)^{\frac{1}{4}} \frac{I_{\frac{1}{4}}(\eta_{ij,0}^{-2})}{I_{-\frac{1}{4}}(\eta_{ij,0}^{-2})} \frac{\Gamma(\frac{3}{4})}{\Gamma(\frac{5}{4})}$$

(2.37)

$$= 2^{-\frac{1}{2}} \left( \frac{\bar{C}_{ij}^{(6)}}{4} \right)^{\frac{1}{4}} \frac{\Gamma(\frac{3}{4})}{\Gamma(\frac{5}{4})} \quad \text{for } \eta_{ij,0} \rightarrow 0.$$

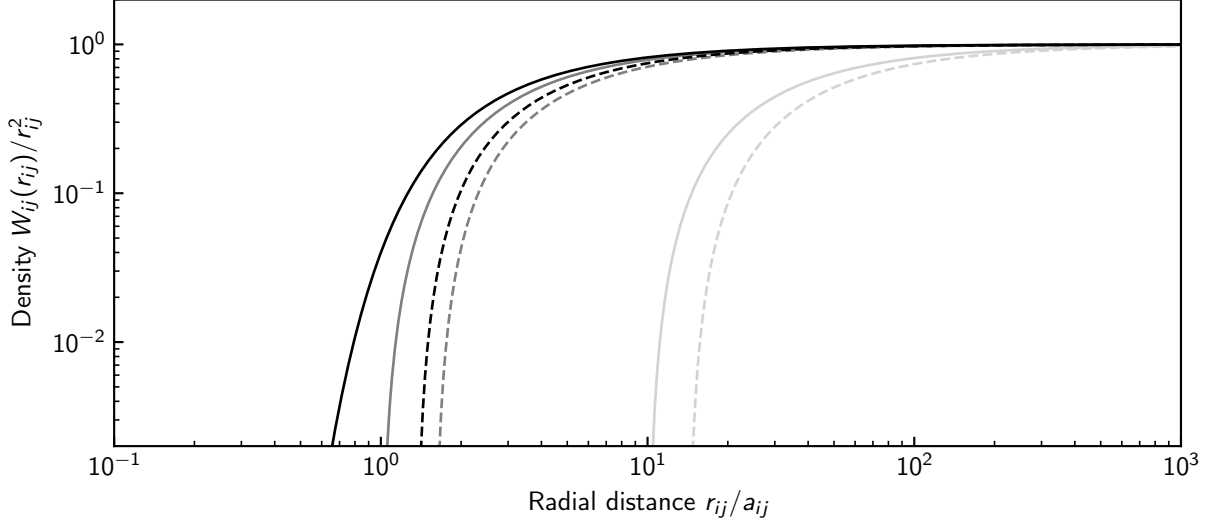


Figure 2.4: Comparison of  $s$ -wave interaction eigenstates. Calculated inter-atomic densities  $W_{ij}(r_{ij})$  as a function of the radial separation  $r_{ij}$  are shown for the van der Waals (solid lines) and effective (dashed lines) interaction Hamiltonians. In increasing order of lightness, densities are plotted for  $\eta_{ij,0} = 10^{-1}$ ,  $10^0$ , and  $10^1$ .

In the limit  $\eta_{ij,0} \rightarrow 0$ ,  $\bar{a}_{ij,0}$  is the van der Waals length. For finite  $\eta_{ij,0}$  the scattering length oscillates over all real values  $\bar{a}_{ij} \in [-\infty, \infty]$  as approximately  $\bar{a}_{ij,0}[1 + \tan(\eta_{ij}^{-2})]$ . Example atomic densities are plotted in Fig. 2.4 for both interaction potentials  $\hat{h}_3$  and  $\hat{h}_3^{\text{eff}}$ .

For neutral strontium in the  $g = 5s5s^1S_0$  ground state,  $C_{gg}^{(6)}/\alpha^2\Lambda_e a_0^6 = 3107(30)$ , and  $a_{gg}^{\text{vdW}}/a_0 \approx 76$  [46], and specifically for strontium-87,  $a_{gg} = 96.2(1)a_0$  where  $a_0 \approx 5.29 \times 10^{-11}$  m is the Bohr radius [47].

For collisions between internal states connected by dipole allowed transitions, one has a finite contribution from  $\hat{h}_2 \sim \bar{r}_{ij}^{-3}$  which are long-range enough such that modeling by an effective contact interaction is not possible, furthermore, emission of a photon at short inter-atomic distances can couple two initially free atoms into a deeply-bound molecular state with a large kinetic energy. Such “light-assisted” collisions preclude coherent spectroscopy of dense gasses unless collisions can be prevented by other means.

## 2.3 Experimental procedure

Here we outline the experimental procedure used from producing lattice-trapped Fermi-degenerate gasses of strontium-87. The main apparatus is schematically represented in Fig. 2.5. The vacuum chamber is divided into three main regions: (1) the cold beam source, (2) the science chamber, and (3) the pumping section. Surrounding the vacuum chamber are three levels of optics used for interacting with atoms in regions (1) and (2).

### 2.3.1 Hot atomic vapor

Naturally occurring strontium is most commonly found in the minerals  $\text{SrSO}_4$  and  $\text{SrCO}_3$ . Chemically pure, dendritic, strontium can be purchased from various chemical supply companies. However, in the solid state, it is still not useful for precision spectroscopy. In order to produce atomic strontium in the gaseous phase, we heat a few grams of dendritic strontium to  $T_{\text{oven}} \approx 750$  K, using a commercial atomic-beam source, as shown in Fig. 2.5.

For a dilute gas in the classical limit ( $\tilde{\mu} \rightarrow -\infty$ ), the phase-space density of a untrapped gas is Gaussian

$$W_i^T(\mathbf{k}, \mathbf{r}) \rightarrow \exp\left[-\frac{\tilde{\Lambda}_i}{2} |\bar{\mathbf{k}}_i|^2\right] \quad \text{for } \tilde{\mu} \rightarrow -\infty. \quad (2.38)$$

The velocity  $\mathbf{v}_i = c\bar{\mathbf{k}}_i$ ; accordingly has an ‘‘root-mean-square’’ (RMS) value

$$\begin{aligned} c\Delta\bar{\mathbf{k}}_i &\equiv c\left[\langle\langle |\bar{\mathbf{k}}_i|^2 W_i^T(\bar{\mathbf{r}}, \bar{\mathbf{k}}) \rangle\rangle\right]^{1/2} = \left(\frac{3k_b T}{2m}\right)^{1/2} \\ &\Rightarrow 1.1 \times 10^{-6} c \approx 330 \text{ m/s} \quad \text{for } T = 750 \text{ K and } m = 86.9 \text{ amu} \end{aligned} \quad (2.39)$$

corresponding to a resonant Doppler broadening, through Eq. 2.26 of  $\Delta(\omega_{eg}/\omega_{eg}^0) = \Delta\bar{\mathbf{k}}_g$  and a recoil shift of  $\bar{\omega}_{eg}/\omega_{eg}^0 = -\omega_{eg}^0/2\Lambda_{eg}$ . Such motional effects are significant as compared to the natural decay-rate of the strontium-87 clock transition  $\gamma_{eg}/\omega_{eg}^0 \approx 1 \times 10^{-18}$ . Various techniques must then be used to remove these motional effects. Laser, and evaporative cooling are used to produce atomic gasses with temperatures in the few nK range. Subsequent trapping in an optical lattice increases the effective mass of the atoms such that Doppler and recoil shifts can be suppressed below the  $10^{-18}$  level.

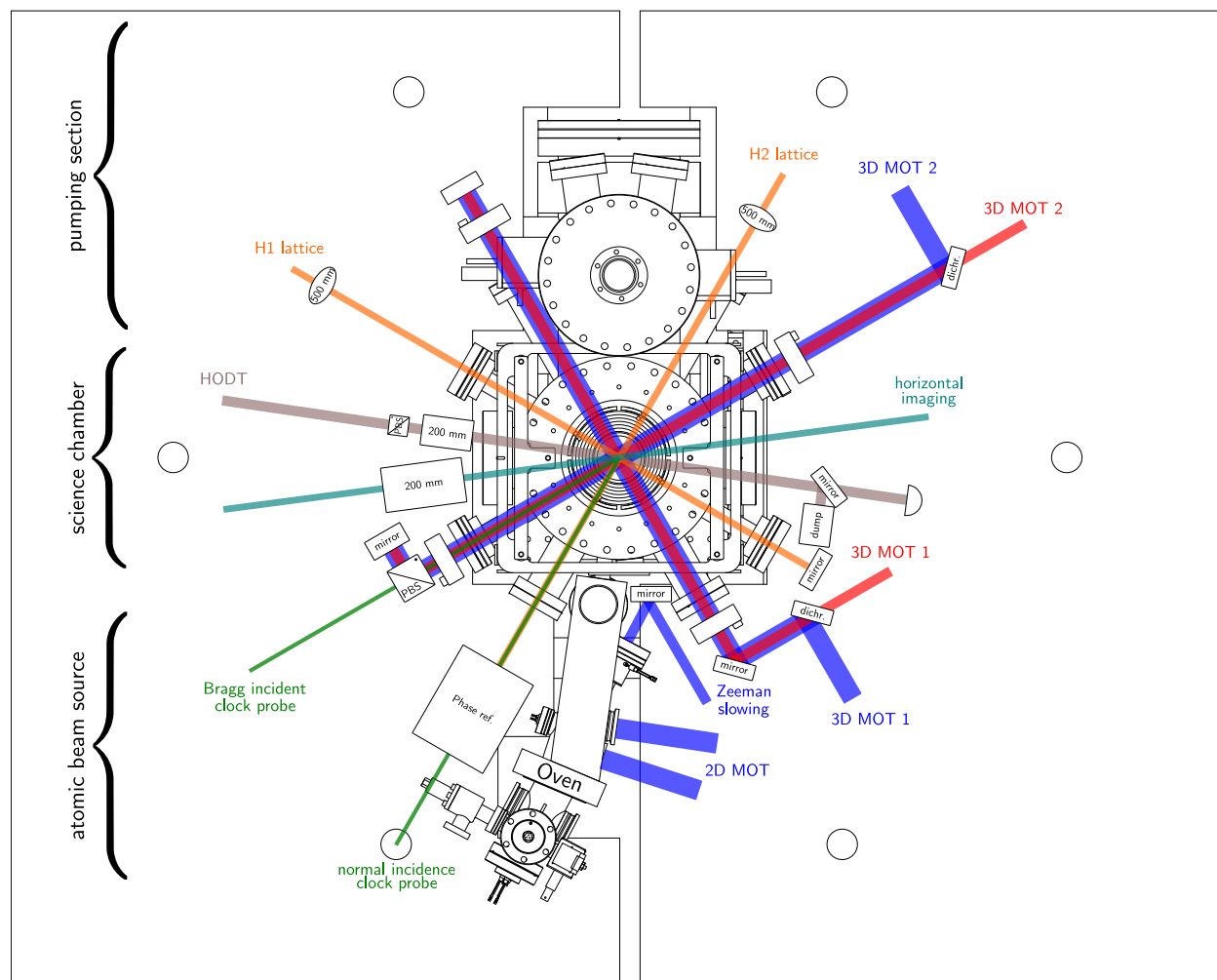


Figure 2.5: Vacuum chamber schematic. Various vacuum chamber regions laser paths which are referred to throughout the text are labeled accordingly. The vacuum pressure in the pumping section, as measured by an ion gauge, is below the  $1 \times 10^{-11}$  Torr-level. Enabling background-gas-collision limited lifetimes longer than two-minutes. The bounding region of the schematic is 5 ft  $\times$  4 ft.

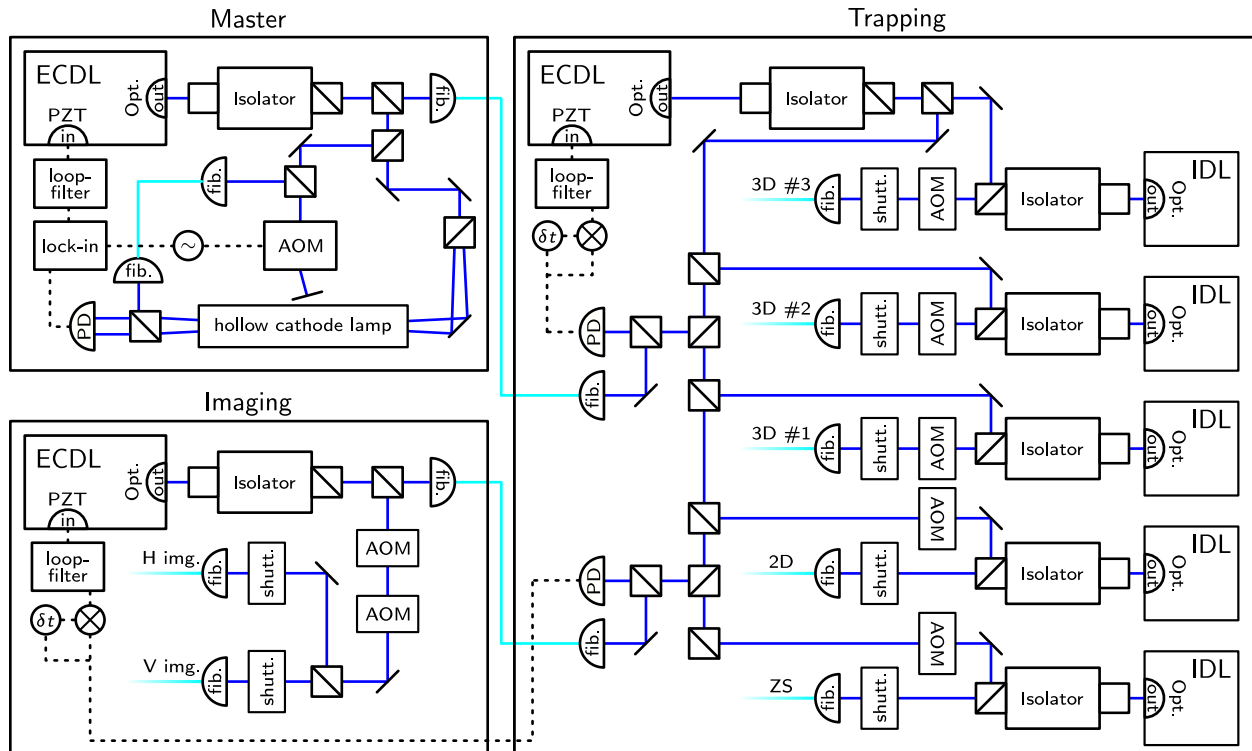


Figure 2.6: Laser layout: 650 THz. A “master” laser is locked to a hot vapor of strontium-88 produced by a hollow cathode lamp using saturated absorption spectroscopy [1]. Secondary lasers are then frequency locked to the master laser using RF interferometers to provide a DC-signal zero crossing at a desired beat-note offset. Trapping light is provided by five injection locked diodes, each providing approximately 120 mW of optical power. The light is provided to the main apparatus via optical fibers.

Preliminary cooling is performed on the  $5s5s^1S_0 \leftrightarrow 5s5p^1P_1$  “blue” transition at  $\omega_{\text{blue}} \approx 650$  THz with  $\gamma_{\text{blue}} \approx 30$  MHz. The coherent radiation at  $\omega_{\text{blue}}$  is produced by a series of diode lasers, shown in Fig. 2.6. The “master”-laser is a commercial external-cavity diode-laser (ECDL) which is frequency locked to a Doppler-free spectrometer signal derived from a hollow-cathode lamp. The various “slave”-lasers include two additional commercial ECDLs which are independently frequency locked to the master laser by feeding a photodiode beat signal into an RF interferometer. Additionally, the cooling light is provided by five injection-locked Fabry-Perot laser diodes.

### 2.3.2 Zeeman Slower

The hot atomic beam is columnated along the  $\bar{\mathbf{k}}_{\text{oven}}$ -axis out of the commercial oven using a microtubule array, resulting in a RMS angular spread of momenta  $\Delta\theta_{\text{oven}} \equiv \Delta(\bar{\mathbf{k}}_g - \bar{\mathbf{k}}_{\text{oven}}) \approx 10$  mrad., and a corresponding transverse temperature of  $T_0^\perp = \Delta\theta_{\text{oven}} T_0 \approx 7.5$  K. The initial *Zeeman-slower* cooling stage then focuses on compressing the momentum distribution along  $\bar{\mathbf{k}}_{\text{oven}}$ .

A 5 mm Gaussian beam propagates anti-aligned to the atomic beam,  $\mathbf{k}_Z = -\mathbf{k}_{\text{oven}}$  with a detuning  $(\omega_Z - \omega_{\text{blue}})/2\pi \approx -500$  MHz. Each absorbed photon imparts a momentum  $\bar{\mathbf{k}}_g \rightarrow \bar{\mathbf{k}}_g + \bar{\mathbf{k}}_{\text{zeeman}}$  while each spontaneously emitted photon,  $\bar{\mathbf{k}}_e \rightarrow \bar{\mathbf{k}}_e - \bar{\mathbf{k}}_p$  for  $\bar{\mathbf{k}}_p$  randomly oriented with respect to  $\bar{\mathbf{k}}_{\text{oven}}$ , such that all together the RMS momentum transfer is  $|\bar{\mathbf{k}}_g| \rightarrow |\bar{\mathbf{k}}_g| - |\bar{\mathbf{k}}_Z| + |\bar{\mathbf{k}}_p|/\sqrt{2}$ . A permanent-magnet produces an axial magnetic field gradient  $\mathbf{B}_Z = B'_Z(\bar{\mathbf{r}}_g - \bar{\mathbf{r}}_0) \cdot \bar{\mathbf{k}}_Z$ , such that the local detunings  $\omega_{\text{blue}} + \mu_{\text{blue}}|\mathbf{B}_Z|$  maximize the number scattered photons over the 5 cm interaction region.

### 2.3.3 Two-Dimensional Magneto-Optical Trap

The second cooling stage compresses the momentum distribution in the transverse direction while simultaneously steering the laser-cooled atoms into the main vacuum chamber. Two subsequent interaction regions provide transverse magnetic field gradients  $\mathbf{B} = B'(\bar{\mathbf{r}}_{2D} - \bar{\mathbf{r}}_g) \perp \mathbf{k}_{\text{oven}}$  offset from the center of the atomic beam. The cooling light is detuned by approximate one line-width  $(\omega_{2D} - \omega_{\text{blue}})/2\pi \approx -30$  MHz such that atoms are preferentially cooled towards  $(\bar{\mathbf{r}}_{2D} - \bar{\mathbf{r}}_g) \perp \mathbf{k}_{\text{oven}} = 0$ . This beam steering is advantageous in that it prevents hot strontium atoms colliding with atoms trapped in the main science chamber.

### 2.3.4 “Blue” MOT

Inside the science chamber, atoms are collected in a three dimensional MOT provided by a quadrupole magnetic field gradient  $\mathbf{B}(\mathbf{r}) \approx B'(\mathbf{x} + \mathbf{y} - 2\mathbf{z})$  with  $B' \approx 0.5$  mT/mm, and three pairs of retro-reflected laser beams, with  $w \approx 6.6$  mm beam waists and  $P \approx 30$  mW of optical power, corresponding to a peak saturation parameter of  $s \approx 1$ . Approximately  $100 \times 10^6$  atoms are trapped into

a region of space with an RMS width of  $\Delta r \approx 1$  mm and a Doppler temperature of 1.5 mK, corresponding to an RMS velocity of 0.3 m/s and a  $\delta\omega_{\text{clock}}^k/\omega_{\text{clock}} = \sqrt{\gamma_{\text{blue}}/2\Lambda_g} \approx 1 \times 10^{-9}$ . At the end of the blue MOT stage, the intensities of each beam are linearly ramped down in order to maximize the transfer-efficiency into the “red”-MOT.

### 2.3.4.1 “Red” MOT

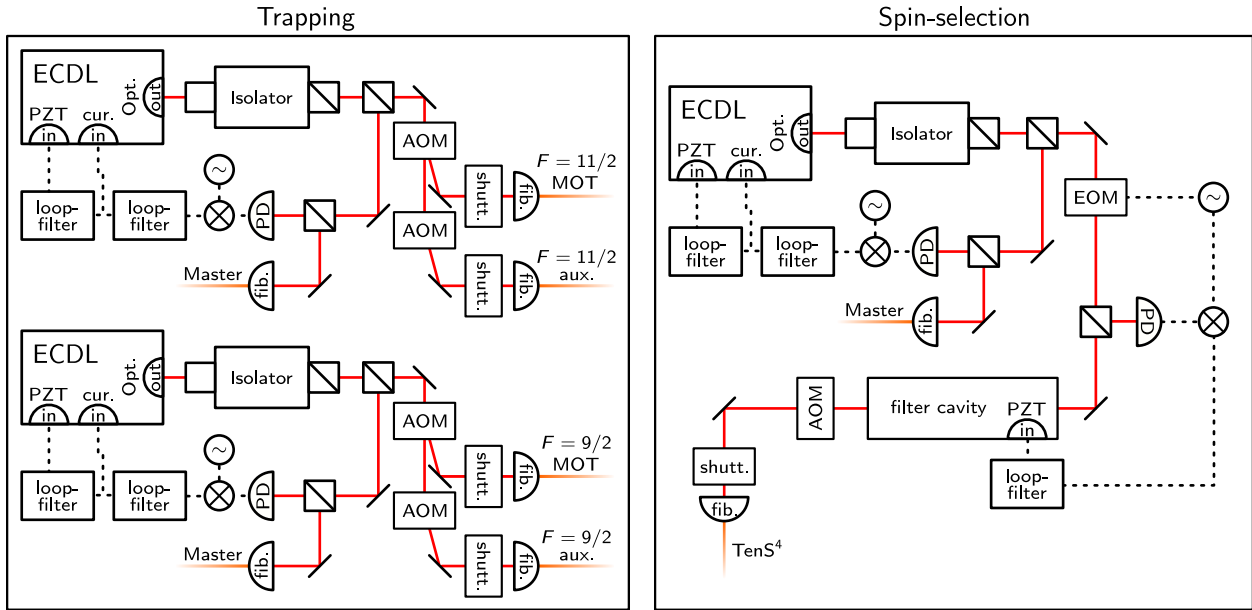


Figure 2.7: Laser layout: 435 THz. phase-stabilized reference light ultimately referenced to the cryogenic-silicon reference-cavity [1], as described in Refs. [2]. Three ECDLs are phase locked to the reference light with arbitrary waveform generators providing the demodulation signals. Approximately 5 mW are provided by each laser to the vacuum chamber via optical fiber.

Due to the reduced (7.48 kHz) line-width of the  $5s5s^1S_0 \leftrightarrow 5s5p^3P_1$  “red” transition at  $\omega_{\text{red}} \approx 435$  THz, The Doppler temperature is significantly reduced  $T_{\text{red}}^{\text{Dop}} \approx 180$  nK approximately equal to the recoil limit  $T_{\text{rec}}^{\text{red}} \approx 280$  nK. As depicted in Fig. 2.7, narrow-line cooling light is provided by two home-built ECDLs phase locked to a third “master”-laser, which is itself referenced to the clock laser via a frequency comb.

Approximately  $10 - 40 \times 10^6$  atoms can be obtained with temperatures in the range of  $1 - 4$   $\mu\text{K}$ , and RMS widths of  $\Delta r_{\text{red}} \approx 100$   $\mu\text{m}$ . At this point, optical depths can easily exceed 200, prior to

considering motional broadening. The corresponding trapping produces a significant trade off between atom number and temperature, and the peak phase-space density is limited to approximately  $10^{-3}$ . The phase-space density of the atomic gas can be further improved by cooling into a “crossed-dipole” trap

### 2.3.5 Far-off-resonant optical trapping

$F_i$	Label $k$	$\omega_{ki}/2\pi$ (THz)	$\gamma_{ki}/2\pi$ (kHz)	$\alpha_{\text{dc}}^0$ (a.u.)	$\alpha_{\text{lat.}}^{(0)}$ (a.u.)	$\alpha_{\text{lat.}}^{(1)}$ (a.u.)	$\alpha_{\text{lat.}}^{(2)}$ (a.u.)
0	$5s5p^3P_1$	434.82	7.458	0.230	0.817	0	0
0	$5s5p^1P_1$	650.49	30240	185.8	274.0	0	0
0	$5s6p^3P_1$	1015.3	4.83	0.005	0.006	0	0
0	$5s6p^1P_1$	1022.2	336.5	0.339	0.390	0	0
0	other $^1P_1$	1876.0	121000	10.75	11.20	0	0
0	Total	—	—	197.1	286.0	0	0
9/2	Total	—	—	197.1	286.0	$4.5 \times 10^{-5}$	$1.57 \times 10^{-5}$

Table 2.1: Line strengths for  $5s5s^1S_0$  polarizability calculation.

$F_i$	Label $k$	$\omega_{ki}/2\pi$ (THz)	$\gamma_{ki}/2\pi$ (kHz)	$\alpha_{\text{dc}}^0$ (a.u.)	$\alpha_{\text{lat.}}^{(0)}$ (a.u.)	$\alpha_{\text{lat.}}^{(1)}$ (a.u.)	$\alpha_{\text{lat.}}^{(2)}$ (a.u.)
0	$5s4s^3D_1$	115.18	43.62	272.6	-29.5	0	0
0	$5s6s^1S_1$	441.32	1320	38.28	126.5	0	0
0	$5s5d^1D_1$	620.24	5713	42.46	65.64	0	0
0	$5p5p^3P_1$	632.05	6835	47.11	71.38	0	0
0	$5s7s^3S_1$	692.73	353.1	1.687	2.352	0	0
0	$5s6d^3D_1$	760.51	2365	7.776	10.16	0	0
0	other $^1D_1$	1047.0	37780	34.58	39.47	0	0
0	Total	—	—	444.5	286.0	0	0
9/2	Total	—	—	444.5	286.0	0.191	$3.65 \times 10^{-4}$

Table 2.2: Line strengths for  $5s5p^3P_0$  polarizability calculation.

For an off-resonant coherent state, atoms then experience a position-dependent potential according to Eq. 2.22. Neglecting other forces, the potential minimum is located at the focus when the sum over

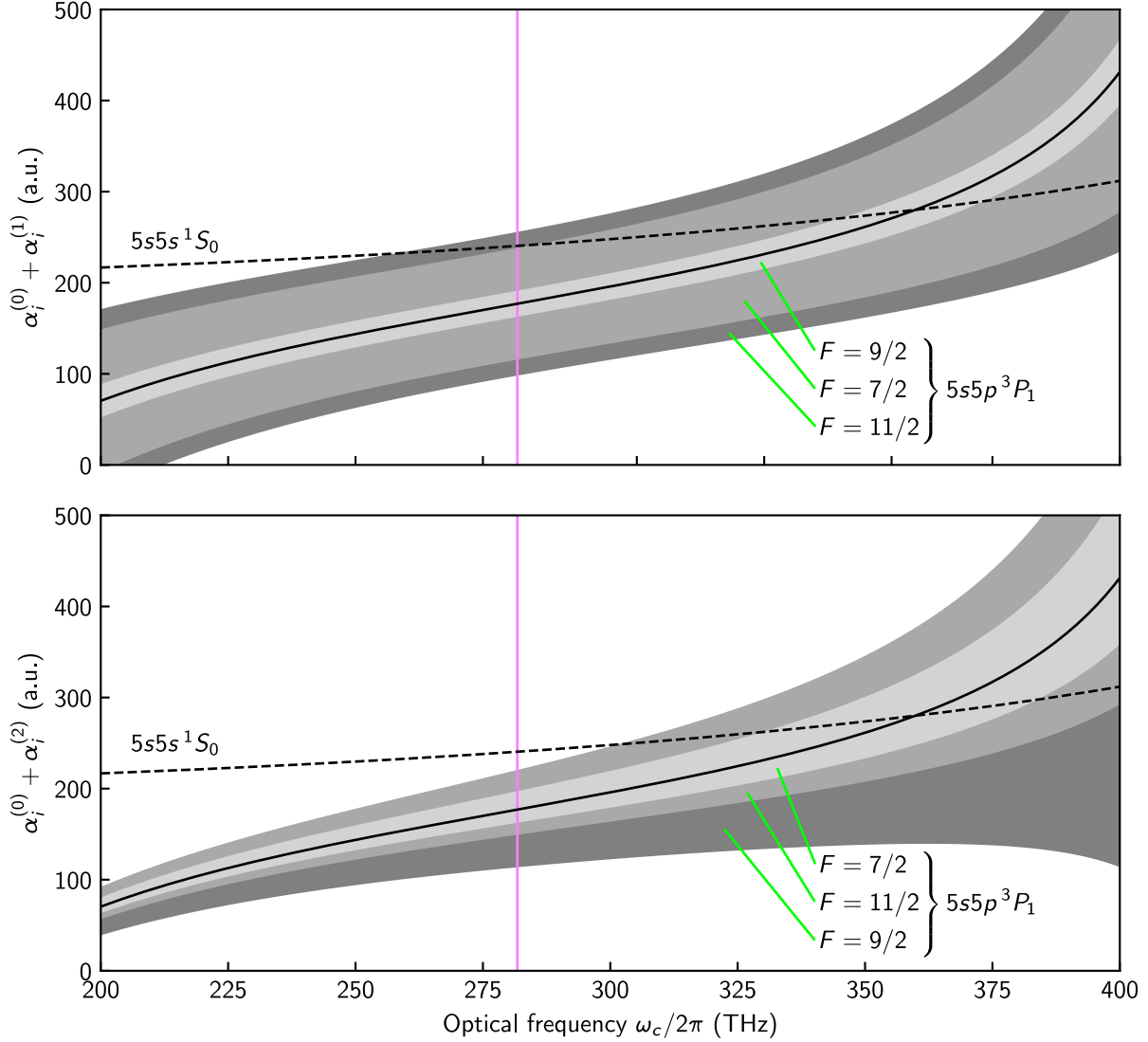


Figure 2.8: Ac polarizabilities for the  $5s5s^1S_0 \leftrightarrow 5s5p^3P_1$  narrow-line cooling transition. The dashed (solid) line shows the scalar polarizability of the ground  $5s5s^1S_0$  (excited  $5s5p^3P_1$ ) state. Shaded regions in the top (bottom) panel show the range of scalar plus vector (tensor) polarizabilities, varying  $m_F$  and  $\hat{\mathbf{e}}_p$ , within each of the three hyperfine manifolds of  $5s5p^3P_1$ :  $F = 7/2, 9/2, 11/2$ . Within the  $5s5p^3P_1$  manifold, vector (tensor) stark shifts are minimized (maximized) for  $F = 9/2$ . The vertical line marks the optical frequency used for bulk-gas trapping:  $\omega_{\text{ODT}} \approx 282$  THz.

$F_i$	Label $k$	$\omega_{ki}/2\pi$ (THz)	$\gamma_{ki}/2\pi$ (kHz)	$\alpha_{\text{ODT}}^{(0)}$ (a.u.)	$\alpha_{\text{ODT}}^{(1)}$ (a.u.)	$\alpha_{\text{ODT}}^{(2)}$ (a.u.)
1	$5s4s^3D_1$	109.58	28.17	-12.77	-24.62	-6.383
1	$5s4s^3D_2$	111.37	52.53	-39.15	74.29	3.915
1	$5s6s^1S_1$	435.72	3811	66.63	32.31	33.31
1	$5s5d^1D_1$	614.64	4170	13.56	4.663	6.781
1	$5s5d^1D_2$	615.09	7522	40.64	-13.96	-4.064
1	$5p5p^3P_0$	620.25	19380	20.16	13.74	-20.16
1	$5p5p^3P_1$	626.45	4991	14.90	5.025	7.448
1	$5p5p^3P_2$	634.68	5191	24.34	-8.106	-2.434
1	$5s7s^3S_1$	687.13	1034	2.044	0.629	1.022
1	$5s6d^3D_1$	754.91	1735	2.275	0.637	1.138
1	$5s6d^3D_2$	755.06	3124	6.825	-1.910	-0.682
1	other $^1D_1$	1041.4	27833	9.378	1.903	4.689
1	other $^1D_2$	1041.4	50190	28.13	-5.709	-2.813
1	Total	—	—	177.0	78.90	21.77
7/2	Total	—	—	177.0	-61.36	10.16
9/2	Total	—	—	177.0	14.34	-31.66
11/2	Total	—	—	177.0	78.90	21.78

Table 2.3: Line strengths for  $5s5p^3P_1$  polarizability calculation.

intermediate levels in Eq. 2.22 is negative. Taylor expanding around  $\mathbf{r}_c$ ,

$$\delta_i(\mathbf{r}) \approx \sum_c \delta_{i,c}(\tilde{\mathbf{r}}_c) \sum_u \left\{ 1 - 2w_{c,u}^{-2} [(\mathbf{r} - \mathbf{r}_c) \cdot \hat{\mathbf{e}}_{c,u}]^2 \right\} \quad (2.40)$$

where  $w_{c,z}^{-2} = k_c^{-2} (w_{c,x}^{-4} + w_{c,y}^{-4})$

Fig. 2.8 plots the atomic polarizabilities for as a function of photon energy over the visible and near-infrared spectrum for the narrow-line cooling transitions. Tab. 2.3 and Tab. 2.1 list the line-strengths used in calculating the polarizabilities in Fig. 2.8.

The bulk-gas optical trap is formed by two Gaussian beams with  $\omega_c = \omega_{\text{odt}} \approx 282$  THz. The first ‘‘surfboard’’ beam propagates orthogonally to gravity with focal-plane beam waists  $w_{\text{surf},x} \approx 340 \mu\text{m}$ ,  $w_{\text{surf},y} \approx 17 \mu\text{m}$ , and  $w_{\text{surf},z} \approx 1.7$  mm. The relatively small waist along gravity is chosen to have a deep enough potential to hold atoms against gravity while minimizing the distribution of Ac Stark shifts. The relatively large waist orthogonal to gravity maximizes the mode-volume enabling laser cooling of many

atoms before rescattering of cooling light becomes problematic. The second “dimple” beam propagates roughly along gravity with  $w_{\text{dimp},x} \approx w_{\text{dimp},y} \approx 30 \mu\text{m}$ .

The combination of the two potentials then defines two distinct regions where atoms are trapped. Within the “crossed-trap” region, atoms are tightly confined in all three spatial directions, and the correspondingly high atomic density limits the efficiency of laser cooling. Outside of the crossed-trap, a relatively dilute gas is trapped in the “reservoir” where laser cooling is still effective, particularly along gravity. Accordingly, we rely on laser cooling to remove entropy of the reservoir and subsequent collisional thermalization to further populate the dimple.

In order to aid the transfer efficiency into the crossed trap, we additionally apply a “transparency” beam which is spatially overlapped with the dimple beam and roughly 20 GHz blue-detuned from the  $5s5p^3P_1 \leftrightarrow 5s6s^3S_1$  transition [34]. This light significantly lowers the cooling transition frequency for atoms located in the crossed trap such that they do not interact with the cooling light and remain in the ground state, preventing light assisted collisions.

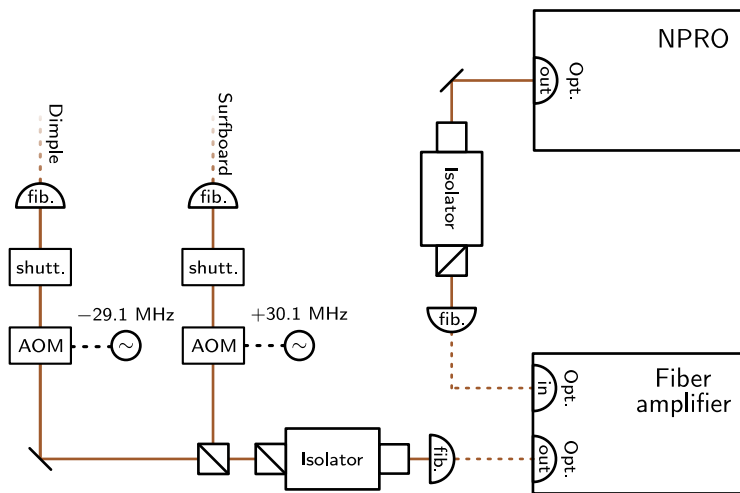


Figure 2.9: Laser layout: 282 THz. The bulk gas optical trapping light is produced by a commercial NPRO laser seeding a 50 W fiber amplifier. Between 2 - 5 W are delivered to the vacuum chamber via photonic crystal optical fibers.

At the end of the laser cooling stage, which lasts about 1-2 seconds per experimental shot,

we obtain a cloud of approximately  $10^6$  atoms at a temperature of approximately  $2 \mu\text{K}$  and a peak phase-space density approaching 1.

The phase-space distribution is characterized via “time-of-flight” absorption imaging. By instantaneously turning off the optical traps, the momentum distribution is mapped onto position  $\mathbf{r}_i(T_{\text{tof}}) = \mathbf{r}_i(0) + \mathbf{k}_i(0)T_{\text{tof}}/m$ . For multiple fermionic particles, and ignoring collisional energies, the *in-site* phase-space distribution of atomic densities is

$$\hat{\rho}_i = \left\{ \exp \left[ \frac{\mathcal{H}(h_{\text{odt}})}{k_{\text{B}}T} \right] + 1 \right\}^{-1} \hat{P}_i$$

with

$$\begin{aligned} h_{\text{odt}}(\bar{\mathbf{k}}_i, \bar{\mathbf{r}}_i) &= \frac{|\mathbf{k}_i|^2}{2m} - \alpha_{i,\text{surf}} I_{\text{surf}}(\mathbf{r}) - \alpha_{i,\text{dimp}} I_{\text{dimp}}(\mathbf{r}) \\ &\approx \frac{|\mathbf{k}_i|^2}{2m} + \frac{1}{2} m (\boldsymbol{\omega}_{\text{odt},x} \cdot \mathbf{r})^2 \end{aligned} \quad (2.41)$$

in time-of-flight, we may substitute  $\mathbf{r}_i \rightarrow \mathbf{r}_i(t_0) + \mathbf{k}_i(t_0)t$ , such that in the limit  $\bar{\mathbf{k}}\bar{t} \gg \sqrt{\langle \bar{\mathbf{r}}^2 \rangle}$  the imaged density distribution approaches

$$W_i(\bar{\mathbf{r}}_i^\perp) \rightarrow \left( \frac{\tilde{\Lambda}_i}{\pi} \right)^2 f_2 \left[ \tilde{\mu} - \frac{1}{2} \tilde{\Lambda}(\bar{k}_i^\perp \bar{t})^2 \right] / f_3[\tilde{\mu}] \quad (2.42)$$

using the Fermi functions  $f_n$  defined previously in Eq. 2.30. Then using prior knowledge of  $t$ , this can be used as a fit function to obtain the temperature  $\beta^{-1}$  and the quantity  $\mathcal{Z} = f_3(\tilde{\mu})$  from which one often computes the reduced temperature

$$T/T_F = (6\mathcal{Z})^{-1/3} \quad (2.43)$$

for quantum degenerate Fermi gases satisfying  $\mathcal{Z} \gg 1$ .

### 2.3.6 Evaporative cooling

Further cooling beyond the above results is achieved by *evaporative cooling*. The finite trap depth  $U = \delta_{\text{odt}}(\mathbf{r}_{\text{odt}})$  provides an effective energy cutoff in phase-space distribution given in Eq. 2.27. In the presence of gravity, atoms with energies greater than  $U$  are irreversibly lost. An instantaneous decrease in the total trap depth  $U \rightarrow U - dU$  reduces the atom number by an amount  $dN \approx g(U) dU$ , where  $g$  is the density of states. This process reduces the mean energy  $\epsilon = \int^U dE E g(E) < U$  of the remaining atoms

by an amount  $N d\epsilon = dN(U - \epsilon)$ . Subsequent thermalization, provided by  $s$ -wave collisions, then gives  $N d\beta^{-1} = dN(U - \beta^{-1}) > 0$ . The maximal cooling rate  $\frac{d\beta^{-1}}{dt} \leq \frac{U}{\tau_{\text{col}}}$  is then determined by the rate of  $s$ -wave collisions  $\tau_{\text{col}}^{-1} = 4\pi a_{gg}^2 c \bar{\mathbf{k}} \mathcal{N} / \langle \langle r_{ij}^3 \rangle \rangle$  [34], where  $\mathcal{N}$  is the number of atoms between which  $s$ -wave collisions are allowed. In the case of strontium-87, which has ten magnetic sub-levels in the  $5s5s^1S_0$  hyperfine manifold,  $\mathcal{N} = \frac{9}{10} N$ .

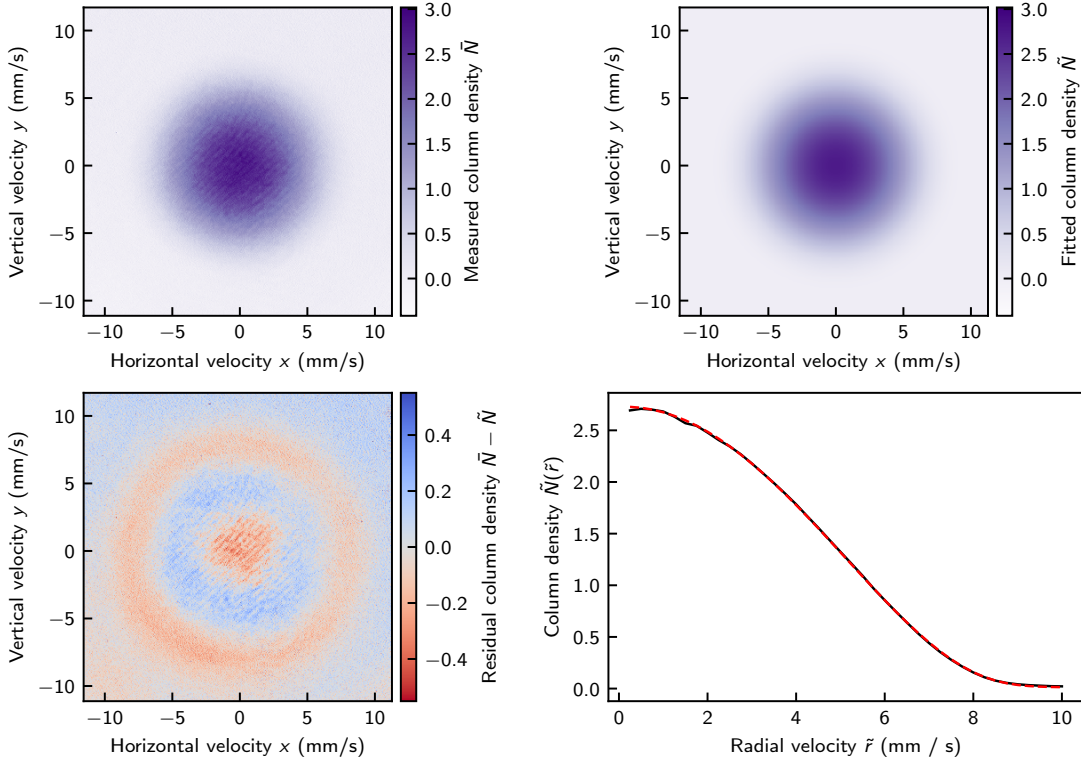


Figure 2.10: Degenerate Fermi gas with ten spin components in time-of-flight. After a 10 ms time-of-flight, absorption images were taken of a degenerate Fermi gas of  $2 \times 10^5$  atoms, revealing a degeneracy parameter of  $T/T_F \approx 0.1$ . The top left (right) panel shows the observed (fitted) column density of atoms as a function of transverse velocity. The bottom left panel shows the residuals of the observed momentum distribution with respect to a Gaussian fitting function. The bottom right panel shows radial averages of the data (black) and fit (red).

At the end of evaporation, thermodynamic parameters are extracted via time-of-flight absorption images, such as those shown in Fig. 2.10 corresponding to a 10-nuclear-spin-component degenerate Fermi gas of  $2 \times 10^5$  atoms with  $T/T_F \approx 0.1$

### 2.3.7 Spin-state manipulation

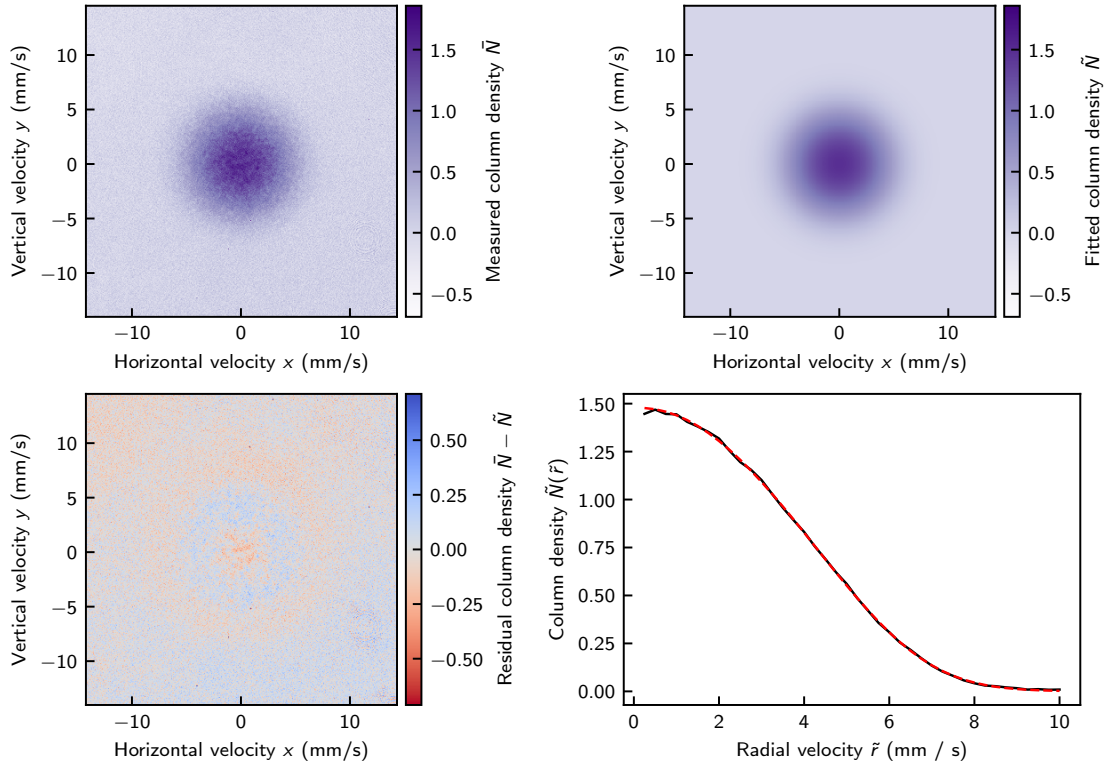


Figure 2.11: Degenerate Fermi gas with a single spin components in time-of-flight. After a 10 ms time-of flight, absorption images were taken of a degenerate Fermi gas of  $2 \times 10^4$  atoms, revealing a degeneracy parameter of  $T/T_F \approx 0.2$ . The top left (right) panel shows the observed (fitted) column density of atoms as a function of transverse velocity. The bottom left panel shows the residuals of the observed momentum distribution with respect to a Gaussian fitting function. The bottom right panel shows radial averages of the data (black) and fit (red).

While the presence of all ten magnetic sub-levels is advantageous for rapid evaporative cooling, often we wish to spectroscopically interrogate a single magnetic sub-level. The high atomic density precludes the use of optical pumping to remove unwanted populations as light assisted collisions can introduce heat into the remaining Fermi seas. To overcome this obstacle, we apply off-resonant light, detuned by  $\sim 266$  MHz above the  $F = 11/2$  hyperfine manifold of  $5s5p^3P_1$ , such that the polarizability is negative for all sub-levels other than  $m_F = \pm 9/2$ . Introducing a weak elliptical polarization then breaks the degeneracy between  $m_F = \pm 9/2$ , such that with further fine-tuning of the laser frequency,

we can kick all atoms apart from those in  $m_F = -9/2$  from the trap after a  $100 \mu\text{s}$  pulse of light, while only slightly heating the remaining atoms. Fig. 2.11 shows the resulting momentum distribution of the single-spin Fermi gas taken in time-of-flight via absorption imaging.

### 2.3.8 Optical lattices

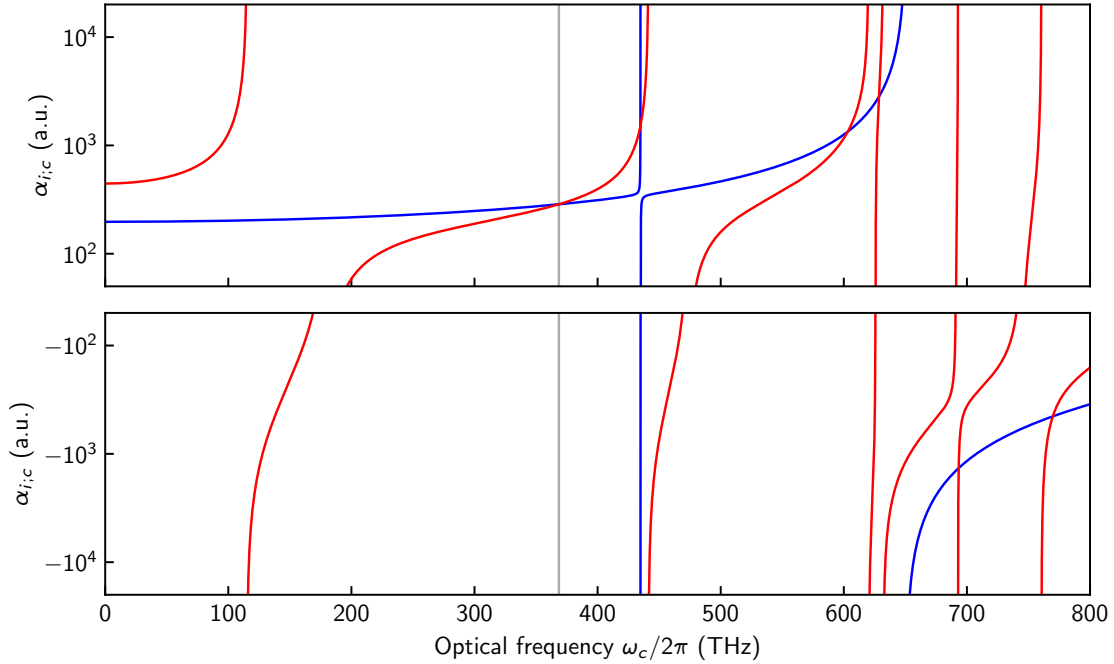


Figure 2.12: Clock state polarizabilities, calculated according to Eq. 2.22, and given in atomic units  $1 \text{ a.u.} = \pi(c/a_0)^3$ . All presented experimental results were obtained using lattice light at the  $\omega_c \approx 368.555 \text{ THz}$  “magic” condition.

At the end of the evaporative cooling stage, the thermal motional broadening  $\bar{k} \approx 5 \times 10^{-12}$  is still far too significant for coherent clock spectroscopy. By tightly confining the atoms in an optical lattice, formed by interfering two counter-propagating lasers, we are able to increase the effective mass by an amount sufficient to reduce motional dephasing below the  $10^{-18}$ -level. The optical frequency  $\omega_c$  of the trapping light is chosen to satisfy the “magic” condition that the differential polarizabilities between the two clock states is zero  $\alpha_{e,c} - \alpha_{g,c} = 0$ . Fig. 2.12 shows the calculated polarizabilities of the two clock states from dc through the visible spectrum.

Given two off-resonant coherent states propagating in opposite directions, we have the following Hamiltonian

$$\begin{aligned}\hat{h}_0 + \hat{h}_2 &= \frac{\hbar|\mathbf{k}_i|^2}{2m} + V_c \cos^2(\mathbf{k}_c \cdot \mathbf{r}_i) \\ &\equiv E_c [\bar{k}_i^2 + \bar{V}_c \cos^2(\bar{r}_i)]\end{aligned}\quad (2.44)$$

where we have taken  $k_c^{-1}$  as the intrinsic length scale of the problem and subsequently normalized  $\bar{k}_i = k_i/k_c$   $\bar{r}_i = k_c r_i$  and defined  $E_c = \hbar k_c^2/2m$ . Fourier transforming the lattice potential with respect to  $\bar{r}_i$ ,

$$h_{\text{lat.}}(\bar{k}_i, \bar{r}_i) = E_c \int d\bar{k}'_i \left\{ k_i^2 \delta(\bar{k}'_i - \bar{k}_i) + \frac{1}{4} V_c e^{-i\bar{k}'_i \bar{r}_i} [2\delta(\bar{k}'_i - \bar{k}_i) + \delta(2 + \bar{k}'_i - \bar{k}_i) + \delta(2 + \bar{k}'_i - \bar{k}_i)] \right\} \quad (2.45)$$

The eigenstates of the above Hamiltonian may then be expressed as a tri-diagonal matrix and numerically diagonalized, yielding the momentum-space coefficients  $C(\bar{q}_i, \bar{k}_i)$ , Energies  $E_n(\bar{q}_i)$ , and spatial wave functions  $\phi_{n_i}(\bar{q}_i) = \sum_{m \in \mathbb{Z}} C_{n_i}(\bar{q}_i, \bar{q}_i + 2m) \phi_{\bar{k}_i}(\bar{q}_i + 2m)$  where the quantum number  $\bar{q}_i$  is the *quasi-momentum*. Numerical values of these quantities are plotted in Fig. 2.13 for three trap depths  $V_c \in \{-1, -8, -64\}$

In transferring the bulk gas at the end of evaporation into a cubic lattice, care must be taken to balance relevant energy scales in order to maximize the number of atoms loaded into the ground band  $n = 0$ . As shown in Fig. 2.14, the lowest two bands in a simple cubic lattice have energy overlap for lattice depths  $|\bar{V}_c| > 2.2$ . Our strategy for loading the lattice is then to adjust the ODT trapping frequencies such that  $E_F < E_c$ , where the ground band is at most half full and no other bands are occupied. After slowly ramping the lattice potential up to  $\bar{V}_c \approx 2.5$ , we are then able to compress the gas by increasing the ODT trapping frequencies, without worry of adiabatically populating higher bands. Once the desired density is achieved, we are then able to continue ramping the lattice depths to their desired values, typically  $\bar{V}_c > 70$  for clock spectroscopy. The lattice light is provided by the two optical setups described in Fig. 2.15.

Since we desire to hold the atoms in a deep lattice potential for many seconds, careful considerations must be made to noise processes in the trapping light to minimize heating. Appendix B describes our theoretical basis for calculating heating rates based on measured intensity and pointing noise of the lattice

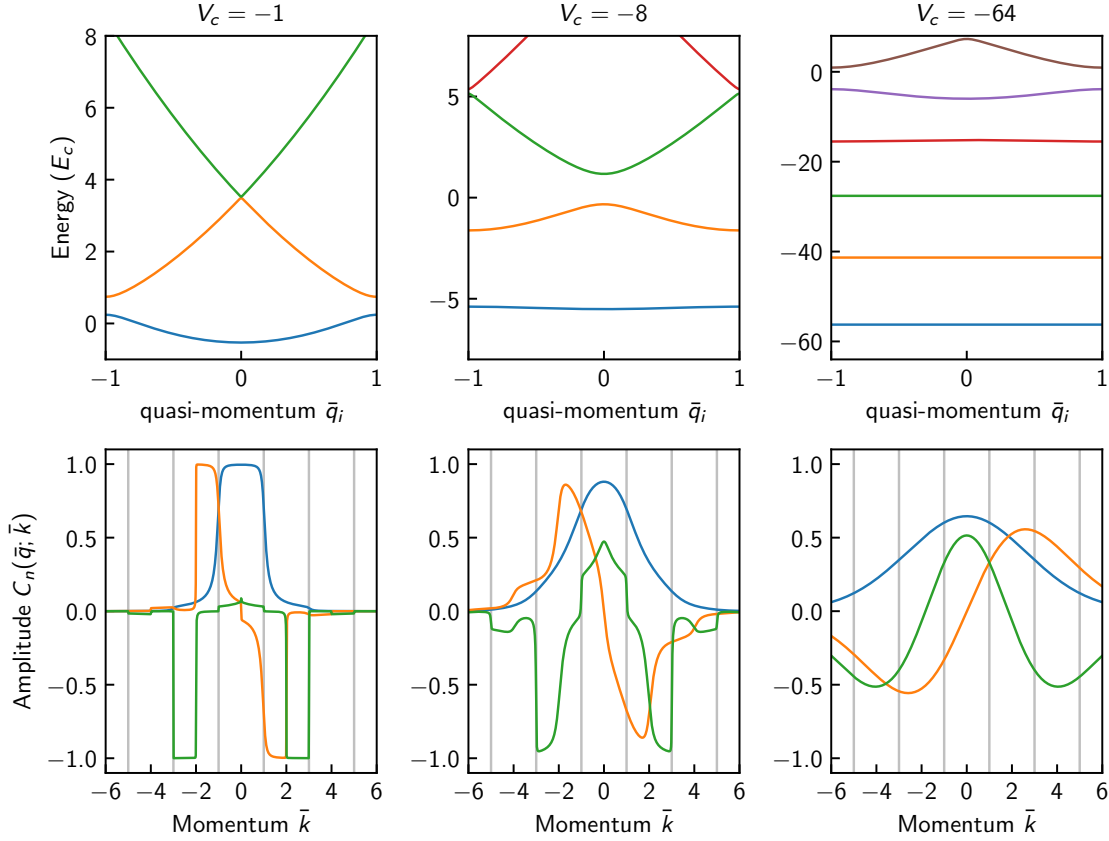


Figure 2.13: Diagonalization of one-dimensional cosine lattice potential in Eq. 2.45. (Top panel) The obtained energies are shown for three different trap depths  $V_c \in \{-1, -8, -64\}$ . Different colors correspond to subtraction of different band indices  $n$ . (Bottom panel) The momentum-space coefficients are shown for the first three bands  $n \in \{0, 1, 2\}$ . The coefficients yield the eigenstates in momentum space via the sum  $\phi_n(\bar{q}) = \sum_{m \in \mathbb{Z}} C_n(\bar{q}, \bar{q} + 2m) \phi_{\bar{k}}(\bar{q} + 2m)$ .

beams. We after optimization of lattice-intensity feedback, we are able to trap ground-state atoms with lifetimes exceeding 100 s.

With the goal of characterizing the filling fraction  $n_a$  of the band insulator, we first define the dimensionless potential  $u_{\mathbf{a}} = \mathbf{a} \cdot \mathbf{u} \cdot \mathbf{a}$  with

$$\mathbf{u} = \frac{1}{2a^2} \left( \sigma_{\hat{x}}^{-2} \hat{x}\hat{x} + \sigma_{\hat{y}}^{-2} \hat{y}\hat{y} + \sigma_{\hat{z}}^{-2} \hat{z}\hat{z} \right) \quad (2.46)$$

The dimensionless fit parameters  $\sigma_{\hat{n}}$  characterize the strength of the confining potential along the  $\hat{n}$ -th axis.

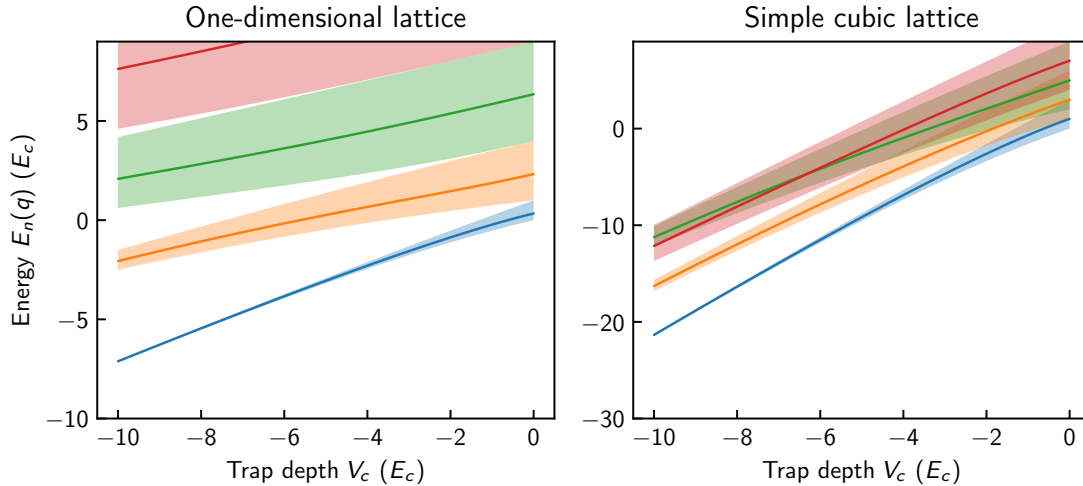


Figure 2.14: Energy spectrum for one-dimensional and simple cubic lattices at weak lattice depths. For a one-dimensional lattice, an energy gap opens up between the lowest two bands for infinitesimal  $V_c$ . In three dimensions, the first excited band corresponds to a motional excitation along only a single direction and an energy gap only emerges for  $\bar{V}_c > 2.2$

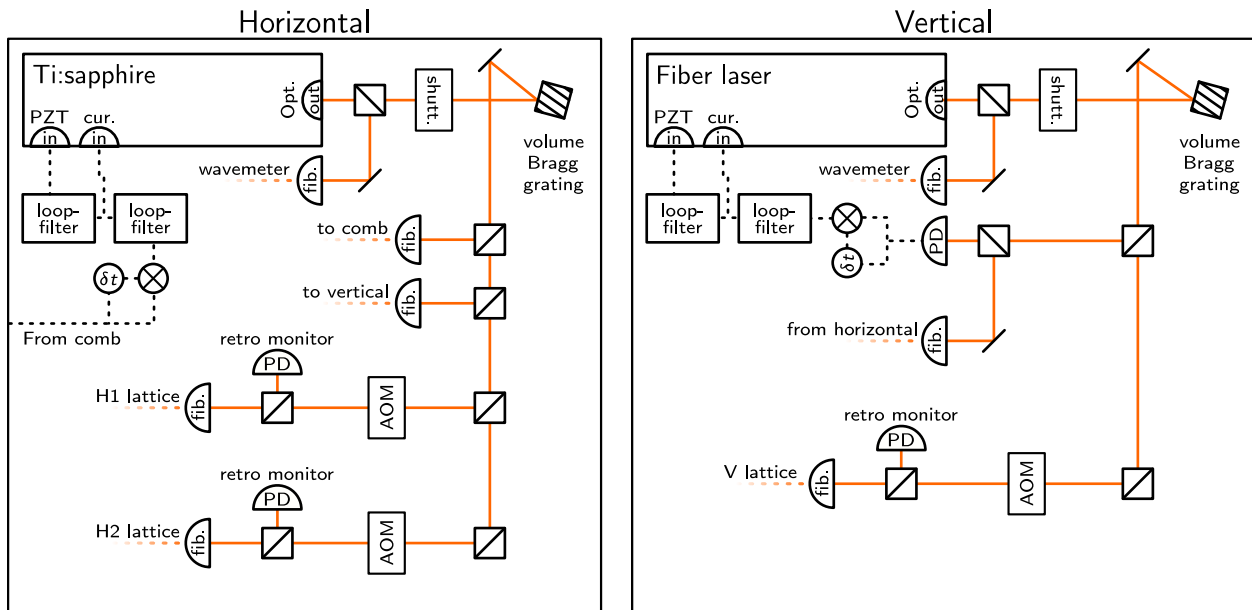


Figure 2.15: Lattice laser layout. The lattice light is provided by two commercial lasers reverenced to the clock light via a frequency comb. The volume Bragg gratings remove residual light outside of a 10 GHz passband. The retro monitors are used to back-couple the retro-reflected light in order to maximize the mode overlap at the position of the atoms.

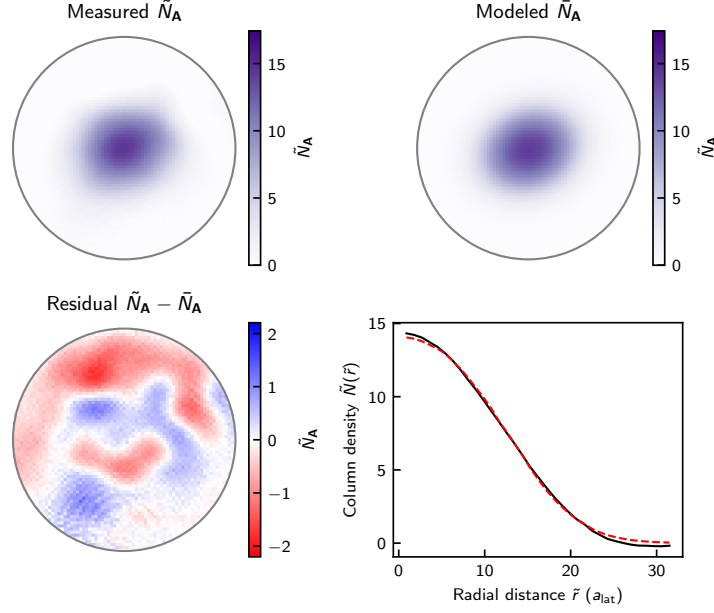


Figure 2.16: Band insulator density distribution. An in-situ density distribution of the band insulator is captured via resonant absorption imaging. The top two panels show the observed and fitted column densities  $\tilde{N}$ . The bottom left panel shows the residuals of the fitted distribution. The bottom right panel shows the radial average of both distributions. Given the agreement between the observed data and the fit, we then use the fit to reconstruct the three-dimensional density  $n$ .

For a grand canonical ensemble under the local-density-approximation we define the dimensionless local chemical potential  $\mu_{\mathbf{a}} = \mu_0 - u_{\mathbf{a}}$  where the peak chemical potential  $\mu_0$  is an additional fit parameter. The corresponding partition function for identical fermions restricted to the ground band of the lattice is given by  $Z_{\mathbf{a}} = 1 + e^{\mu_{\mathbf{a}}}$ . The local density  $n_{\mathbf{a}}$  is then

$$n_{\mathbf{a}} = Z_{\mathbf{a}}^{-1} e^{\mu_{\mathbf{a}}} = \frac{e^{\mu_{\mathbf{a}}}}{1 + e^{\mu_{\mathbf{a}}}}. \quad (2.47)$$

Summing along the imaging axis  $\hat{\mathbf{m}}$  gives the column density fitting function

$$N_{\mathbf{a}_{\hat{\mathbf{m}}}} = \sum_{\mathbf{a}' \parallel \mathbf{a}_{\hat{\mathbf{m}}}} n_{\mathbf{a}'}. \quad (2.48)$$

Fitting absorption images, such as those presented in Fig. 2.16 to  $N_{\mathbf{a}_{\hat{\mathbf{m}}}}$  with four free parameters  $(\mu_0, \sigma_{\hat{x}}, \sigma_{\hat{y}}, \sigma_{\hat{z}})$  exhibits large covariance between  $\mu_0$  and  $w_{\hat{\mathbf{n}}}$  for  $\mu_0 \ll 1$ . This ambiguity can be fixed by imaging along an orthogonal axis. Images taken along  $\hat{\mathbf{m}} = \hat{\mathbf{z}}$  reveal  $\sigma_{\hat{x}} \approx \sigma_{\hat{y}}$  such that the aspect ratio

$\beta = \sqrt{\sigma_{\hat{x}}\sigma_{\hat{y}}}/\sigma_{\hat{z}} \approx 1.79$  can be constrained by fitting absorption images taken along  $\hat{\mathbf{m}} = \cos(\pi/6)\hat{\mathbf{x}} + \sin(\pi/6)\hat{\mathbf{y}}$ . Under this constraint, the fit to  $N_{\mathbf{a}_2}$ , yields  $\mu_0 \approx 1.44$ ,  $\sigma_{\hat{x}} \approx 8.8$ , and  $\sigma_{\hat{y}} \approx 7.2$ .

With our model for  $n_{\mathbf{a}}$  determined, various thermodynamic quantities can be numerically extracted.

The peak density is

$$n_0 = \frac{e^{\mu_0}}{1 + e^{\mu_0}} \approx 0.81 . \quad (2.49)$$

The total atom number is

$$N = \sum_{\mathbf{a}} n_{\mathbf{a}} \approx 9 \times 10^3 , \quad (2.50)$$

in agreement with time-of-flight absorption measurements. The RMS width along the  $\hat{\mathbf{n}}$ -th axis is given by

$$w_{\hat{\mathbf{n}}}^2 = \sum_{\mathbf{a}} (\mathbf{a} \cdot \hat{\mathbf{n}})^2 n_{\mathbf{a}} \rightarrow (w_{\hat{x}}, w_{\hat{y}}, w_{\hat{z}}) = (3.9 \mu\text{m}, 3.8 \mu\text{m}, 2.1 \mu\text{m}) . \quad (2.51)$$

The entropy per particle at the  $\mathbf{a}$ -th lattice site is

$$s_{\mathbf{a}} = k_{\text{B}} [n_{\mathbf{a}} \log n_{\mathbf{a}} + (1 - n_{\mathbf{a}}) \log(1 - n_{\mathbf{a}})] / n_{\mathbf{a}} . \quad (2.52)$$

for the central lattice site,  $s_0 \approx 0.6k_{\text{B}}$ . Summing over all sites, the mean entropy per particle is

$$S = \sum_{\mathbf{a}} n_{\mathbf{a}} s_{\mathbf{a}} / N \approx 1.9k_{\text{B}} . \quad (2.53)$$

The (dimensionless) average potential energy is

$$\epsilon = \sum_{\mathbf{a}} n_{\mathbf{a}} u_{\mathbf{a}} \approx 1.4 . \quad (2.54)$$

The (dimensionless) Fermi energy  $\epsilon_F$  is implicitly defined via

$$N = \sum_{u_{\mathbf{a}} \leq \epsilon_F} 1 \rightarrow \epsilon_F \approx 2.0 , \quad (2.55)$$

yielding a degeneracy parameter

$$\epsilon / \epsilon_F \approx 0.7 . \quad (2.56)$$

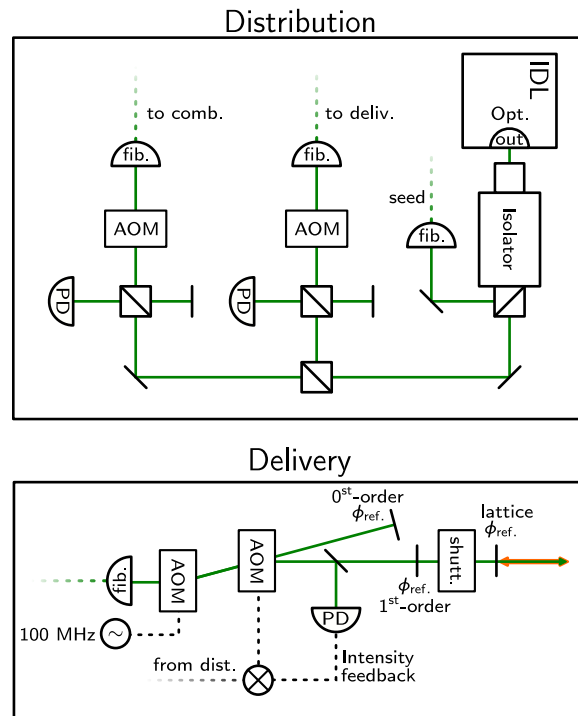


Figure 2.17: Clock laser layout. The clock light used to probe the atoms is derived from an injection locked diode seeded with light from a ULE-cavity stabilized ECDL and further stabilized to the cryogenic reference cavity via an optical frequency comb. Phase noise from the optical fiber is canceled by comparing light returned from the apparatus to a phase reference inside the “distribution center”.

### 2.3.9 Clock spectroscopy

With our lattice-trapped band-insulator at hand, we are now prepared to perform coherent clock spectroscopy, using laser light at  $\omega_{\text{clk}} \approx 429$  THz phase stabilized to a cryogenic silicon reference cavity [41, 42]. The probe laser exhibits white frequency noise on timescales of a few seconds, where the RMS difference in phases over a time interval  $\Delta t$  is approximately  $\sqrt{\langle \Delta \phi^2(\Delta t) \rangle} / \Delta t \approx 90$  mrad.  $\text{s}^{-1}$  [41]. In order to measure the relative detuning  $\omega_{eg,c}$  between the probe laser and the clock transition, we apply various spectroscopic sequences prior to measuring the final atomic populations.

#### 2.3.9.1 Rabi spectroscopy

A particularly simple method, colloquially referred to as **Rabi spectroscopy**, for extracting information regarding atomic transition frequencies involves applying a near resonant light for a time interval

$T_c$  then subsequently measuring the atomic populations. Denoting the final state  $\hat{\rho}(T_c) = \mathcal{U}_c \hat{\rho}(0)$ , solving Eq. 2.18 in the  $\gamma_{eg} \rightarrow 0$  limit with the initial conditions  $\langle \hat{Z}_{eg} \rangle_0 = Z_0$  and  $\langle \hat{S}_{eg} \rangle = \langle \hat{S}_{eg}^\dagger \rangle = 0$  results in the final spin-projection

$$\langle \mathcal{R}_c^\dagger \hat{Z}_{eg} \rangle = Z_0 \frac{\bar{\omega}_{eg,c}^2 + \Omega_{eg,c}^2 \cos\left(T_c \sqrt{\bar{\omega}_{eg,c}^2 + \Omega_{eg,c}^2}\right)}{\bar{\omega}_{eg,c}^2 + \Omega_{eg,c}^2} \quad (2.57)$$

This result is more conveniently expressed as the following fit-function, given in terms of the ordinary frequencies,  $\nu_c = \omega_c/2\pi$  and  $\nu_{eg} = \omega_{eg}/2\pi$ , and the resonant oscillation period  $T_{eg,c} = 2\pi/\Omega_{eg,c}$  for the purposes of determining the microscopic parameters  $\{\nu_{eg}, T_{eg,c}\}$  from experimentally observed population differences  $Z_{\text{obs}}(\nu_c, T_c)$  with known inputs  $\{\nu_c, T_c\}$ :

$$Z_{\text{fit}}(\nu_c, T_c, \nu_{eg}, T_{eg,c}, Z_0, Z_\infty) = Z_0 \left\{ 1 - 2 \left[ \frac{\sin(\mathcal{T}\mathcal{D})}{\mathcal{D}} \right]^2 \right\} + Z_\infty \quad (2.58)$$

$$\mathcal{T}(T_c, T_{eg,c}) = \pi T_c / T_{eg,c}$$

$$\mathcal{D}(\nu_c, \nu_{eg}, T_{eg,c}) = \sqrt{1 + (\nu_c - \nu_{eg})^2 T_{eg,c}^2}$$

where we have introduced  $Z_\infty$  as a phenomenological parameter characterizing a non-zero signal independent of  $\{\nu_c, T_c\}$ .

Fig. 2.18 shows a resonant ‘‘Rabi flop’’ varying the pulse area over the interval  $\theta \in [0, 2\pi]$ . Computing the noise between shots with similar pulse areas reveals the quantum projection noise, corresponding to the binomial distribution of atoms being projected into either clock state.

Assuming an estimate  $\bar{\nu}_{eg,c}^{\text{est}}$  of  $\bar{\nu}_{eg,c}$  can be made to within  $\bar{\nu}_{eg,c}^{\text{est}} T_c \ll 1$  for fixed  $T_c$ , differentiating Eq. 2.58 with respect to  $\bar{\nu}_{eg,c} = \nu_c - \nu_{eg}$  and  $T_{eg,c}$ , suggests maximal information regarding  $\bar{\nu}_{eg,c}$  is obtained for  $T_c^{-1} T_{eg,c}^{\text{opt}} \approx 1.88$  and  $T_c |\bar{\nu}_{eg,c}^{\text{opt}}| \approx 0.375$ , whereby observed population differences  $\Delta Z_{\text{obs}} = [Z_{\text{obs}}|_{\text{sgn}(\bar{\nu}_{eg,c})=+1} - Z_{\text{obs}}|_{\text{sgn}(\bar{\nu}_{eg,c})=-1}]/2$  can be converted into frequency measurements according to  $\nu_{eg} - \nu_{eg}^{\text{est}} = 2\pi \tau_c^{-1} C_{\text{Rab}} \Delta Z_{\text{obs}} / Z_0$  with  $C_{\text{Rab}} \approx 1.64$ . Fig. 2.19 shows a ‘‘Rabi line-scan’’ obtained by varying the probe detuning with a fixed pulse area  $\theta = \pi$ , and pulse-length  $T \approx 4$  s.

### 2.3.9.2 Ramsey Spectroscopy

An alternative spectroscopic method, colloquially referred to as **Ramsey spectroscopy**, involves stroboscopic application of resonant light in between periods of free-evolution. Evolving Eq. 2.18, starting

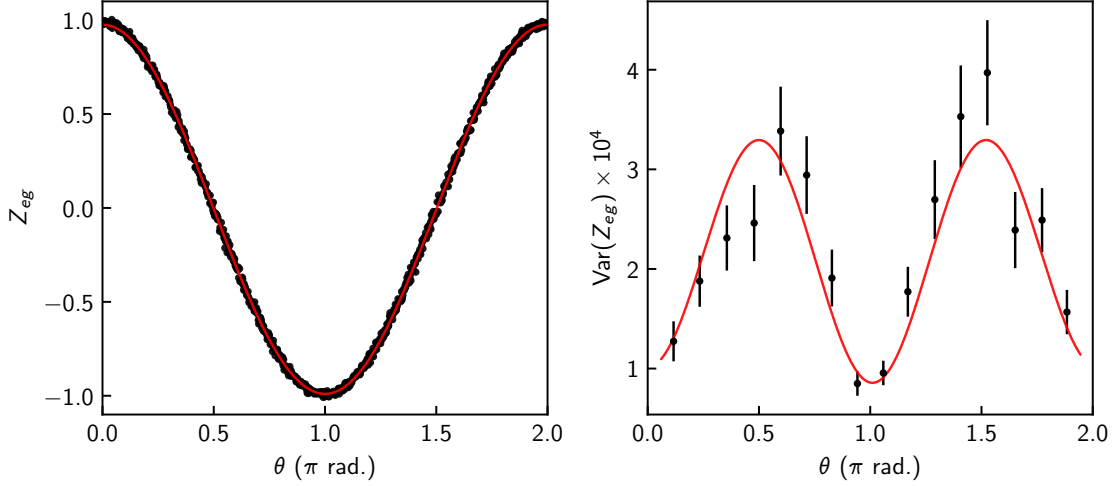


Figure 2.18: Rabi “flop” and quantum projection noise calibration. The differential state projection  $\langle \hat{Z}_{eg} \rangle = \langle \hat{P}_e - \hat{P}_g \rangle$  is shown as a function of pulse area  $\theta$  for fixed, resonant detuning  $\omega_{eg,c} \approx 0$ . Computing the relative noise between individual experimental shots and the fitted response (red line) reveals a  $Z_{eg}$  dependent variance according to  $\text{Var}(Z_{eg}) \sim (1 - Z_{eg}^2)/N$ . Allowing for a state-independent technical noise term, fitting the amplitude of the noise term allows for a determination of the total number of atoms  $N \approx 4 \times 10^3$ .

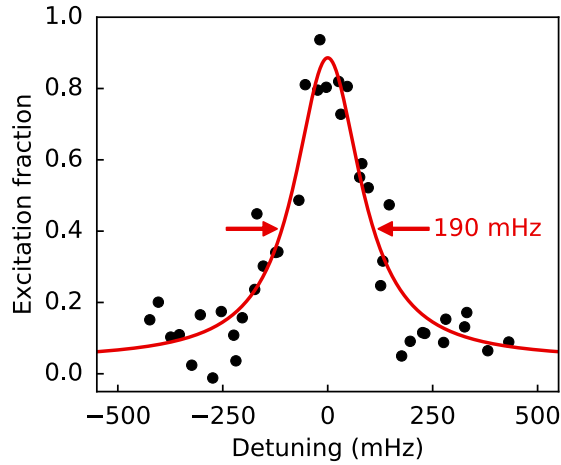


Figure 2.19: Rabi linescan obtained with a 4 s interrogation time.

at a time  $\tau_c$ , for a pulse-duration  $T_c = \theta_{eg,c} T_{eg,c} / 2\pi$  in the limit  $\bar{\omega}_{eg,v} \Omega_{eg,v}^{-1} \ll 1$  yields

$$\begin{aligned}
 \langle \mathcal{U}_c^\dagger \hat{S}_{eg}^+ \rangle &= \cos^2(\theta_{eg,c}/2) \langle \hat{S}_{eg}^+ \rangle + \sin^2(\theta_{eg,c}/2) (\zeta_{eg,c}^*)^2 \langle \hat{S}_{eg}^- \rangle - \frac{i}{2} \zeta_{eg,c}^* \sin(\theta_{eg,c}) \left( \langle \hat{S}_{eg}^+ \hat{S}_{eg}^- \rangle - \langle \hat{S}_{eg}^- \hat{S}_{eg}^+ \rangle \right) \\
 \langle \mathcal{U}_c^\dagger \hat{S}_{eg}^+ \hat{S}_{eg}^- \rangle &= \cos^2(\theta_{eg,c}/2) \langle \hat{S}_{eg}^+ \hat{S}_{eg}^- \rangle + \sin^2(\theta_{eg,c}/2) \langle \hat{S}_{eg}^- \hat{S}_{eg}^+ \rangle - \frac{i}{2} \sin(\theta_{eg,c}) \left( \zeta_{eg,c} \langle \hat{S}_{eg}^+ \rangle - \zeta_{eg,c}^* \langle \hat{S}_{eg}^- \rangle \right) \\
 \langle \mathcal{U}_c^\dagger \hat{S}_{eg}^- \hat{S}_{eg}^+ \rangle &= \cos^2(\theta_{eg,c}/2) \langle \hat{S}_{eg}^- \hat{S}_{eg}^+ \rangle + \sin^2(\theta_{eg,c}/2) \langle \hat{S}_{eg}^+ \hat{S}_{eg}^- \rangle + \frac{i}{2} \sin(\theta_{eg,c}) \left( \zeta_{eg,c} \langle \hat{S}_{eg}^+ \rangle - \zeta_{eg,c}^* \langle \hat{S}_{eg}^- \rangle \right)
 \end{aligned}
 \tag{2.59}$$

Stringing together two pulses, for an initial state with  $\langle \hat{S}_{eg}^+ \hat{S}_{eg}^- \rangle = (1 + Z_0)/2$ ,  $\langle \hat{S}_{eg}^- \hat{S}_{eg}^+ \rangle = (1 - Z_0)/2$ , and  $\langle \hat{S}_{eg}^- \rangle = \langle \hat{S}_{eg}^+ \rangle = 0$ , the final population difference is given as

$$\begin{aligned} \langle \mathcal{U}_{eg,c_1}^\dagger \mathcal{U}_{eg,c_2}^\dagger \hat{Z}_{eg} \rangle &= Z_0 \left[ \cos(\theta_{eg,c_1}) \cos(\theta_{eg,c_2}) - \frac{1}{2} \sin(\theta_{eg,c_1}) \sin(\theta_{eg,c_2}) (\zeta_{eg,c_1} \zeta_{eg,c_2}^* - \zeta_{eg,c_1}^* \zeta_{eg,c_2}) \right] \\ &= Z_0 [\cos(\theta_{eg,c_1}) \cos(\theta_{eg,c_2}) - \sin(\theta_{eg,c_1}) \sin(\theta_{eg,c_2}) \cos[\phi_{eg,c_1}(\tau_{c_1}) - \phi_{eg,c_2}(\tau_{c_2})]] \end{aligned} \quad (2.60)$$

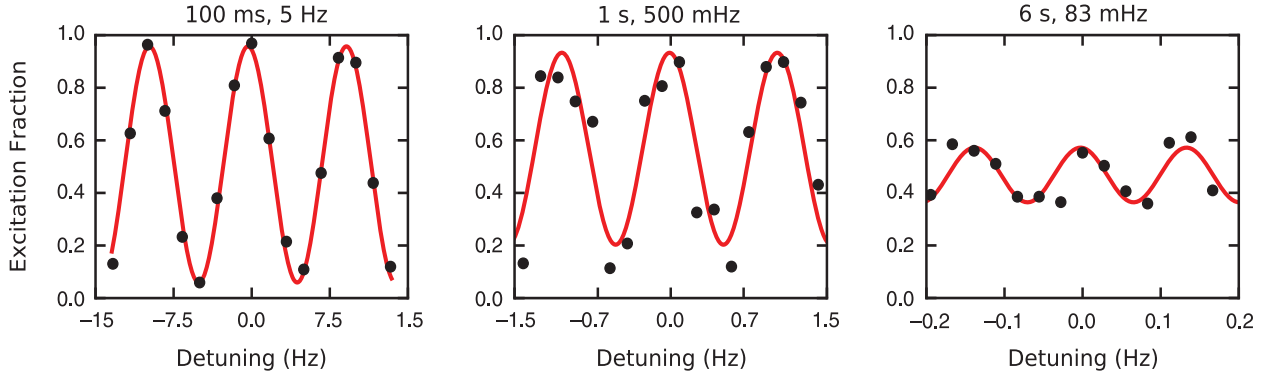


Figure 2.20: Ramsey linescans obtained with various dark times.

Similarly to our analysis of Rabi spectroscopy, maximal information regarding  $\bar{\nu}_{eg,c}$  is obtained for  $\theta_{eg,c_1} = \theta_{eg,c_2} = \pi/2$  and  $\arg(\zeta_{eg,c_1} \zeta_{eg,c_2}^*) = \pm\pi/2$ , at which point  $\nu_{eg} - \nu_{eg}^{\text{est}} = 2\pi\tau_{c_1,c_2}^{-1} C_{\text{Ram}} \Delta Z_{\text{obs}}/Z_0$  with  $C_{\text{Ram}} = 1$

### 2.3.10 Imaging spectroscopy

Comparing global atomic responses to the probe laser frequency is sensitive to noise processes in both the atomic signal as well as the probe laser's phase fluctuations. Spatially resolving the spectroscopic signals, turns out to be a very powerful tool for measuring differential clock shifts between differential regions of the cloud, as phase fluctuations of the probe laser provide only a global offset to an imaged signal [33]. Example images of spatially resolved clock signals are shown in Fig. 2.21 for a single, short  $\theta = \pi/2$  Rabi pulse.

The power of this technique is emphasized in Fig. 2.22 for a somewhat artificial perturbation given by a magnetic field gradient along the x-axis. After the spectroscopic sequence, the local magnetic field

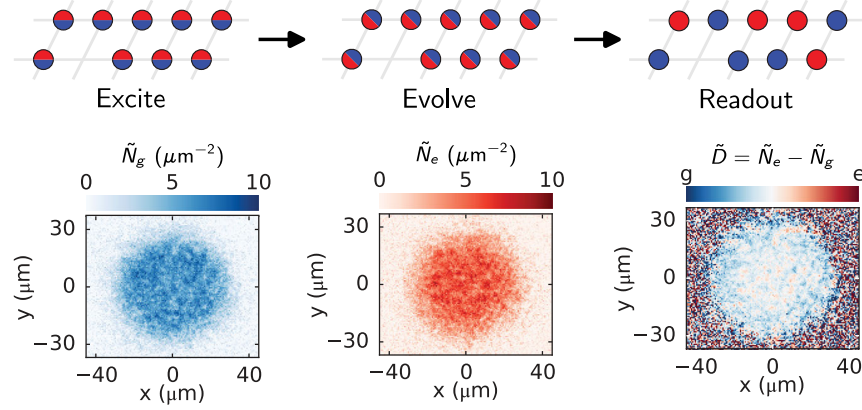


Figure 2.21: Imaging clock signals. At the end of a spectroscopic sequence, column-densities of the atomic populations  $\tilde{N}_g$  and  $\tilde{N}_e$  are imaged onto a sCMOS camera with a  $\sim 1 \mu\text{m}$  resolution. The sum and difference signals  $\tilde{S} = \tilde{N}_g + \tilde{N}_e$  and  $\tilde{D} = \tilde{N}_e - \tilde{N}_g$  are then computed, and reveal spatial dependencies of probe-laser detunings  $\omega_{eg,c}$ . The noise in the difference signal can be largely attributed to quantum projection noise which is then low-pass filtered by the diffraction limited imaging system with a  $1/e^2$  radius optical resolution of  $1.1 \mu\text{m}$ .

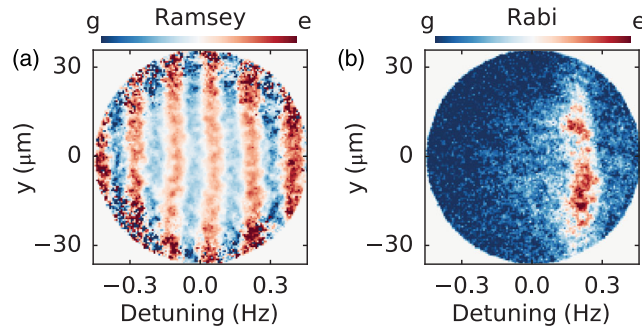


Figure 2.22: Imaging Ramsey and Rabi linescans. Applying a magnetic field gradient transverse to the imaging axis allows for single shot linescans, with coherent interaction times of 6 s and 8 s for Ramsey and Rabi sequences, respectively. In the case of Ramsey spectroscopy, independent of fluctuations of the instantaneous laser phase, one can always determine the relative frequency (or specifically in this case, the local magnetic field) between two regions by simply counting the number of fringes between the regions.

$B_z = x \frac{d}{dx} B_z$  is mapped onto the atomic populations, according to Eq. 2.60,  $D(x) \propto \cos(\delta\mu B_z(x)T + \phi)$

where  $\phi$  is a global phase offset subject to shot-to-shot fluctuations due to the finite laser phase noise.

In this sense the atomic cloud, having a finite spatial extent is then a magnetic gradiometer.

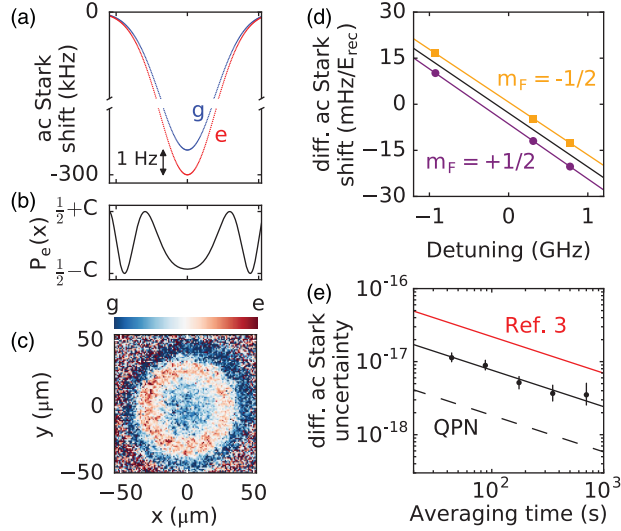


Figure 2.23: Imaging differential ac Stark shifts. Away from the magic condition, the vertical lattice laser, produces a spatial clock signal dependent on the local lattice intensity  $I_c(\mathbf{r}) \propto r^2$ . Fitting the observed signal to the function  $P_e(\mathbf{r}) = \frac{1}{2}[1 + C \cos(\phi + \delta\alpha(\omega_c)r^2)]$  for various  $\omega_c$  allows for rapid determination of the magic detuning.

As a more practical example, imaging spectroscopy is frequently used to determine optimal lattice laser optical frequencies by imaging the differential ac Stark shifts. Since the intensity of the vertical lattice beams varies across the atomic sample  $I \propto x^2 + y^2$ , any deviations of the differential polarizability  $\delta\alpha$  from the magic condition  $\delta\alpha = 0$  results in an atomic response  $D(x) \propto \cos(\delta\alpha I(x^2 + y^2)T + \phi)$ . In this manner we are able to rapidly determine optimal optical frequencies of each lattice beam.

Fig. 2.24 characterizes the achievable signal-to-noise ratios of differential frequency measurements between two regions of the optical lattice. For coherent interrogation times  $T$  short as compared to the decoherence rate  $\Gamma$ , the measurement instability improves rapidly as  $T^{-1}$ . The instability then reaches a maximum at  $\Gamma T = 1/2$  before slowly worsening at longer interrogation times.

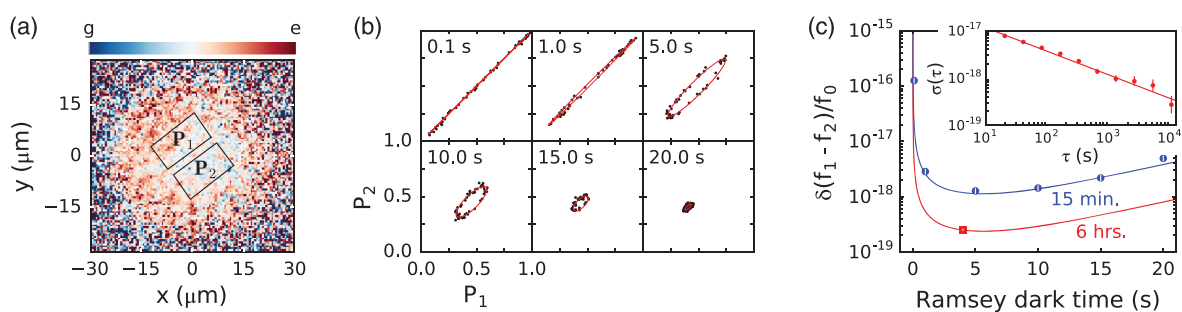


Figure 2.24: Imaging differential clock signals. Clock laser noise provides a common-mode signal between individual measurements, such that the spatial dependence of differential frequency shifts is immune to laser noise. (a) Regions 1 and 2 over which mean excitation probabilities are computed. (b) Parametric plots of  $P_e^{(1)}$  versus  $P_e^{(2)}$  for various dark times  $\tau \in [100 \text{ ms}, 20 \text{ s}]$ . Fitting the eccentricity of the observed ellipses determines the relative frequency shifts. As will be detailed in Ch. 4, contrast decay is due to Raman scattering of optical lattice photons. (c) Relative instabilities of the spatial frequency shift determinations versus  $\tau$ . (c, inset) Relative instability versus averaging time, ultimately reaching a sub- $10^{-18}$  uncertainty after 30 minutes of averaging.

## Chapter 3

### Spectroscopy of atomic collisions

While the spectra presented in the previous chapter were obtained using nuclear-spin polarized gasses where the fraction of doubly occupied sites was exponentially suppressed by the lattice band gap energy  $\omega_{\text{bg}}$ ,  $\delta_{gg'}^{\mathbf{r}} \langle \hat{P}_g \hat{P}_{g'} \rangle \propto e^{-\mu/\omega_{\text{bg}}}$ , the introduction of additional spin components provided an opportunity to investigate ultra-cold collisions in tightly confined harmonic traps, as reported in Ref. [48]. The key advantage over previous work studying ultra-cold collisions in one-dimensional optical lattice clocks [24, 49], is twofold: (1) in a cubic lattice, atoms are tightly confined in all three spatial dimensions, and pair-wise  $s$ -wave interaction energies are on the order of 1 kHz, as opposed to sub 1 Hz in one-dimensional lattices. (2) within a single cubic lattice site, the unperturbed density distributions are characterized only by the band gaps of each of the three lattice beams, and no thermal averaging over motional degrees of freedom is required. These properties then enabled an order-of magnitude improvement in two  $s$ -wave scattering lengths  $a_{eg}^+$  and  $a_{eg}^-$ , and additionally the first reported measurements of molecular three-body loss rates in the collision channels  $egg^+$  and  $egg^-$ .

#### 3.1 Theoretical background

In the deep, isotropic lattice limit  $V_{\text{lat}}/E_{\text{lat}} \gg 1$ , we may treat individual lattice sites as approximately uncoupled harmonic oscillators

$$\begin{aligned} \hat{h}_0 &= \sum_i \frac{1}{2} \left( \frac{\hbar}{m} |\mathbf{k}_i|^2 + \frac{m}{\hbar} \omega_{\text{ho}}^2 |\mathbf{r}_i|^2 \right) \hat{P}_i \\ &= \sum_i \frac{1}{2} \omega_{\text{ho}} \left( |\bar{\mathbf{k}}_i|^2 + |\bar{\mathbf{r}}_i|^2 \right) \hat{P}_i \end{aligned} \tag{3.1}$$

where we have rescaled  $r_0 \bar{\mathbf{r}} = \mathbf{r}$  and  $\bar{\mathbf{k}} = r_0 \mathbf{k}$  by harmonic oscillator length  $r_{\text{ho}} = (\omega_{\text{ho}}/\lambda c)^{\frac{1}{2}}$ . In three spatial dimensions, the eigenstates with no angular momentum ( $l = \langle \bar{\mathbf{r}}_i \times \bar{\mathbf{k}}_i \rangle = 0$ ) may be given as,

$$\begin{aligned} \psi_{n_i}^{\text{ho}}(\bar{\mathbf{r}}_i) &= \left( \frac{1}{2\pi} \frac{\Gamma(n_i + 1)}{\Gamma(n_i + \frac{3}{2})} \right)^{\frac{1}{2}} \exp\left(-\frac{1}{2}|\bar{\mathbf{r}}_i|^2\right) L_{n_i}^{(\frac{1}{2})}(|\bar{\mathbf{r}}_i|^2) \\ \Rightarrow \hat{H}_0 = \langle \hat{h}_0 \rangle &= \sum_i \omega_{\text{ho}} \left( 2n_i + \frac{3}{2} \right) \hat{P}_i^{\text{ho}} \\ &\equiv \sum_i E_i^{\text{ho}} \hat{P}_i^{\text{ho}} \end{aligned} \quad (3.2)$$

In describing pairs of interacting atoms we substitute  $i \rightarrow ij$  into the above equations with  $|\bar{\mathbf{r}}_{ij}| = |\bar{\mathbf{r}}_i - \bar{\mathbf{r}}_j|$  being the distance between the two atoms and  $m_{ij} = m_i m_j / (m_i + m_j)$  being the reduced mass. Following Ref. [50] we may compute the interaction energies  $U_{ij} = (E_{ij}^s - E_{ij}^{\text{ho}})$  corresponding to the addition of a regularized effective potential [51]

$$\hat{h}^{\text{eff}} = 4\pi\omega_{\text{ho}} \left( \bar{a}_{ij} - \bar{E}_{ij}^s \bar{r}_{ij}^{\text{eff}} \right) \delta(\mathbf{r}_{ij}) \frac{\partial}{\partial \bar{r}_{ij}} \bar{r}_{ij} \hat{P}_{ij} \quad (3.3)$$

in place of Eq. 2.33 by exactly solving the Schrödinger equation for  $\hat{h}^s = \hat{h}^{\text{ho}} + \hat{h}^{\text{eff}}$  in the basis of non-interacting eigenstates  $\psi_{ij}^s = \sum_n c_{ij,n} \psi_n^{\text{ho}}$  with coefficients  $c_{ij,n}^* \propto \psi_n^{\text{ho}}(0) / (U_{ij} + 2n_{ij} - 2n)$ . Taking the expectation value of computing the expectation value of  $\hat{h}^s$  for  $\langle \hat{P}_{ij}^s \rangle = 1$  gives

$$\begin{aligned} -\frac{1}{2} \left[ (\bar{U}_{ij} + 2n_{ij}) \bar{r}_{\text{eff}} - \frac{1}{\bar{a}_{ij}} \right] &= \frac{\Gamma[-\frac{1}{2}(\bar{U}_{ij} + 2n_{ij})]}{\Gamma[-\frac{1}{2}(\bar{U}_{ij} + 2n_{ij} + 1)]} \\ \Rightarrow \bar{U}_{ij} &\approx \left( \frac{4}{\pi} \right)^{\frac{1}{2}} \binom{n_{ij} + \frac{1}{2}}{n_{ij}} \bar{a}_{ij} \quad \text{for } \bar{a}_{ij} \ll 1 \end{aligned} \quad (3.4)$$

where  $\bar{U}_{ij} = U_{ij}/\omega_{\text{ho}}$ .

We may now give the following effective Hamiltonian

$$\hat{H}_s = \sum_{ij} U_{ij} \hat{P}_{ij} \quad (3.5)$$

where  $U_{ij}$  may be determined numerically from Eq. 3.4, or for  $\bar{a}_{ij} \ll 1$  we may alternatively Taylor expand the effective scattering length  $\bar{a}_{ij}^{\text{eff}}$  for which the above leading-order term gives the exact interaction

energy using the provided expansion coefficients

$$\bar{a}_{ij}^{\text{eff}} = \bar{a}_{ij} + \left(\frac{\pi^{\frac{1}{2}}}{2}\right) \sum_{n=2}^{\infty} \sum_{m=1}^{n-1} \left[ \left(\frac{2}{\pi^{\frac{1}{2}}}\right)^n b_n + c_{nm} \left(\frac{2}{\pi^{\frac{1}{2}}}\right)^{n-m} \left(\frac{3}{2} \bar{r}_{ij}^{\text{eff}}\right)^m \right] \bar{a}_{ij}^n$$

with

$$b_1 = 1, \quad b_2 = 1 - \log 2, \quad b_3 = 1 - \frac{\pi^2}{24} - \frac{3}{2}(\log 2)(2 - \log 2)$$

$$c_{2,1} = 1, \quad c_{3,1} = 2\left(\frac{4}{3} - \log 2\right), \quad c_{3,2} = 1$$

(3.6)

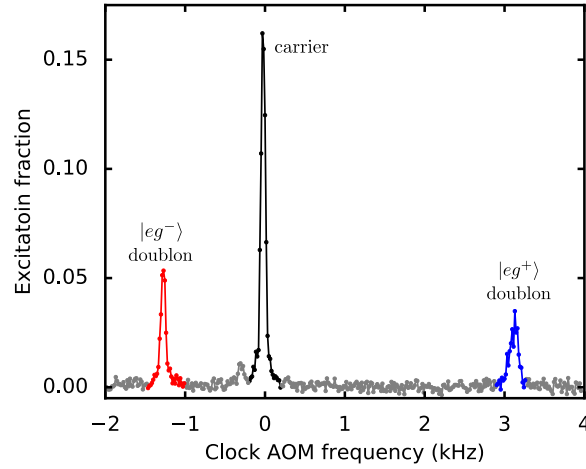


Figure 3.1: Doublon  $s$ -wave collisional shifts. A Rabi linescan was performed on a lattice trapped gas with a significant number of doubly occupied sites. Two main features are present in addition to the singlon signal at zero detuning, correspond to either symmetric or anti-symmetric excitation of the electronic state.

Fig. 3.1 shows a Rabi linescan over a lattice trapped gas initially populating all ten magnetic sub-levels of  $5s5s \ ^1S_0$  and a significant number of doubly occupied sites. Remarkably, only two spectroscopic features are present, in addition to the carrier corresponding to singly occupied sites, despite the entire two-atom Hilbert space containing  $4F(2F + 1) = 380$  states. This can be understood by the fact that the short-range potential, characterized by  $\eta_{ij}^0$  in Eq. 2.31 is determined by the electronic degrees of freedom and for  $J = 0$  in each clock state, the nuclear spin is decoupled from the electronic orbitals.

There are then only four possible electronic orbital configurations:

$$\begin{aligned}
\langle \hat{H}_s \rangle = U_{gg} \quad \text{for} \quad \langle \hat{P}_{gg} \rangle &\equiv \left\langle \sum_{gg'} \hat{C}_g^+ \hat{C}_{g'}^+ \hat{C}_g^- \hat{C}_{g'}^- \right\rangle = 1 \\
\langle \hat{H}_s \rangle = U_{ee} \quad \text{for} \quad \langle \hat{P}_{ee} \rangle &\equiv \left\langle \sum_{ee'} \hat{C}_e^+ \hat{C}_{e'}^+ \hat{C}_e^- \hat{C}_{e'}^- \right\rangle = 1 \\
\langle \hat{H}_s \rangle = U_{eg^+} \quad \text{for} \quad \langle \hat{P}_{eg^+} \rangle &\equiv \left\langle \sum_{eg} \sum_{e'g'} (\delta_{ee'}^m \delta_{gg'}^m + \delta_{ge'}^m \delta_{eg'}^m) \hat{C}_{e'}^+ \hat{C}_{g'}^+ \hat{C}_e^- \hat{C}_g^- \right\rangle = 1 \\
\langle \hat{H}_s \rangle = U_{eg^-} \quad \text{for} \quad \langle \hat{P}_{eg^-} \rangle &\equiv \left\langle \sum_{eg} \sum_{e'g'} (\delta_{ee'}^m \delta_{gg'}^m - \delta_{ge'}^m \delta_{eg'}^m) \hat{C}_{e'}^+ \hat{C}_{g'}^+ \hat{C}_e^- \hat{C}_g^- \right\rangle = 1
\end{aligned} \tag{3.7}$$

We may then identify the density shifts as corresponding to the differences of interaction energies  $(U_{eg^+} - U_{gg})/2\pi \approx -1.3$  kHz and  $(U_{eg^-} - U_{gg})/2\pi \approx 3.1$  kHz. Assuming prior knowledge of the ground state scattering length from Ref. [47], combining independent measurements of the lattice band-gaps and doublon density-shifts can be used to determine the inter-orbital free-space  $s$ -wave scattering lengths  $a_{eg^+}$  and  $a_{eg^-}$ , by inserting the observed density shifts into Eq. 3.4. Numerical values of the scattering lengths are given in Tab. 3.1 and the trap-depth dependence of the density shifts is shown in Fig. 3.2.

Channel $ij$	$a_{ij}/a_0$	$a_{ij}^{\text{vdW}}/a_0$	$b_{ij}/a_0$
$gg$	96.2(0.1)	71.2	127.8
$eg^+$	161.3(0.5)[2.5]	75.2	110.3
$eg^-$	69.1(0.2)[0.9]	75.2	262.2

Table 3.1: Clock-state  $s$ -wave scattering lengths ( $a_{ij}$ ), van der Waals lengths ( $a_{ij}^{\text{vdW}}$ ), and effective ranges ( $b_{ij}$ ). Statistical uncertainties are given in parenthesis and systematic uncertainties in brackets. The  $s$ -wave scattering lengths  $a_{eg^\pm}$  are determined from the observed clock shifts, assuming the quoted value for  $a_{gg}$  as determined by two-photon photo-association in Ref. [47]. The van der Waals lengths are computed from the  $C^6$  coefficients reported in Ref. [49]. The effective ranges  $b_{ij}$  are determined completely by  $a_{ij}$  and  $a_{ij}^{\text{vdW}}$  using Eq. 24 in Ref. [52].

### 3.2 Effective Multi-body interactions

If one carefully inspects Fig. 3.1, there is actually a third interaction peak  $\sim 200$  Hz below the carrier. This turns out to correspond to a signal from triply occupied sites, how then may we make sense of the observed shift and can we predict the location of additional peaks?

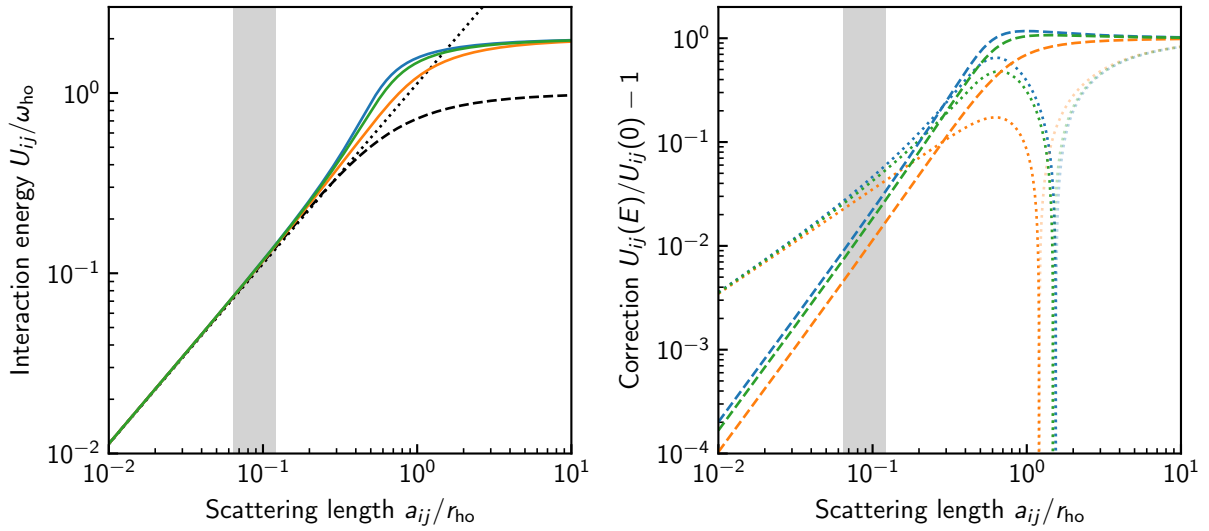


Figure 3.2:  $s$ -wave interaction energies for two atoms in a three-dimensional harmonic oscillator. (Left panel) The solid lines show the results of solving Eq. 3.4 for the  $gg$  (blue),  $eg^+$  (orange), and  $eg^-$  collision channels using the parameter values given in Tab. 3.1. The dotted black line shows the free-space limit  $\bar{U}_{ij} \rightarrow 2\bar{a}_{ij}/\pi^{\frac{1}{2}}$ . The dashed black line shows the solution to Eq. 3.4 in the low-energy limit  $b_{gg} \rightarrow 0$ . (Right panel) The corrections compare the exact values to the two approximations in the left panel, with colors corresponding to the same collision channels. The vertical bar represents the range of experimentally relevant harmonic oscillator lengths corresponding to lattice depths  $V_c/E_c \in [10, 100]$ .

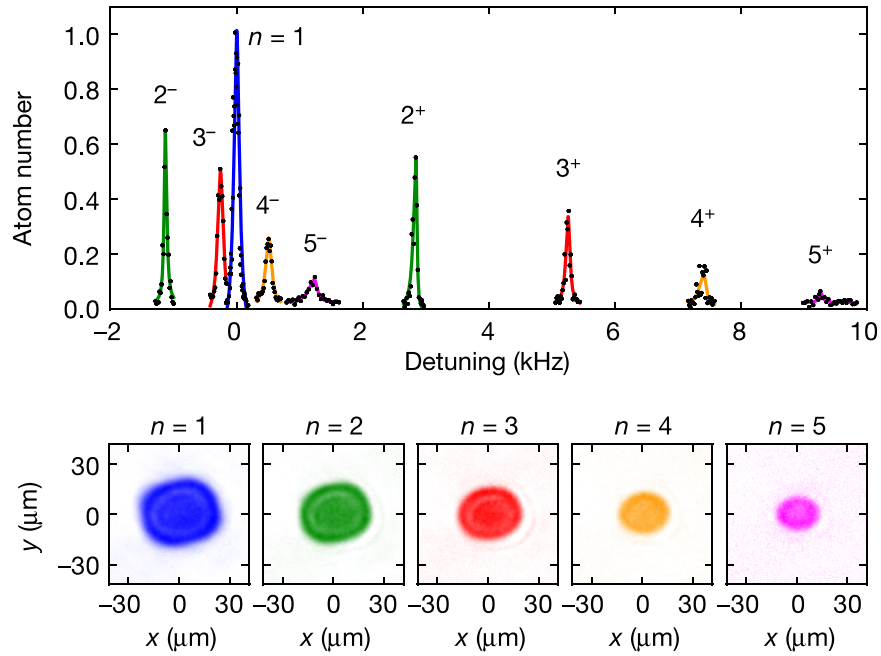


Figure 3.3: Multibody interaction spectrum. (top) Zero-bias-field Rabi linescans of all interaction peaks corresponding to  $n \leq 5$  in a  $\bar{V}_c = 54$  cubic lattice. For each  $n$  the total atom number was varied in order to obtain a peak filling fraction  $n_0 = n$ . (bottom) images of the column integrated densities of the  $n = \{1, \dots, 5\}$  shells for  $n_0 = 5$  were obtained by driving a desired multibody transition, removing all ground state atoms with resonant  $5s5s \ ^1S_0 \leftrightarrow 5s5p \ ^1P_1$  light before moving excited state atoms back to the ground state and subsequently imaging.

Upon first noticing this peak in the lab, we noted that, applying  $\hat{H}_s$  to a three atom state  $\hat{P}_{ijl}$  with at most one atom in the excited clock state gives three additional eigenvalues

$$\begin{aligned} \langle \hat{H}_s \rangle &= 3U_{gg} \equiv U_{ggg} & \text{for } \langle \hat{P}_{ggg} \rangle &= 1 \\ \langle \hat{H}_s \rangle &= U_{gg} + 2U_{eg^+} \equiv U_{egg^+} & \text{for } \langle \hat{P}_{egg^+} \rangle &= 1 \\ \langle \hat{H}_s \rangle &= U_{gg} + \frac{1}{2}(U_{eg^+} + U_{eg^-}) + U_{eg^-} \equiv U_{egg^-} & \text{for } \langle \hat{P}_{egg^-} \rangle &= 1 \end{aligned} \quad (3.8)$$

and while the additional peak roughly agreed with the prediction  $U_{egg^-} \approx 400$  Hz, no additional peaks were found in the immediate vicinity of  $U_{egg^+} \approx 6.2$  kHz.

Following a talk with then visiting JILA fellow Misha Lukin, it became apparent that simply summing pairwise interactions could lead to errors significantly larger than what we had expected.

Applying the formalism given in Ref. [53] which computes effective scattering lengths for multiple harmonically trapped identical bosons, we were able to determine a narrow enough region for which the  $egg^-$  peak could be found within an hour of spectroscopy. Thanks to theory collaborators Michael Perlin and Ana Maria Rey, we were then able accurately model the observed shifts using an effective theory for fermionic atoms. The procedure is as follows.

Anticipating that the addition of an atom to a site occupied by  $n - 1$  atoms modifies all previous interactions, we start with expressing  $\hat{H}_s$  as a power-series in  $n$ -body interactions.

$$\hat{H}_s = \sum_n \hat{H}_s^n = \sum_n \sum_{(i_1 \dots i_n); (j_1 \dots j_n)} U_{(i_1 \dots i_n); (j_1 \dots j_n)}^n \hat{S}_{(i_1 \dots i_n); (j_1 \dots j_n)}^n \quad (3.9)$$

Rather than restricting the available motional states  $\hat{P}_{(i_1 \dots i_n)}^n$  to  $s$ -wave harmonic modes in the center of mass frame, we allow all modes to be populated by individual atoms. However, given the density of states  $g(E_i^{\text{ho}}) \sim n_i$  increases faster than the spatial overlaps  $K_{(i_1 \dots i_n)}^{(j_1 \dots j_n)} = \int d^3\mathbf{r} \psi_{j_1}^* \dots \psi_{j_n}^* \psi_{i_1} \dots \psi_{i_n} \sim |n_j - n_i|^{-\frac{1}{2}}$ , simply assuming  $G^n \propto a_{ij}^n$  leads to divergent interaction shifts. These divergences are “renormalized” by introducing a non-observable counter-term, parameterized by a scattering length  $a_{ij}^{\text{ct}}$  chosen such that when added to  $a_{ij}$  in the coupling constant  $G^n \propto (a_{ij} + a_{ij}^{\text{ct}})^n$  all divergences in the previous order  $G^{n-1}$  are removed. As the exact details of the normalization procedure are quite involved, I simply present the following experimental results from Ref. [48] and refer the reader to Ref. [54] for a precise description.

The effective multibody interactions can clearly be seen when plotting in Fig. 3.5 the observed density shift vs.  $n$  for each branch “ $\pm$ ”.

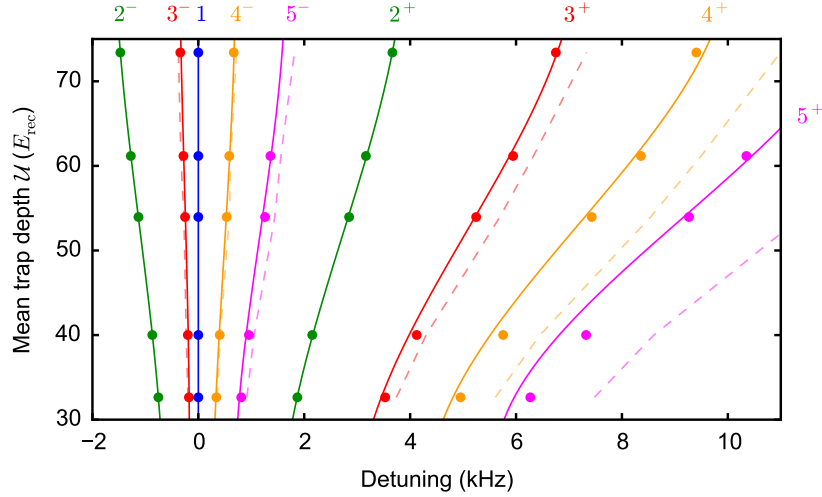


Figure 3.4: Multibody shifts vs.  $V_c$  for  $n \in \{1, \dots, 5\}$ . Data points are shown as solid dots, theory based on effective multi-body interactions as solid lines and two-body theory as dashed lines.

Fig. 3.3 displays all observed, singly excited resonances for a ten nuclear spin component Fermi gas of strontium-87 with at most 5 atoms per site in a  $V_{\text{lat}}/E_c \approx 70$  three-dimensional optical lattice. The spectra were obtained for each  $n$  by successively increasing the number of atoms loaded into the optical lattice such that the central region contained at most  $n$  atoms. Using the computed effective interaction energies a fine scan around the peak could then be performed. For each  $n > 1$ , two peaks are present:  $(eg_1 \dots g_n)^+$  and  $(eg_1 \dots g_n)^-$ . Their locations are given with respect to  $(eg_1 \dots g_{n-1})^\pm$  by  $U_{(eg_1 \dots g_n)^+} \approx U_{(eg_1 \dots g_{n-1})^+} + U_{(eg_1 \dots g_{n-1})^{\text{dir}}}$  and  $U_{(eg_1 \dots g_n)^-} \approx U_{(eg_1 \dots g_{n-1})^+} + U_{(eg_1 \dots g_{n-1})^{\text{ex}}}$ , with the relations being exact after renormalization. Fig. 3.4 show the observed spectrum's dependence on the lattice depth.

The effective multibody interactions can clearly be seen when plotting in Fig. 3.5 the observed density shift vs.  $n$  for each branch “ $\pm$ ”.

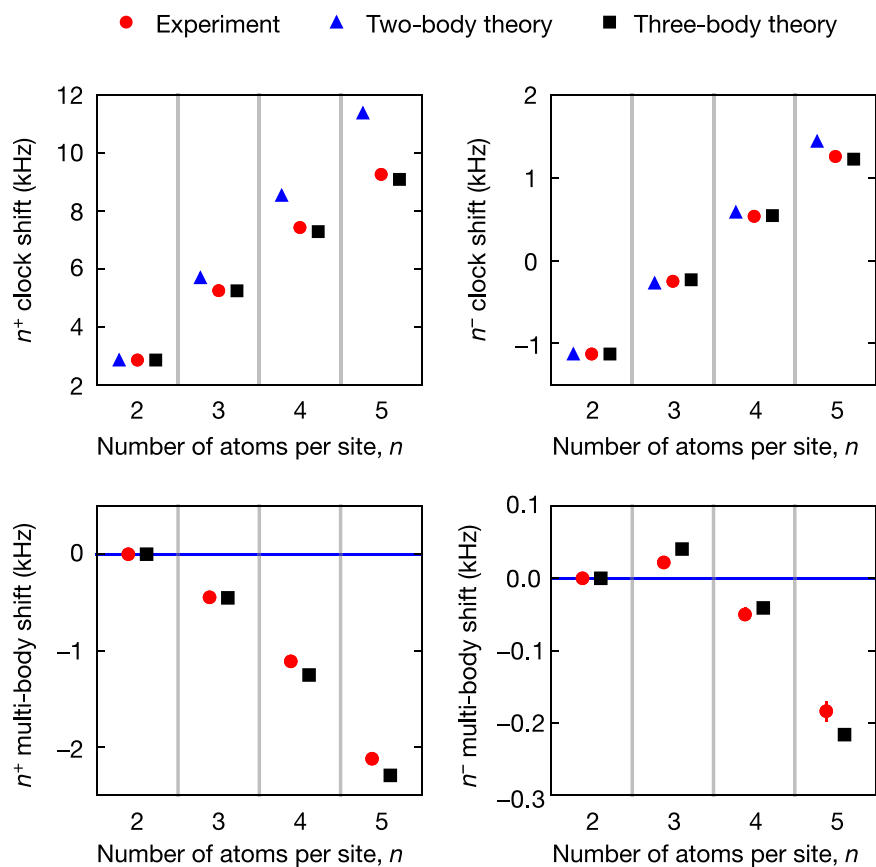


Figure 3.5: Multibody shifts vs.  $n$ . Experimental data are shown as red points, two-body theory as blue triangles, and multi-body theory as black squares. Deviations between the data and the two-body theory grow with  $n$  while the multibody theory at least qualitatively agrees.

### 3.3 Molecular three-body interactions

In addition to the observed clock shifts, the presence of multiple atoms on individual lattice sites is associated with atomic loss. At any finite density, atoms spend time within the van der Waals length of each other. They can become trapped within this molecular potential if by some mechanism the molecular binding energy can be absorbed/released. For atoms in excited electronic states, the molecular binding energy can be released as an outgoing photon. For more than two colliding atoms, two atoms may form a molecular state while the others absorb the binding energy as kinetic energy.

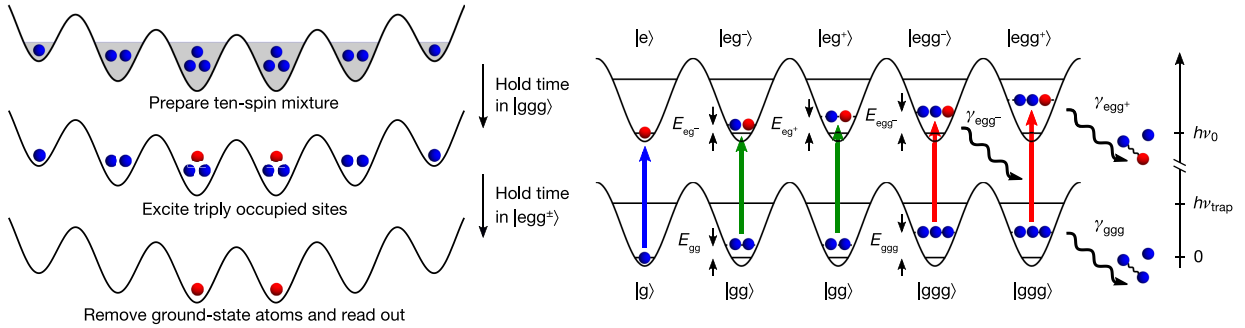


Figure 3.6: Schematic for multibody lifetime measurements. By holding the atoms in the lattice for a variable amount of time before (after) driving a multibody transition, the lifetimes  $\tau_{g\dots}$  ( $\tau_{eg\dots}$ ) are able to determined by counting the total number of atoms in the excited state. Such measurements of recombination rates are advantageous over bulk-gas measurements since the signal is not averages over a range of densities.

Measurements of the lifetimes of the  $n$ -body states then serve as probes of such physics. The measurement scheme is depicted in Fig. 3.6. By holding a manybody state in a lattice for a variable amount of time and then imaging only excited state populations, we are able to extract molecular loss rates  $\tau_{i_n}^{-1}$  defined as

$$\tau_{i_n}^{-1} = \beta_{i_n} \int d^3\mathbf{r} |\psi_{i_n}|^{2n} \quad (3.10)$$

where  $\beta_{i_n}$  is a fixed coefficient for each collision channel. Fig. 3.7 displays the acquired data for various  $n$  and  $V_{\text{lat}}$  and theoretical predictions from José D'Incao obtained from modeling of the molecular potentials.

The measured loss rates are given in Tab. 3.2.

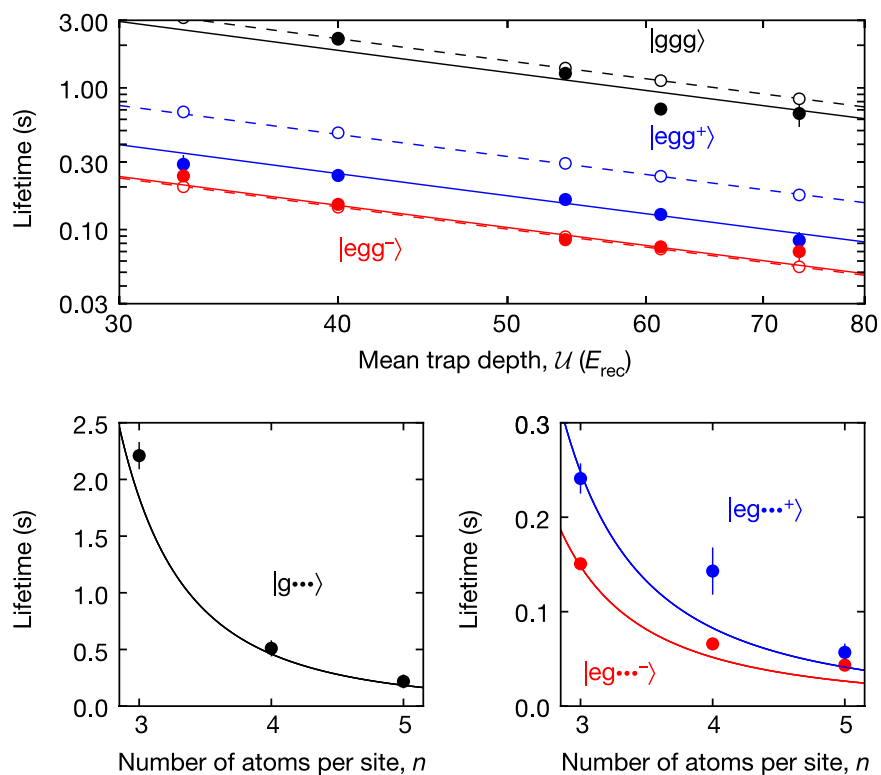


Figure 3.7: Determination of Molecular loss rates for multibody states. (Top panel) Three body recombination rates for the collisional channels  $ggg$ ,  $egg^+$ , and  $egg^-$  in lattice sites occupied by three atoms are shown to scale, according to Eq. 3.10, as  $V^{-3/2}$ . Solid (open) circles represent experimental (numerical) data and solid (dashed) lines show power-law fits. (Bottom panel) molecular loss rates as a function of atom number in a single lattice site. Experimental are shown to roughly scale with the combinatorial expressions given in Eq. 3.11.

Channel $x$	$\beta_x$
$gg$	—
$eg^+$	$2.1(0.2) \times 10^{16} \text{ cm}^3/\text{s}$
$eg^-$	$2.2(0.2) \times 10^{16} \text{ cm}^3/\text{s}$
$ggg$	$2.0(0.2) \times 10^{30} \text{ cm}^6/\text{s}$
$egg^+$	$25(1) \times 10^{30} \text{ cm}^6/\text{s}$
$egg^-$	$15(1) \times 10^{30} \text{ cm}^6/\text{s}$

Table 3.2: Molecular loss rates determined from the data in Fig. 3.7

For  $n$  more than three atoms per site, the expected loss rates are given by combinatorics as

$$\begin{aligned}
\tau_{g\dots}^{-1} &= \tau_{ggg}^{-1} \binom{n}{3} \\
\tau_{eg\dots}^+ &= \tau_{egg^+}^{-1} \binom{n-1}{2} + \tau_{ggg}^{-1} \binom{n-1}{3} \\
\tau_{eg\dots}^- &= \tau_{egg^-}^{-1} \frac{2n}{3n-3} \binom{n-1}{2} + \tau_{egg^+}^{-1} \frac{n-3}{3n-3} \binom{n-1}{2} + \tau_{ggg}^{-1} \binom{n-1}{3}
\end{aligned} \tag{3.11}$$

While for clock operation, one wishes to avoid trapping multiple atoms on individual lattice sites, the above characterizations of  $s$ -wave collisional parameters has proven to be useful in modeling observed density shifts in one-dimensional ‘‘Wannier-Stark’’ optical lattice clocks [55], as well as various proposals involving many-body physics, and more specifically spin-squeezing, in shallow optical lattices [56–59].

## Chapter 4

### Engineering quantum states of matter

In Figs. 2.20 and 2.24, we presented Ramsey fringes for various dark times  $\tau \in [0.1 \text{ s}, 20\text{s}]$ , with the observed contrast decaying with increasing dark time. As shown by the data in Fig. 4.1, this effect turns out to be directly related to the lattice depth. As described in Sec. 4.1 and additionally in Ref. [60], many the observed features can be accurately modeled by Raman scattering of the optical lattice photons. The intensity dependence of the scattering rate  $\tau_R^{-1} \propto V_{\text{lat}}$  motivates operation of the clock in shallow lattices. Extrapolating the high lattice depth data in Fig. 4.1 to lower trap depths suggests a total depth of  $\bar{V}_C = 3 \times 4$  is required to enable coherent interrogation times on the order of the clock transitions 120 s natural lifetime.

There is further motivation to reduce optical trap depths when considering higher-order corrections to the differential ac Stark shifts between the two clock states. Magnetic dipole  $M1$  and Electric quadrupole  $E2$  contributions to the clock state polarizabilities, though relatively minor in absolute scale, obey different scaling laws with respect to the lattice intensity and complicate operation of optical lattice clocks below the  $1 \times 10^{-18}$  level [30, 61]. Other, more technical imperfections such as optical birefringence in viewports can also limit atom-atom coherence through spatially dependent vector ac Stark shifts [31]. Operation in a  $V_{\text{tot}} = 12E_R$  trap should dramatically reduce these effects.

However, in shallow lattices, motional couplings between lattice sites open up additional dephasing mechanisms.

However, in shallow lattices, motional couplings between lattice sites open up additional dephasing mechanisms. Motivated by these conflicting challenges, we discuss a few opportunities to engineer

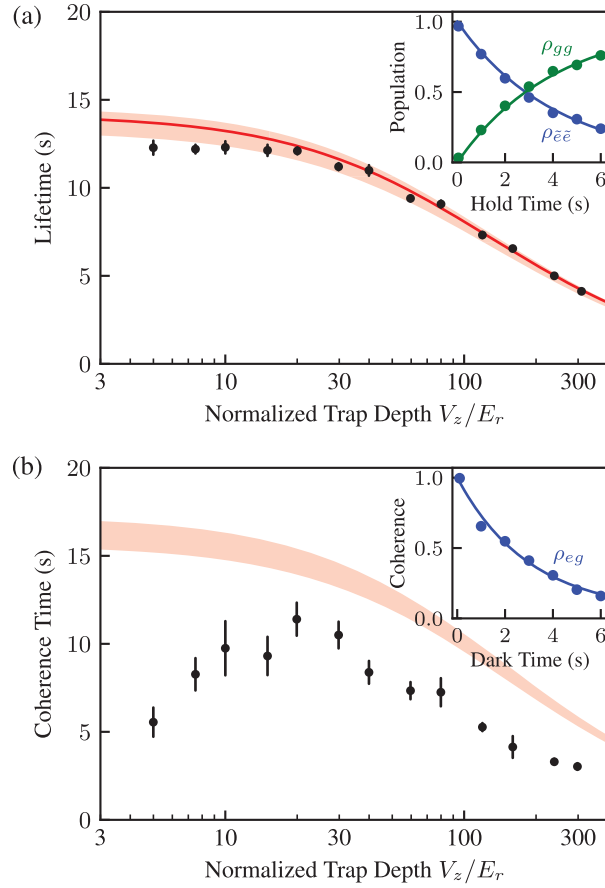


Figure 4.1: Raman scattering of optical lattice photons. Data points in the top (bottom) panel are obtained for each vertical lattice trap depth  $V_z$  by measuring the excited state populations (Ramsey fringe contrast) for various dark times  $T$  and subsequently fitting an exponential decay. Red regions show a no-free-parameter theory model based on Raman scattering of optical lattice photons. The  $V_z \rightarrow 0$  behavior of the theory curve is dominated by contributions from the two other lattice beams  $V_x, V_y \approx 70E_r$ . While the observed populations agree well with the model for all trap depths, the coherences seem to be systematically biased to be 50% lower than what is expected from Raman scattering at large lattice depths  $V_z/E_r > 20$  and follow a qualitatively different trend below  $V_c/E_r < 10$ .

quantum states of matter which can be simultaneously immune to both dephasing mechanisms.

#### 4.1 Off-resonant two-photon scattering

We begin by more precisely defining the Rayleigh/Raman scattering problem. At fourth-order in the electric dipole interaction  $\hat{H}_1$  from Ch. 2 (or equivalently second order in  $\hat{H}_2$ ), for a far-off-resonant coherent state  $A_c$ , single-atom atomic operators evolve in time according to

$$\begin{aligned} \frac{d}{dt} \hat{S}_{ij} &\approx \bar{\mathcal{H}}[\hat{H}_2 \mathcal{T}(\hat{H}_2) \hat{S}_{ij}] \\ &= - \sum_{mn} \left[ \bar{\Gamma}_{mn}^{jm} \hat{S}_{in} + \bar{\Gamma}_{mi}^{nm} \hat{S}_{nj} - 2\tilde{\Gamma}_{jn}^{mi} \hat{S}_{mn} \right] \end{aligned}$$

where

$$\begin{aligned} \tilde{\Gamma}_{jn}^{mi} &\equiv \sum_{\mu\nu} \sum_p \delta(\omega_{cp} + \omega_{nj}) \delta_{im+jn}^\omega \left( \frac{\mathcal{G}_{m\mu;p} \mathcal{G}_{\mu i;c}}{\omega_{\mu i;c}} - \frac{\mathcal{G}_{m\mu;c} \mathcal{G}_{\mu i;p}}{\omega_{m\mu;c}} \right) \left( \frac{\mathcal{G}_{j\nu;c} \mathcal{G}_{\nu n;p}}{\omega_{\nu j;c}} - \frac{\mathcal{G}_{j\mu;p} \mathcal{G}_{\nu n;c}}{\omega_{n\nu;c}} \right) \\ \bar{\Gamma}_{mi}^{jm} &\equiv \sum_{\mu\nu} \sum_p 4\delta(\omega_{pc} + \omega_{mj}) \frac{\mathcal{G}_{j\nu;p} \mathcal{G}_{\nu m;c} \mathcal{G}_{m\mu;c} \mathcal{G}_{\mu i;p}}{(\omega_c^2 - \omega_{\mu m}^2)(\omega_c^2 - \omega_{\nu m}^2)} \left[ (\omega_c^2 + \omega_{\mu m} \omega_{\nu m}) \delta_{ij}^\omega - (\omega_c^2 - \omega_{\mu m} \omega_{\nu m}) \delta_{im+jm}^\omega \right] \end{aligned} \quad (4.1)$$

The contributions from the  $\bar{\Gamma}$  ( $\tilde{\Gamma}$ ) terms can be considered Rayleigh (Raman) scattering process as they do (not) conserve the populations  $\hat{P}_i$ . It turns out that the dephasing of the clock states  $\frac{d}{dt} \hat{S}_{eg}$  due to Rayleigh scattering are exactly zero for the magic wavelength lattice where the ac polarizabilities are matched. This is due to Rayleigh scattering being proportional to the exact combination of dipole matrix elements and weighting factors as the ac polarizability [62]. Photons are scattered off an atom in either clock state at the exact same rate and with the same spatial distribution, such that this process leaves atoms indistinguishable. Raman scattering however, affects both the clock state populations and coherences.

By energy conservation and parity selection rules, Raman scattering can transfer excited state populations only within the  $5s5p \ ^3P_J$  manifold:  $5s5p \ ^3P_0 \leftrightarrow 5s5p \ ^3P_{1,2}$ . Fig. 4.2 shows calculated Raman scattering rates out of the excited clock state as a function of optical wavelength for a  $1E_c$  lattice, using the parameters in Tab. 2.1-2.3.

For convenience, we here list approximate formulae for estimating depopulation and decoherence

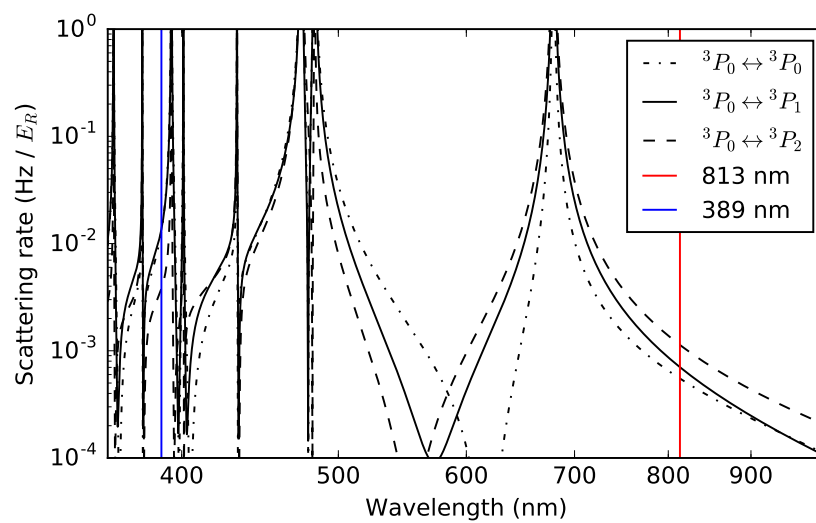


Figure 4.2: Raman scattering rates out of  $5s5p\ ^3P_0$  vs. lattice wavelength. Calculated scattering rates out of  $^3P_0$  as a function of trap wavelength for a fixed trap depth  $\bar{V}_c = 1$  with  $E_c = 2\pi^2\hbar/m\lambda^2$ .

rates in a  $\omega_c \approx 368$  THz retro-reflected lattice in terms of the normalized trap depth  $\bar{V}_c = V_c/E_c$ :

$$\begin{aligned}\frac{d}{dt}\hat{P}_e &= \Gamma_{ee}^1 \bar{V}_c \left(1 - \frac{1}{2}\bar{V}_c^{-1/2}\right) + \Gamma_{ee}^0 \\ \frac{d}{dt}\hat{S}_{eg} &= \Gamma_{eg}^1 \bar{V}_c \left(1 - \frac{1}{2}\bar{V}_c^{-1/2}\right) + \Gamma_{eg}^0\end{aligned}\tag{4.2}$$

with

$$\begin{aligned}\Gamma_{ee}^1 &= 5.7(3) \times 10^{-4} \text{ s}^{-1}, & \Gamma_{ee}^0 &= 9(1) \times 10^{-3} \text{ s}^{-1} \\ \Gamma_{eg}^1 &= 4.0(2) \times 10^{-4} \text{ s}^{-1}, & \Gamma_{eg}^0 &= 1.2(1) \times 10^{-2} \text{ s}^{-1}\end{aligned}$$

In the above expressions, the non-linear scaling of the scattering rates with lattice depth accounts for the spatial overlap of the atomic density with the laser intensity in the harmonic limit ( $V_i/E_r \gg 1$ ).

While the  $^1S_0$  populations are nominally unaffected by spontaneous Raman scattering (there are no other levels within  $\omega_c$  of the ground state), the ground state can be populated from scattering events in the  $^3P_J$  manifold which place atoms in  $^3P_1$ , which relatively rapidly decays into the ground state. Fig. 4.3 shows a rate-equation simulation of atomic populations starting in the excited clock state, using the scattering rates specified in Eq. 4.2.

Looking back at Fig. 4.1, the modeled population decay agrees quite well with the simulation, however the decoherence rates are systematically biased. We speculate there could be a few reasons for this. Firstly, our calculation treats the atoms as effectively having only two electrons, and effectively absorbing the polarizability of the core electrons into the polarizability of the continuum of states at the ionization threshold. This seems to accurately reproduce all reported measurements of differential polarizabilities in strontium, but potentially ignores additional scattering channels. Another effect that was unmodeled was the potentiality of trapping light induced heating producing atoms in higher bands which could then tunnel around and cause collisionally-induced dephasing. A third mechanism could involve radiative interactions between atoms, as will be discussed in the following chapter.

None-the-less, it is clear from the data that trapping depths should be minimized.

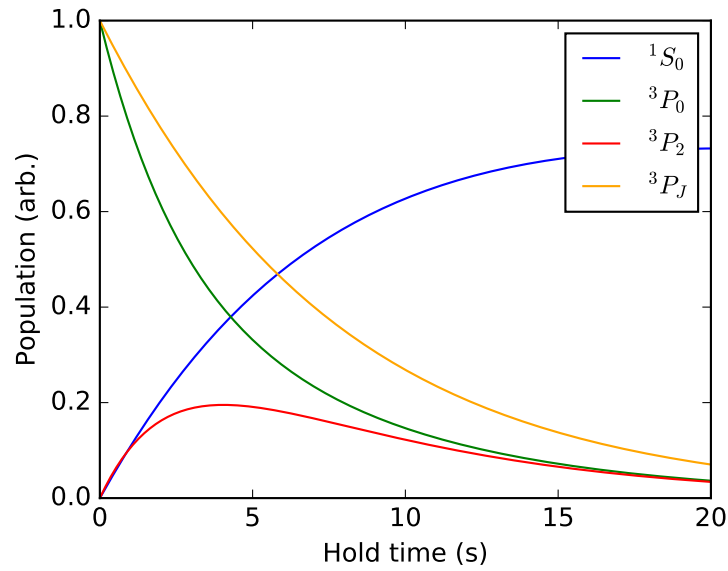


Figure 4.3: Population dynamics due to Raman scattering. Starting with an atom in  $^3P_0$  and a  $V_{\text{tot.}} = 200E_c$  lattice, all populations in the manifold of states  $\{5s5s\ ^1S_0, 5s5p\ ^3P_J\}$  are evolved according to Eq. 4.1, with fixed  $\hat{S}_{ij} = 0$  for  $i \neq j$ . Depopulation of  $^3P_0$  is nearly twice as fast as the population of  $^1S_0$ . This is roughly consistent with the experimental observation that the clock-state decoherence rates and  $^3P_J$ -manifold lifetimes are roughly equal.

## 4.2 Motional dephasing in shallow lattices

The problem with reducing lattice depths too far is that the lattice is there in the first place to reduce motional dephasing. In a shallow enough lattice, the effective mass of atoms becomes small enough that Doppler shifts can be observed [63, 64]. In a deep optical lattice, the ground band energy spectrum, as a function of quasi-momentum, can be approximated in one-dimension as

$$E_{\bar{q}} = -2t \cos(\bar{q}) \quad (4.3)$$

where  $t$  is the tunneling rate, to be obtained numerically from diagonalizing Eq. 2.45. The coherent coupling between clock states obtains a state dependence

$$\zeta_{eg;p} = \sum_m C_{n_g}(\bar{q}_g + \bar{k}_p, \bar{q}_g + \bar{k}_p + 2m) C_{n_e}(\bar{q}_e, \bar{q}_e + 2m) \exp(-i\omega_{eg;p}t) \quad (4.4)$$

Which is non-zero only for  $\bar{q}_g + \bar{k}_p = \bar{q}_e$ , shifting the resonance condition away from the infinite mass limit:  $\omega_p - \omega_{eg}^0 = 2t [\cos(\bar{q}_e + \bar{k}_p) - \cos(\bar{q}_g)]$ . When a degenerate Fermi gas fills all available quasi-momentum states  $\bar{q}_g \in [-\pi, \pi)$ , averaging over all signals gives a Doppler broadening of up to  $4t$ , when  $\bar{k}_p = \pi$ . We accordingly define  $\gamma_t = 4t |\sin(\bar{k})|$  as the motional dephasing rate. For the 368 THz retro-reflected lattice, one has  $\bar{k}_{\text{clock}} = 7\pi/6$  such that one is near maximal sensitivity to Doppler shifts for a given tunneling rate  $t$ , this incentivizes operation in a deep lattice, in contradiction to what we concluded from the Intensity dependence of Raman scattering.

## 4.3 Accordion lattice

Given we now have conflicting desires in optimizing atomic coherence times in the optical lattice, some new experimental techniques are required. The Raman scattering rates are intrinsically tied to the optical intensity of the light, while the Doppler broadening also depends on lattice depth, the periodic momentum dependence opens up an avenue to negating motional dephasing even in a lattice with large tunneling rates. What one needs is a periodic potential with a spacing giving  $\hat{k}_{\text{clock}} = 2\pi$ . As depicted in Fig. 4.4, one could envision accomplishing this by interfering the lattice lasers at some angle other than

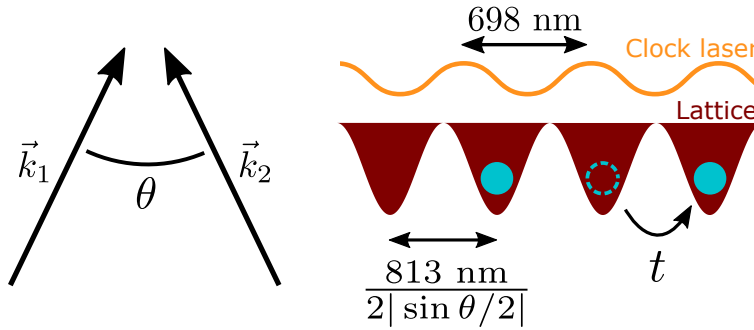


Figure 4.4: Schematic of accordion optical lattice. Two Gaussian beams with wavelength  $\lambda$  interfering at an angle  $\theta$  form a standing wave with period  $a(\theta) = \lambda/2 \sin(\theta/2) \geq \lambda/2$ . Orienting the lattice polarization into the plane maximizes the interference term.

$180^\circ$ , the largest angle at which this condition is satisfied is approximately  $34^\circ$ . Alternatively, optical tweezers are a promising method to create such arrays for smaller numbers of atoms [65–67].

As shown in Fig. 4.5, This scheme can also be conceptualized in real space where an atom tunneling along the propagation direction of the clock laser always sees the same laser phase. Additionally shown are the Hubbard parameters  $t^*$  (kinetic energy) and  $U$  (interaction energy) as well as the motional dephasing rate  $\gamma_t$  as a function of lattice spacing in a  $V_c = 3 \times 4E_c$  cubic lattice, as a function of lattice spacing. At the phase matching condition, motional dephasing is seen to sharply dip below the natural decay rate of the excited clock state. Achieving using interfering laser beams requires angular deviations to be controlled to within the  $10^{-5}$  and  $10^{-2}$  levels for the first and second resonances, respectively.

We now consider whether there are any other major problems associated with operating in such a shallow optical lattice, other than the motional dephasing.

#### 4.3.1 Line pulling

One concern could be that even though coupling between motional states within the ground band can be arranged to not produce motional broadening in the Bragg lattice, how strong will couplings be to other motional bands?

Scalings of the motional energy spectrum versus lattice spacing are given in Fig. 4.6. By visual inspection, the band gaps remain at the few kHz level for relevant lattice spacings, which is significantly

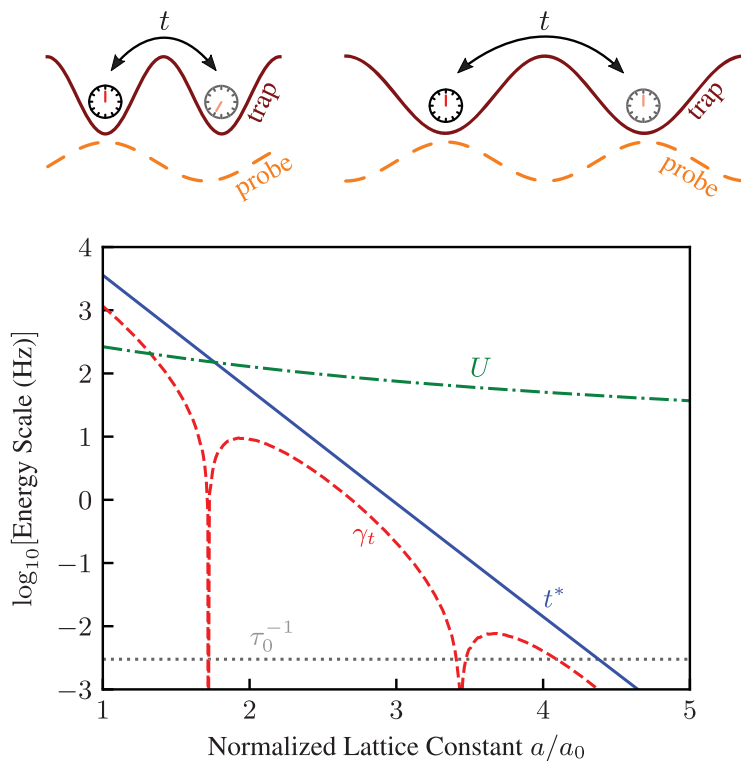


Figure 4.5: Hubbard parameters in a  $3 \times \bar{V}_c = 12$  cubic accordion lattice, plotted as a function of lattice spacing  $a$ , in units of the retro-reflected lattice spacing  $a_0 \approx 407$  nm. The exponential suppression of  $t$  as compared to  $U$  means one can rapidly enter the Mott-insulating regime  $t^* \ll U$  even in nominally shallow lattices.

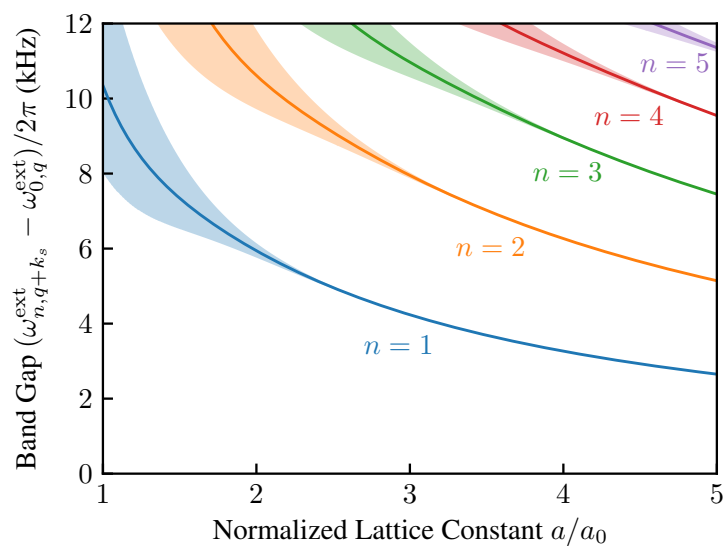


Figure 4.6: Single particle energy spectrum in a in a  $\bar{V}_c = 4$  one-dimensional accordion lattice. Shaded regions show the range of energies for all quasi-momenta,  $q$ . Solid lines show mean values within a single band  $n$ .

larger than relevant Rabi coupling rates. To be more quantitative, we may compute the residual signal from off-resonant excitation (line-pulling) as follows.

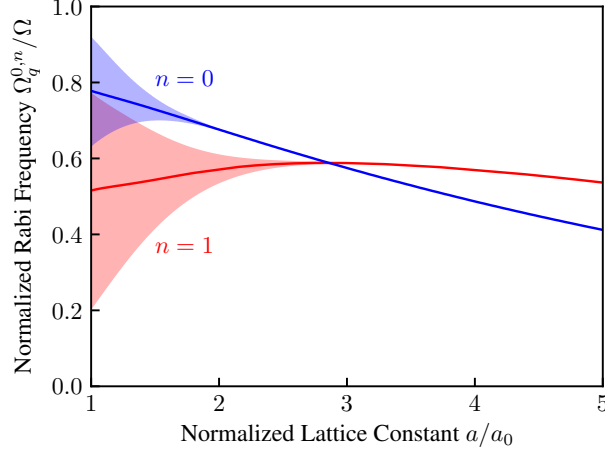


Figure 4.7: Single atom Rabi couplings in a  $\bar{V}_c = 4$  one-dimensional accordion lattice. Values are normalized by the infinite mass coupling  $\Omega_0$ . Shaded regions show the full range of values for all initial quasi-momenta,  $q$ . Solid lines show mean values withing a single band  $n$ , or equivalently that of a maximally localized atom.

In a Rabi interrogation sequence, an error signal for referencing the clock laser to the atomic transition is typically generated by starting in the state  $|\psi_{\pm}(0)\rangle = |g; n = 0\rangle$ , applying a pulse of duration  $T_{\pi} = \pi/\Omega^{0,0}$  while dithering the detuning between two values  $\Delta_{\pm} \approx \Delta \pm 0.8\Omega$  on successive experimental cycles, then computing the difference in excitation probabilities,  $\epsilon(\Delta) = P_{+} - P_{-}$ . The presence of asymmetric sidebands in the atomic response can then result in a non-zero clock shift,  $\Delta/\omega_0$  for  $\Delta$  satisfying  $\epsilon(\Delta) = 0$ .

We may calculate the quantities  $P_{\pm}$  by first solving the system of coupled differential equations

$$\begin{aligned} \partial_t \langle e; n | \psi_{\pm}(t) \rangle &= -\frac{i}{2} \sum_{n'} \Omega^{n,n'} e^{-i(\Delta_{\pm} + \omega_{n'}^{\text{ext}} - \omega_n^{\text{ext}})t} \langle g; n' | \psi_{\pm}(t) \rangle \\ \partial_t \langle g; n | \psi_{\pm}(t) \rangle &= -\frac{i}{2} \sum_{n'} \Omega^{n',n} e^{i(\Delta_{\pm} + \omega_n^{\text{ext}} - \omega_{n'}^{\text{ext}})t} \langle e; n' | \psi_{\pm}(t) \rangle , \end{aligned} \quad (4.5)$$

then summing

$$P_{\pm} = \sum_n |\langle e; n | \psi_{\pm}(T_{\pi}) \rangle|^2 . \quad (4.6)$$

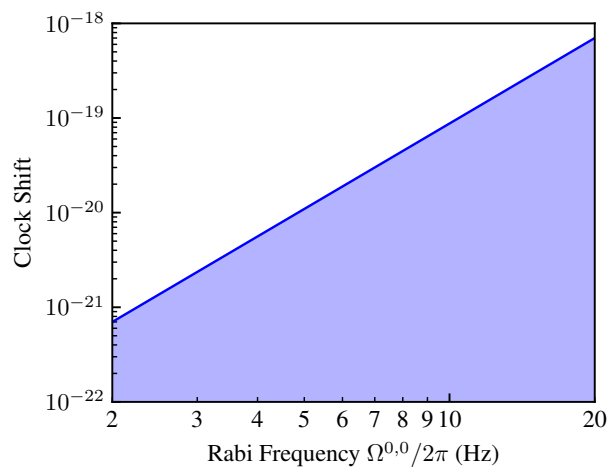


Figure 4.8: Upper bounds on line-pulling clock shifts in a  $\bar{V}_c = 4$  one-dimensional accordion lattice. Upper bounds are computed as a function of coupling strength  $\Omega_{0,1}$  for  $a/a_0 = 5$ ,  $\omega_1^{\text{ext}} - \omega_0^{\text{ext}} = 2.6$  kHz and  $\Omega^{0,1}/\Omega^{0,0} = 1.3$ .

Here, all dependence on  $q$  has been suppressed under the assumption that any variance is negligibly small for  $a/a_0 \gtrsim 3$ . Fig. 4.8 gives the range of clock shifts relevant to our proposal, showing that line pulling effects are suppressed below the  $10^{-19}$  level for  $\Omega/2\pi < 10$  Hz.

### 4.3.2 Collisional effects

Collisional interactions may also significantly effect dynamics in a shallow lattice clock [64]. We investigate these effects with a “toy model” consisting of a double well potential given by the following Hamiltonian.

$$H/\hbar = \sum_x \left[ \frac{\Delta}{4} (n_{x,e} - n_{x,g}) + \frac{U}{2} n_{x,g} n_{x,e} + \frac{\Omega}{2} e^{i\phi_x} c_{x,e}^\dagger c_{x,g} \right] - t \sum_\sigma c_{L,\sigma}^\dagger c_{R,\sigma} + \text{H.c.} \quad (4.7)$$

Here  $c_{x,\sigma}^\dagger$  ( $c_{x,\sigma}$ ) creates (destroys) a fermion with internal state  $\sigma \in \{g, e\}$  in well  $x \in \{L, R\}$ ,  $n_{x,\sigma} = c_{x,\sigma}^\dagger c_{x,\sigma}$ ,  $\Delta = \omega - \omega_0$  is the difference between the frequency of the driving field  $\omega$  from the atomic resonance,  $\omega_0$ ,  $\Omega$  is the Rabi coupling strength, and  $\phi_x = 2\pi \frac{a}{\lambda_{\text{clk}}} \delta_{x,R}$  is the site-dependent phase shift of the clock light, with  $\delta_{i,j}$  being the Kronecker delta function. The two atom spectrum of this Hamiltonian with  $\Omega = 0$ , is shown in Fig. 4.9a.

We simulate Ramsey spectroscopy of one and two atoms in the double well by numerically integrating the Schrödinger equation. A resonant ( $\Delta = 0$ )  $\pi/2$ -pulse with  $\Omega \gg t$  places each atom in an equal superposition of ground and excited electronic states. For  $a/\lambda_{\text{clk}} \bmod 1 \neq 0$ , this pulse also changes the system’s motional state. During field-free evolution ( $\Omega = 0$ ), the different motional states beat against each other causing a dephasing of the spectroscopic feature. We quantify this effect with the following relation,

$$\gamma = \sqrt{\langle H^2 \rangle - \langle H \rangle^2}. \quad (4.8)$$

The dephasing rates for a system consisting of 1 (single-particle) and two (half-filling) atoms are shown as a function of lattice spacing in Fig. 4.9b. The repulsion between atoms apparently localizes their motional states, leading to an enhanced suppression of tunneling. Such physics in the many-body limit is known as a Mott-insulator [68]

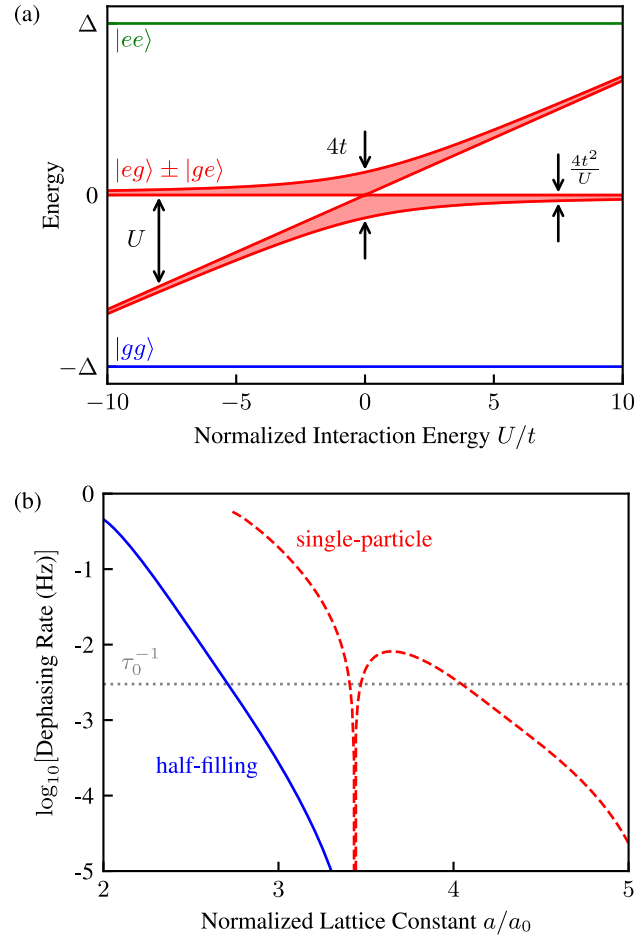


Figure 4.9: Two-atoms in a double-well potential. (a) Energy spectrum of Eqn. 4.7 at half-filling. States with zero, one, and two atoms in  $|e\rangle$  are shown as blue, red, and green lines, respectively. The  $|gg\rangle$  and  $|ee\rangle$  states are non-interacting due to the Pauli exclusion principle. The  $|eg\rangle \pm |ge\rangle$  states are spread by twice the Bloch band width at  $U = 0$ . Whereas in the Mott-insulating regime ( $U/t \gg 1$ ), an energy gap  $U$  opens up and a pair of weakly interacting states become spectroscopically resolvable. (b) Dephasing rates, as given by Eqn. 4.8, for one (red dashed line) and two (solid blue line) atoms in a double well potential. The tunneling rates and interaction strengths as a function of lattice spacing are taken from Fig. 4.5 and inserted into the double well Hamiltonian with  $\Omega/2\pi = 0.5$  Hz. The curves are not plotted for  $4t > \Omega$  where the analogy between the double well system and an infinite lattice breaks down as the discrete levels of the finite sized system become resolved.

## 4.4 Alternative methods of reducing Raman scattering

### 4.4.1 Blue-detuned lattice

It has been proposed [69] that operation in a blue-detuned magic wavelength lattice, e.g. the polarizability-crossing in Fig. 2.12 near  $\omega_b \approx c/390$  nm where both polarizabilities are negative, would be a possible method to reduce Raman scattering induced dephasing due to the atoms being trapped at the lattice intensity minima. We compute a trap-depth dependence of the clock state coherences to be

$$\begin{aligned} \frac{d}{dt} \hat{S}_{eg} &= \Gamma_{eg}^1(\omega_b) \frac{1}{2} \bar{V}_b^{1/2} + \Gamma_{eg}^0 \\ \Gamma_{eg}^1(\omega_b) &= 110(10) \times 10^{-4} \text{ s}^{-1} \end{aligned} \quad (4.9)$$

We can then compare the expected dephasing rates in blue versus red detuned lattices by picking  $V_i$  to achieve similar tunneling rates along all lattice axes. For  $V_{\text{tot.}} = 150E_r$  in the red-detuned case, one requires  $V_{\text{tot.}} \approx 185E_b$  in the blue-detuned case. This gives  $\Gamma_{eg} \approx 14$  s and  $\Gamma_{eg}^b \approx 13$  s and we thus conclude that simply operating in a blue-detuned lattice does not provide for a significant advantage over the red-detuned case, and will not enable atomic coherence times on the order of  $\tau_0$ .

### 4.4.2 Floquet Engineering

Here we briefly discuss a shaken lattice as an additional method for engineering lattices of localized atoms which does not necessarily involve increased lattice constants. Ignoring collisional interactions, we assign the following Hamiltonian,

$$H/\hbar = -t \sum_{\langle i,j \rangle} (c_i^\dagger c_j + c_j^\dagger c_i) + \omega K \cos \omega t \sum_i i n_i \quad (4.10)$$

Here  $K$  is the dimensionless driving amplitude and  $\omega$  the frequency of the drive. This can be shown to lead to an effective Hamiltonian

$$H_{\text{eff}}/\hbar = -t_{\text{eff}} \sum_{\langle i,j \rangle} (c_i^\dagger c_j + c_j^\dagger c_i) \quad (4.11)$$

with  $t_{\text{eff}} = t \mathcal{J}_0(K)$ . Thus one may localize atoms by operating at a zero crossing of the Bessel function. However small deviations  $\delta K$  in the modulation amplitude may contribute to significant dephasing.

$$\delta t_{\text{eff}} = \frac{\partial t_{\text{eff}}}{\partial K} \delta K = -t \mathcal{J}_1(K) \delta K \quad (4.12)$$

In a  $V = 4E_r$  lattice, one requires  $\delta t_{\text{eff}}/t \lesssim 5 \times 10^{-6}$  in order to sufficiently suppress tunneling, or equivalently  $\delta K/K \lesssim 4 \times 10^{-6}$  at the first zero,  $K \approx 2.4$ . That is, one needs to control some experimental parameter, such as the position of the lattice beam retro-reflector, at the part-per-million level.

#### 4.4.3 Accelerated lattice

In one-dimensional systems oriented along the acceleration of gravity [55, 70], coherent interrogations have been demonstrated in lattice depths as low as  $\bar{V}_c = 6$ . Such a technique alone is likely to be insufficient to suppress all dephasing mechanisms in a cubic lattice at the 1 mHz level since the gravitational force acting along each axis can be at most a factor of  $\sqrt{3}$  smaller, and lattice depths of  $\bar{V}_c > 3 \times 10$  are generally required to enter the Mott-insulating regime. None-the-less, extending the calculations presented in Ref. [71] might still be worthwhile.

## Chapter 5

### Resonant Dipole-Dipole Interactions

Up to this point, we have shown how careful preparation of a spin-polarized, degenerate Fermi-gas in a deep, simple-cubic, optical lattice enables the simultaneous interrogation of  $N \approx 10^4$  strontium atoms with interrogation times  $T \sim 10$  s. The evolution of the atomic state can largely be treated as that of independent dipole moments interacting with a classical environment. However, by operating with inter-particle spacings on the order of the clock transition's optical wavelength,  $ka \approx 7\pi/6$ , one must consider additional effects which have been largely unexplored in the context of atomic clocks.

The essence of following physics, generically referred to as *resonant dipole-dipole interactions* is that a finite, oscillating electric dipole moment creates an electric field with which other dipoles can interact with. The interactions lead to both an elastic frequency shift and a modified decay rate of the dipole moments, which we refer to as the *cooperative Lamb shift* and *cooperative decay*, respectively. The natural energy scale of resonant dipole-dipole interactions is set by the spontaneous decay rate of the interrogated transition,  $\Gamma_q \approx 2\pi \times 1.35$  mHz for the clock transition in strontium-87. Given that the total systematic uncertainty of optical atomic clocks operating with significantly lower densities have surpassed this fractional frequency scale  $\Gamma_q/\omega_0 \approx 3 \times 10^{-18}$ , a systematic characterization of these effects is crucial to the viability of three-dimensional optical-lattice clocks. Anticipating further progress, the obtained results will soon be relevant to other atomic clocks operating at lower-densities.

## 5.1 Theoretical background

Many key insights can be obtained classically although quantitative modeling of the observed response requires a full quantum treatment. Both limits are discussed in this section.

### 5.1.1 Classical Electric Field of Oscillating Point Dipole

Beginning with an electrically neutral medium, we write Maxwell's equations for the electric  $\mathbf{E}$  and magnetic  $\mathbf{B}$  fields, given a current source  $\mathbf{J}$ , as

$$\begin{aligned}\nabla \cdot \mathbf{E} &= 0 & \nabla \times \mathbf{B} - \frac{1}{c^2} \partial_t^2 \mathbf{E} &= \mu_0 \mathbf{J} \\ \nabla \cdot \mathbf{B} &= 0 & \nabla \times \mathbf{E} + \partial_t \mathbf{B} &= 0\end{aligned}\tag{5.1}$$

Taking a time derivative of the current density and rearranging yields the following wave equation for the electric field,

$$\left( \nabla \cdot \nabla - \frac{1}{c^2} \partial_t^2 \right) \mathbf{E} = \mu_0 \partial_t \mathbf{J} .\tag{5.2}$$

Assuming a harmonically oscillating current localized to a point at position  $\mathbf{a}$ ,  $\mathbf{J} = -i\omega \delta(\mathbf{r} - \mathbf{a}) \mathbf{d}_a \propto e^{-i\omega t}$ ,

$$(\nabla \cdot \nabla + k^2) \mathbf{E} = -\frac{k^2}{\epsilon_0} \delta(\mathbf{r} - \mathbf{a}) \mathbf{d}_a\tag{5.3}$$

which is solved by  $\mathbf{E}_a(\mathbf{b}) = \mathcal{G}(\mathbf{r}_{ba}) \cdot \mathbf{d}_a$  where  $\mathcal{G}$  is the so-called dyadic Green's function

$$\begin{aligned}\mathcal{G}(\mathbf{r}_{ba}) &= (k^2 + \nabla \cdot \nabla) \frac{e^{ikr_{ba}}}{4\pi\epsilon_0 r_{ba}} \\ &= \frac{k^3 e^{ikr_{ba}}}{4\pi\epsilon_0} \left\{ (1 - \hat{\mathbf{r}}_{ba} \hat{\mathbf{r}}_{ba}) \frac{1}{kr_{ba}} + (3\hat{\mathbf{r}}_{ba} \hat{\mathbf{r}}_{ba} - 1) \left[ \frac{1}{(kr_{ba})^3} - \frac{i}{(kr_{ba})^2} \right] \right\}\end{aligned}\tag{5.4}$$

with  $\mathbf{r}_{ba} = \mathbf{b} - \mathbf{a}$ ,  $r_{ba} = |\mathbf{r}_{ba}|$ , and  $\hat{\mathbf{r}}_{ba} = \mathbf{r}_{ba}/r_{ba}$ . This expression is exact for all values of  $kr$  in the limit  $k|\mathbf{R}_a| \ll 1$  where  $\mathbf{R}_a = \mathbf{d}_a/Q$  is the spatial displacement of  $\mathbf{d}_a$  after association with a point charge  $Q$ . Such an approximation is generically valid for electric dipole transitions in atoms; for the 1S-2P transition in atomic hydrogen,  $k|\mathbf{R}_a| \approx 2(2/3)^4 \alpha \approx 3 \times 10^{-3}$ .

In the radiation limit,  $kr_a \gg 1$ ,  $\mathbf{E}_a$  is a spherical wave with  $\mathbf{E}_a \cdot \hat{\mathbf{r}}_a = 0$  and a time-averaged intensity

$$I_a = \frac{\epsilon_0 c}{2} |\mathbf{E}_a|^2 = \frac{k^4 c |\mathbf{d}_a|^2}{32\pi^2 \epsilon_0 r_a^2} (1 - |\hat{\mathbf{e}} \cdot \hat{\mathbf{r}}_a|^2) .\tag{5.5}$$

where  $\hat{\mathbf{e}} = \mathbf{d}/|\mathbf{d}|$ . The far-field radiation patterns for linearly  $\hat{\mathbf{e}}_0 = \hat{\mathbf{z}}$ , and circularly  $\hat{\mathbf{e}}_{\pm 1} = (\hat{\mathbf{x}} \mp i\hat{\mathbf{y}})/\sqrt{2}$  polarized dipoles are shown in Fig. 5.5. Integrating over a spherical surface of radius  $\mathbf{r}_a$ , the dissipated power is

$$P_a = \int d\Omega r_a^2 I_a = \frac{k^4 c |\mathbf{d}_a|^2}{12\pi\epsilon_0} \quad (5.6)$$

### 5.1.2 Interactions Between Classical Oscillating Point Dipoles

For an arbitrary distribution of point dipoles  $\mathbf{d} = \sum_a \mathbf{d}_a$ , the interactions with the electric field  $\mathbf{E} = \sum_a \mathbf{E}_a$  are described by the Hamiltonian  $H_{\text{int}} = -\mathbf{d} \cdot \mathbf{E} = -\sum_{\mathbf{b}a} \mathbf{d}_a \cdot \mathbf{E}_b$ . We can additionally enforce the previously assumed harmonic motion of the individual dipoles by associating a mass  $M$  to the point charges and defining the Hamiltonian  $H_0 = \sum_{a,q} M\omega_{a,q}^2 |\hat{\mathbf{e}}_q \cdot \mathbf{d}_a|^2 / 2Q^2$  in the  $Q \rightarrow 0$  limit. Together, these yield the following Newtonian equations of motion

$$\partial_t^2 \mathbf{d}_a = -\sum_q \omega_{a,q}^2 \hat{\mathbf{e}}_q \hat{\mathbf{e}}_q \cdot \mathbf{d}_a + \frac{Q^2}{M} \sum_b \mathcal{G}(\mathbf{r}_{ba}) \cdot \mathbf{d}_b \quad (5.7)$$

Inserting the ansatz  $\mathbf{d}_a(t) = \sum_q \mathbf{d}_{a,q}$ , with  $\mathbf{d}_{a,q} = e^{-i(\omega_{a,q}t + \Omega_{a,q}t + \phi_{a,q})} |d_{a,q}| \hat{\mathbf{e}}_q$ , into Eq. 5.7 and solving for  $\Omega_{a,q} = \sum_{b,q'} V_{ba}^{qq'}$  yields the solution  $V_{ba}^{qq'} = -\mathbf{d}_{a,q'}^* \cdot \mathcal{G}(\mathbf{r}_{ba}) \cdot \mathbf{d}_{b,q} Q^2 / 2M\omega_{q'} |d_{a,q'}|^2$ <sup>1</sup>. That is, the real and imaginary parts of  $\Omega_{a,q}$  cause a frequency shift and damping of the initial excitation, respectively.

The self-interaction induced damping  $\text{Im}(V_{aa})$  equates the loss in kinetic energy of a single dipole  $\mathbf{d} = \mathbf{d}_a$  to the energy gained by the electromagnetic field in Eq. 5.6:  $-\partial_t K_a = P_a$  where  $K_{a,q} = M|\partial_t \mathbf{d}_{a,q}|^2 / 2Q^2$ . In order to remove explicit dependencies on the *ad hoc* parameters,  $Q$  and  $M$ , we take  $\Gamma_q = P_{a,q} / K_{a,q} = -2\text{Im}(V_{aa}^{qq})$  as defining the characteristic energy scale of  $V_{ba}$

$$V_{ba}^{qq'} = -\frac{3}{4} \Gamma_{q'} \left( \frac{\Gamma_q \omega_{b,q}}{\Gamma_{q'} \omega_{a,q'}} \right)^{1/2} e^{-i(\Delta\omega_{ba}t + \Delta\phi_{ba} - kr_{ba})} \times \left\{ [1 - (\hat{\mathbf{e}}_{q'}^* \cdot \hat{\mathbf{r}}_{ba})(\hat{\mathbf{r}}_{ba} \cdot \hat{\mathbf{e}}_q)] \frac{1}{kr_{ba}} + [3(\hat{\mathbf{e}}_{q'}^* \cdot \hat{\mathbf{r}}_{ba})(\hat{\mathbf{r}}_{ba} \cdot \hat{\mathbf{e}}_q) - 1] \left[ \frac{1}{(kr_{ba})^3} - \frac{i}{(kr_{ba})^2} \right] \right\}, \quad (5.8)$$

where  $\Delta\omega_{ba} = \omega_{b,q} - \omega_{a,q'}$  and  $\Delta\phi_{ba} = \phi_{b,q} - \phi_{a,q'}$ . The resonant dipole-dipole interaction coefficients  $V_{ba}$  are plotted in Fig. 5.1. The regions in parameter space where  $\text{Im}(V_{ba}) \neq 0$  correspond to the classical analog of cooperative decay, where the radiated fields of two dipoles add constructively (*superradiance*),

<sup>1</sup> Here, the prior assumption  $k|\mathbf{R}_a| \ll 1$  validates our expansion under  $\Omega_{a,q} \ll \omega_q$

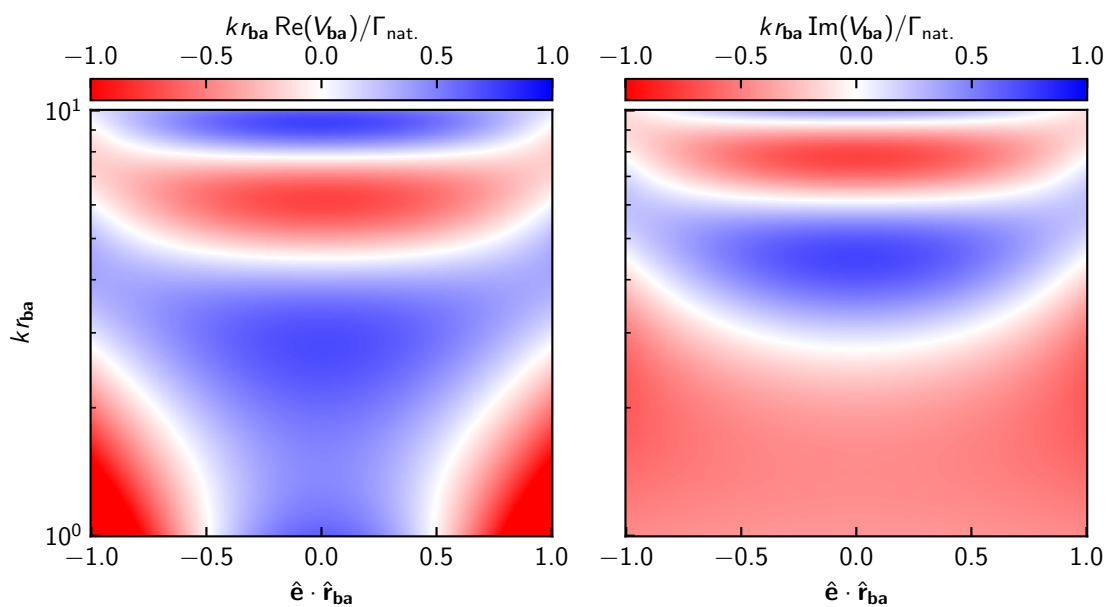


Figure 5.1: The real and imaginary parts of the interaction parameters  $V_{ba}$  for  $\phi_b = \phi_a$  are shown on the left and right, respectively. For arbitrary differences in the instantaneous phases  $\Delta\phi_{ba} = \phi_b - \phi_a$ , the two plots are rotated into one-another according to  $V_{ba} \rightarrow V_{ba}e^{-i\Delta\phi_{ba}}$

or destructively (*subradiance*), resulting in an increase, or decrease in the radiated power  $|\mathbf{E}_a + \mathbf{E}_b|^2 \neq |\mathbf{E}_a|^2 + |\mathbf{E}_b|^2$ , accordingly. Similarly,  $\text{Re}(V_{ba}) \neq 0$  can be interpreted as the classical analogue of the *cooperative Lamb shift*.

### 5.1.3 Interactions Between quantum Dipoles

As we shall see, much of the previously described behavior can analogously be described in the quantum mechanical picture where the degrees of freedom are replaced by operators. For the electric field, we have

$$\hat{\mathbf{E}} = - \sum_{\mathbf{k}, \epsilon} \mathbf{E}_{\mathbf{k}, \epsilon} \hat{a}_{\mathbf{k}, \epsilon} e^{i\mathbf{k} \cdot \mathbf{r}} + \text{H.c.} \quad (5.9)$$

where  $\hat{a}_{\mathbf{k}, \epsilon}^\dagger$  is the creation operators for a photon with wave-vector  $\mathbf{k}$  and polarization  $\hat{\mathbf{e}}_\epsilon$ , and  $\mathbf{E}_{\mathbf{k}, \epsilon} = \hat{\mathbf{e}}_\epsilon (\hbar \omega_{\mathbf{k}, \epsilon} / 2\epsilon_0 \mathcal{V})^{1/2}$ , for some quantization volume  $\mathcal{V}$ . The dipoles are similarly replaced by

$$\hat{\mathbf{d}} = \sum_{\mathbf{a}, q} \mathbf{d}_q \hat{S}_{\mathbf{a}, q} e^{i\mathbf{k} \cdot \mathbf{a}} + \text{H.c.} \quad (5.10)$$

where  $\hat{S}_{\mathbf{a}, q}^\dagger = e^{i\mathbf{k} \cdot \mathbf{a}} |e_q\rangle \langle g_q|$  is the spin- $\frac{1}{2}$  raising operator for the transition labeled  $q$ , and  $\mathbf{d}_q = \hat{\mathbf{e}}_q (3\pi\epsilon_0 \hbar \Gamma_q / k^3)^{1/2}$ . The Hamiltonian of the uncoupled system can be given as

$$\hat{H}_0 = \sum_{\mathbf{k}, \epsilon} \hbar \omega_{\mathbf{k}, \epsilon} \left( \hat{a}_{\mathbf{k}, \epsilon}^\dagger \hat{a}_{\mathbf{k}, \epsilon} + \frac{1}{2} \right) + \sum_{\mathbf{a}, q} \hbar \omega_{\mathbf{a}, q} \hat{S}_{\mathbf{a}, q}^\dagger \hat{S}_{\mathbf{a}, q} \quad (5.11)$$

In the frame rotating with  $\hat{H}_0$ , the interactions of the individual dipoles with the electromagnetic field is given as

$$\begin{aligned} \hat{H}_{\text{int}} &= -e^{i\hat{H}_0 t} \hat{\mathbf{d}} \cdot \hat{\mathbf{E}} e^{-i\hat{H}_0 t} \\ &= \sum_{\mathbf{k}, \epsilon} \sum_{\mathbf{a}, q} \left( \mathbf{d}_{\mathbf{a}, q} \hat{S}_{\mathbf{a}, q} e^{-i(\omega_{\mathbf{a}, q} t - \mathbf{k} \cdot \mathbf{a})} + \text{H.c.} \right) \cdot \left( \mathbf{E}_{\mathbf{k}, \epsilon} \hat{a}_{\mathbf{k}, \epsilon} e^{-i(\omega_{\mathbf{k}, \epsilon} t - \mathbf{k} \cdot \mathbf{a})} + \text{H.c.} \right) \end{aligned} \quad (5.12)$$

Proceeding similarly to the prior chapter on Raman scattering of optical lattice photons, the photonic degrees of freedom can be “integrated out”, although this time, the dipole operator  $\mathbf{d}$  contains a sum over multiple particles, leading to effective dipole-dipole interactions. Additionally, we make the rotating wave approximation, dropping terms proportional to  $e^{\mp i(\omega_{\mathbf{a}, q} + \omega_{\mathbf{k}, \epsilon})t}$ , resulting in the following

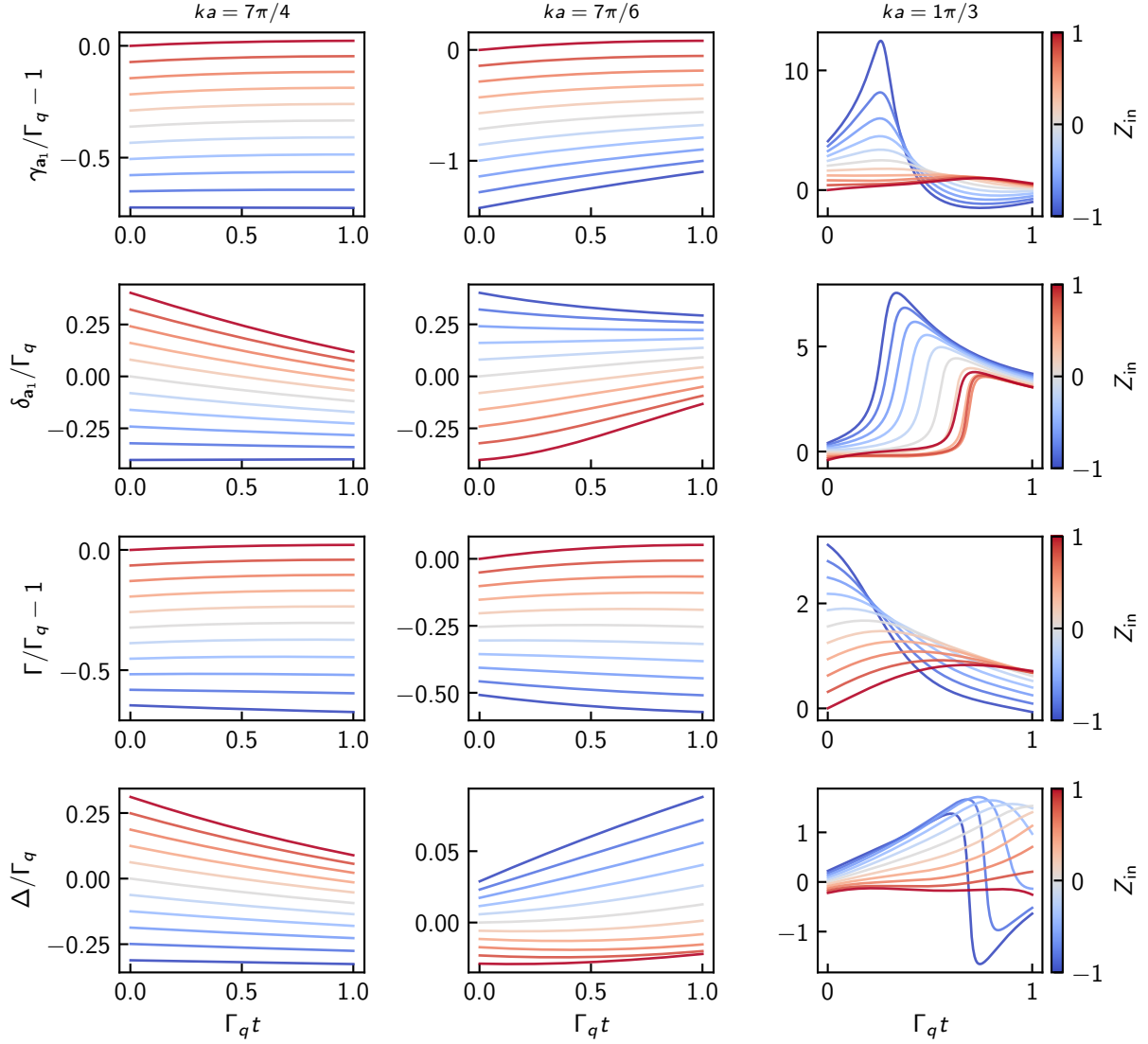


Figure 5.2: Full-state time-evolution for nearest-neighbor, spin- $\frac{1}{2}$ , resonant dipole-dipole interactions in a cubic lattice. The density matrix  $\hat{\rho}$  is time-evolved according to Eq. 5.13 for 7 dipoles,  $\mathbf{a} \in \{\mathbf{a}_1, \dots, \mathbf{a}_7\}$  oriented on a simple-cubic lattice with  $\mathbf{a} = a(x_a\hat{\mathbf{x}} + y_a\hat{\mathbf{y}} + z_a\hat{\mathbf{z}})$ . Denoting the central dipole  $\mathbf{a}_1$ , the other dipoles are placed on each of the six “nearest-neighbor” sites satisfying  $r_{\mathbf{b}\mathbf{a}} = a$ . Columns are labeled by the parameter  $ka$ . All plots fix  $\hat{\mathbf{e}}_q = \hat{\mathbf{e}}_{q'} = \hat{\mathbf{z}}$ ,  $\omega_a = \omega$ , and  $\phi_a = ka\chi_a$ . Colors encode the initial product-state with  $Z_{\text{in}} = \langle \hat{S}_a^\dagger \hat{S}_a \hat{\rho}(0) \rangle = (1 - \text{Re}(\langle \hat{S}_a^\dagger \hat{\rho}(0) \rangle))^2)^{1/2}$ . The single-dipole decay rates and frequency shifts are computed as  $\gamma_a(t) = -\log \text{tr}[\hat{S}_a^\dagger \hat{S}_a \hat{\rho}(t)] / \text{tr}[\hat{S}_a^\dagger \hat{S}_a \hat{\rho}(0)] / t$ , and  $\delta_{a_1}(t) = \arg \text{tr}[\hat{S}_{a_1} \hat{\rho}(t)] / t$ . The average decay rates and frequency shifts are then  $\Gamma = \sum_a \gamma_a$  and  $\Delta = \sum_a \delta_a$ .

quantum master equation in Lindblad form

$$\begin{aligned}\partial_t \hat{\rho} &= \mathcal{L}_{dd}[\hat{\rho}] \\ &= -i \sum_{\mathbf{b}, \mathbf{a}, q, q'} V_{\mathbf{ba}}^{qq'} \left( \hat{S}_{\mathbf{b}, q}^\dagger \hat{S}_{\mathbf{a}, q'} \hat{\rho} - \hat{S}_{\mathbf{a}, q'} \hat{\rho} \hat{S}_{\mathbf{b}, q}^\dagger \right) + \text{H.c.}\end{aligned}\quad (5.13)$$

where we have recovered the interaction parameter  $V_{\mathbf{ba}}^{qq'}$  in Eq. 5.8 . For a spin- $\frac{1}{2}$  system,  $q, q' \in \{0\}$ , Eq. 5.13 can be solved exactly for small numbers of particles. The results of such a simulation, for nearest-neighbor interactions in a simple-cubic lattice, are summarized in Fig. 5.2.

At this point we would like to note that this is essentially the same derivation as what produced spontaneous emission and the Lamb shift in Ch. 2, however this time, we included the presence of multiple atoms and found additional contributions. These realizations were first pointed out by Refs. [72–74], and have since been frequently referred to as cooperative decay, and cooperative Lamb shifts, respectively. Effects of cooperative decay are ubiquitous in experimental physics [75–86], while cooperative Lamb shifts have also been observed in a wide variety of systems, overall reports are less frequent [87–92] and dynamics of the coherent interaction have thus far remained elusive. More recently, cooperative electro-magnetic interactions have been considered in the context of ordered arrays of atoms, resulting in a number of novel theoretical predictions [93–99], followed by the recent experimental demonstration that a monolayer of atoms on a square lattice can act as an efficient mirror [100].

As was first suggested in Ref. [93], given the natural linewidth of the strontium-87 clock transition, and thus the natural scale of cooperative Lamb shifts, happens to be roughly equal to the size of clock shifts modern atomic clocks care about, it seems reasonable to attempt to measure these shifts and demonstrate an ability to characterize their magnitude. Since the atomic coherence times in the cubic lattice are limited to  $\mathcal{O}(10 \text{ s}) \ll \mathcal{O}(\Gamma^{-1})$ , we may Taylor expand the solution to Eq. 5.13, keeping terms at most linear in the parameter  $\Gamma_q t$ .

#### 5.1.4 First-order time-expansion of resonant dipole-dipole dynamics

For increasing numbers of dipoles  $N$ , and internal levels  $\mathcal{N}$ , the Hilbert space grows exponentially as  $\dim \hat{\rho} = \mathcal{N}^N$ , making general numerical solutions to Eq. 5.13 increasingly difficult. In the limit  $\Gamma_q t \ll 1$ ,

one can approximate  $\frac{d}{dt}\langle\hat{O}_a\hat{O}_b\rangle = \text{tr}\{\hat{O}_a\hat{O}_b\mathcal{L}_{dd}[\hat{\rho}]\} \approx 0$ . In the effective subspace  $\hat{\rho}_{a,q} = \text{tr}_{\underline{a},q}\hat{\rho}$ , the number of degrees of freedom are dramatically reduced,  $\sum_a\sum_q\dim\hat{\rho}_{a,q} = NN(\mathcal{N}-1)$ , enabling numerical solutions for experimentally relevant system sizes and arbitrary geometries. Explicitly, we write,

$$\begin{aligned}\partial_t\langle\hat{S}_{a,q}^\dagger\rangle &= \partial_t\langle\hat{S}_{a,q'}\rangle^* \\ &= \text{Tr}\left(\hat{S}_{a,q'}^\dagger\mathcal{L}_{dd}[\hat{\rho}]\right) = i\sum_{b,q}V_{ba}^{qq'}\left(\langle\hat{S}_{a,q'}^\dagger\hat{S}_{a,q'}\hat{S}_{b,q}^\dagger\rangle - \langle\hat{S}_{a,q'}\hat{S}_{a,q'}^\dagger\hat{S}_{b,q}^\dagger\rangle\right)\end{aligned}\quad (5.14)$$

$$\begin{aligned}\partial_t\langle\hat{S}_{a,q'}^\dagger\hat{S}_{a,q'}\rangle &= -\partial_t\langle\hat{S}_{a,q'}\hat{S}_{a,q'}^\dagger\rangle \\ &= \text{Tr}\left(\hat{S}_{a,q'}^\dagger\hat{S}_{a,q'}\mathcal{L}_{dd}[\hat{\rho}]\right) = i\sum_{b,q}V_{ba}^{qq'}\left(\langle\hat{S}_{a,q'}^\dagger\hat{S}_{a,q'}\hat{S}_{b,q}^\dagger\rangle - \langle\hat{S}_{a,q'}\hat{S}_{a,q'}^\dagger\hat{S}_{b,q}^\dagger\rangle\right)\end{aligned}$$

with solutions,

$$\begin{aligned}\langle\hat{S}_{a,q'}^\dagger\mathcal{F}(t)\rangle &= \langle\hat{S}_{a,q'}^\dagger\rangle + it\sum_{b,q}V_{ba}^{qq'}\left[\langle\hat{S}_{a,q'}^\dagger\hat{S}_{a,q'}\hat{S}_{b,q}^\dagger\rangle - \langle\hat{S}_{a,q'}\hat{S}_{a,q'}^\dagger\hat{S}_{b,q}^\dagger\rangle\right] \\ \langle\hat{S}_{a,q'}^\dagger\hat{S}_{a,q'}\mathcal{F}(t)\rangle &= \langle\hat{S}_{a,q'}^\dagger\hat{S}_{a,q'}\rangle + it\sum_{b,q}V_{ba}^{qq'}\left[\langle\hat{S}_{a,q'}^\dagger\hat{S}_{a,q'}\hat{S}_{b,q}^\dagger\rangle - \langle\hat{S}_{a,q'}\hat{S}_{a,q'}^\dagger\hat{S}_{b,q}^\dagger\rangle\right]\end{aligned}\quad (5.15)$$

where we have introduced  $\mathcal{F}(t) = e^{\mathcal{L}_{dd}t}$ .

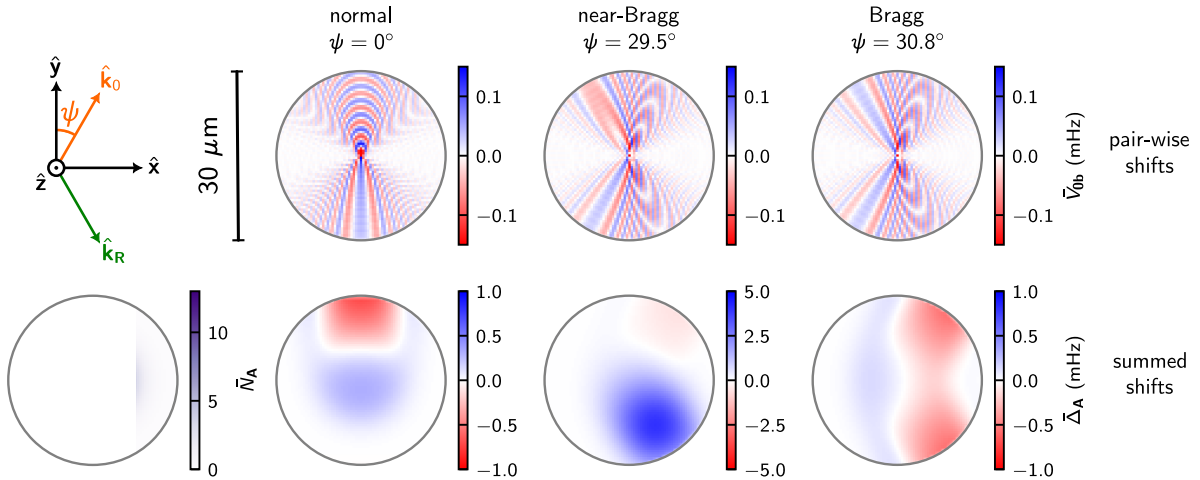


Figure 5.3: Modeling spatial signal of cooperative Lamb shifts. The top row shows the column-integrated pairwise interactions  $\text{Re}(\bar{V}_{ab})$  between an atom in the central pixel  $\mathbf{a} = \mathbf{0}$  and all other atoms projected onto pixel  $\mathbf{b}$ . The bottom row then shows the sums of interactions  $\bar{\Delta}$  given the density distribution  $\tilde{N}$  in the lower left. Dipole moments are oriented along the  $\hat{x}$ -axis.

The expected frequency shifts given by Eq. 5.15 are visualized in Fig. 5.3 for a cubic lattice and variable angles of incidence of the probe laser.

### 5.1.5 Resonant dipole-dipole interactions in a Ramsey interferometer

We now discuss how resonant dipole-dipole interactions affect a Ramsey signal to leading order in  $\Gamma t$ . Defining the rotation operator corresponding to a short resonant pulse of duration  $T = \theta/g$ ,

$$\begin{aligned}
\langle \hat{S}_a^\dagger \mathcal{R}(\theta, \phi) \rangle &= \cos^2(\theta/2) \langle \hat{S}_a^\dagger \rangle + e^{2i\phi} \sin^2(\theta/2) \langle \hat{S}_a \rangle - \frac{i}{2} e^{i\phi} \sin(\theta) \left( \langle \hat{S}_a^\dagger \hat{S}_a \rangle - \langle \hat{S}_a \hat{S}_a^\dagger \rangle \right) \\
\langle \hat{S}_a^\dagger \hat{S}_a \mathcal{R}(\theta, \phi) \rangle &= \cos^2(\theta/2) \langle \hat{S}_a^\dagger \hat{S}_a \rangle + \sin^2(\theta/2) \langle \hat{S}_a \hat{S}_a^\dagger \rangle - \frac{i}{2} \sin(\theta) \left( e^{-i\phi} \langle \hat{S}_a^\dagger \rangle - e^{i\phi} \langle \hat{S}_a \rangle \right) \\
\langle \hat{S}_a \hat{S}_a^\dagger \mathcal{R}(\theta, \phi) \rangle &= \cos^2(\theta/2) \langle \hat{S}_a \hat{S}_a^\dagger \rangle + \sin^2(\theta/2) \langle \hat{S}_a^\dagger \hat{S}_a \rangle + \frac{i}{2} \sin(\theta) \left( e^{-i\phi} \langle \hat{S}_a^\dagger \rangle - e^{i\phi} \langle \hat{S}_a \rangle \right).
\end{aligned} \tag{5.16}$$

For generic multi-dipole operators,

$$\partial_t \langle \prod_a \hat{O}_a \rangle = \sum_a g_a \langle \hat{P}_a \prod_{b \neq a} \hat{O}_b \rangle \tag{5.17}$$

Thus multi-particle matrix elements of  $\mathcal{R}$  can be obtained directly from the above elements, e.g.  $\partial \langle \hat{O}_a \hat{O}_b \mathcal{R}(\theta, \phi) \rangle / \partial \langle \hat{P}_a \hat{P}_b \rangle = \partial^2 \langle \hat{O}_a \mathcal{R}(\theta, \phi) \rangle \langle \hat{O}_b \mathcal{R}(\theta, \phi) \rangle / \partial \langle \hat{P}_a \rangle \partial \langle \hat{P}_b \rangle$ . In particular, we will make use of

$$\begin{aligned}
\langle \hat{S}_a^\dagger \mathcal{R}(\theta, 0) \rangle_0 &= -\frac{i}{2} \sin(\theta) n_a \\
\langle \hat{S}_a^\dagger \hat{S}_a \hat{S}_b^\dagger \mathcal{R}(\theta, 0) \rangle_0 &= -\frac{i}{2} \sin(\theta) \cos^2(\theta/2) n_a n_b \quad \text{for } \mathbf{a} \neq \mathbf{b} \\
\langle \hat{S}_a \hat{S}_a^\dagger \hat{S}_b^\dagger \mathcal{R}(\theta, 0) \rangle_0 &= -\frac{i}{2} \sin(\theta) \sin^2(\theta/2) n_a n_b \quad \text{for } \mathbf{a} \neq \mathbf{b} \\
\langle \hat{S}_a^\dagger \mathcal{R}(\pi, \phi) \rangle &= e^{2i\phi} \langle \hat{S}_a \rangle \\
\langle \hat{S}_a^\dagger \hat{S}_a \hat{S}_b^\dagger \mathcal{R}(\pi, \phi) \rangle &= e^{2i\phi} \langle \hat{S}_a \hat{S}_a^\dagger \hat{S}_b \rangle \quad \text{for } \mathbf{a} \neq \mathbf{b} \\
\langle \hat{S}_a \hat{S}_a^\dagger \hat{S}_b^\dagger \mathcal{R}(\pi, \phi) \rangle &= e^{2i\phi} \langle \hat{S}_a^\dagger \hat{S}_a \hat{S}_b \rangle \quad \text{for } \mathbf{a} \neq \mathbf{b} \\
\langle \hat{Z}_a \mathcal{R}(\pi/2, \phi) \rangle &= -i \left[ e^{-i\phi} \langle \hat{S}_a^\dagger \rangle - e^{i\phi} \langle \hat{S}_a \rangle \right].
\end{aligned} \tag{5.18}$$

During a single free-evolution-period, single-particle atomic coherences evolve according to

$$\partial_t \langle \hat{S}_a^\dagger \rangle = \text{Tr} \left( \hat{S}_a^\dagger \mathcal{L}_{\text{free}}[\hat{\rho}] \right) = i \sum_i \sum_b h_{ba}^{(i)} \left( \langle \hat{S}_a^\dagger \hat{S}_a \hat{S}_b^\dagger \rangle - \langle \hat{S}_a \hat{S}_a^\dagger \hat{S}_b \rangle \right) \tag{5.19}$$

where

$$\begin{aligned}
h_{ba}^{(1)} &= (\Delta\omega_a - i\gamma/2) \delta_{a,b} \\
h_{ba}^{(2)} &= V_{ba}
\end{aligned} \tag{5.20}$$

In solving  $\langle \hat{S}_a^\dagger \rangle$  to first order in  $\Gamma_0 t$ , we may obtain a closed form for the time-dependence of the multi-atom expectation values  $\langle \hat{S}_a^\dagger \hat{S}_a \hat{S}_b^\dagger \rangle$  and  $\langle \hat{S}_a \hat{S}_a^\dagger \hat{S}_b^\dagger \rangle$  for  $\mathbf{a} \neq \mathbf{b}$

$$\begin{aligned} \partial_t \langle \hat{S}_a^\dagger \hat{S}_a \hat{S}_b^\dagger \rangle &\approx \text{Tr} \left( \hat{S}_a^\dagger \hat{S}_a \hat{S}_b^\dagger \mathcal{L}_1[\hat{\rho}] \right) = \left( i\Delta\omega_b - \frac{3}{2}\gamma \right) \langle \hat{S}_a^\dagger \hat{S}_a \hat{S}_b^\dagger \rangle \\ \partial_t \langle \hat{S}_a \hat{S}_a^\dagger \hat{S}_b^\dagger \rangle &\approx \text{Tr} \left( \hat{S}_a \hat{S}_a^\dagger \hat{S}_b^\dagger \mathcal{L}_1[\hat{\rho}] \right) = \left( i\Delta\omega_b - \frac{1}{2}\gamma \right) \langle \hat{S}_a \hat{S}_a^\dagger \hat{S}_b^\dagger \rangle + \gamma \langle \hat{S}_a^\dagger \hat{S}_a \hat{S}_b^\dagger \rangle . \end{aligned} \quad (5.21)$$

We then have

$$\begin{aligned} \langle \hat{S}_a^\dagger \mathcal{F}(t) \rangle &= e^{-\gamma t/2} \left\{ e^{i\Delta\omega_a t} \left( 1 - \frac{\Gamma_0 t}{2} \right) \langle \hat{S}_a^\dagger \rangle + it \sum_{\mathbf{b} \neq \mathbf{a}} h_{\mathbf{b}\mathbf{a}}^{(2)} e^{i\Delta\omega_b t} \left[ (2e^{-\gamma t} - 1) \langle \hat{S}_a^\dagger \hat{S}_a \hat{S}_b^\dagger \rangle - \langle \hat{S}_a \hat{S}_a^\dagger \hat{S}_b^\dagger \rangle \right] \right\} \\ \langle \hat{S}_a^\dagger \hat{S}_a \hat{S}_b^\dagger \mathcal{F}(t) \rangle &= e^{-3\gamma t/2 + i\Delta\omega_b t} \langle \hat{S}_a^\dagger \hat{S}_a \hat{S}_b^\dagger \rangle \\ \langle \hat{S}_a \hat{S}_a^\dagger \hat{S}_b^\dagger \mathcal{F}(t) \rangle &= e^{-\gamma t/2 + i\Delta\omega_b t} \left[ (1 - e^{-\gamma t}) \langle \hat{S}_a^\dagger \hat{S}_a \hat{S}_b^\dagger \rangle + \langle \hat{S}_a \hat{S}_a^\dagger \hat{S}_b^\dagger \rangle \right] . \end{aligned} \quad (5.22)$$

We now consider a “spin-echo” sequence which is designed to remove effects of the single-particle coherent dephasing from  $\Delta\omega_a$

$$\mathcal{U} = \mathcal{R}(\pi/2, \phi_{\text{out}}) \mathcal{F}(T/4) \mathcal{R}(\pi, \pi) \mathcal{F}(T/2) \mathcal{R}(\pi, -\pi/2) \mathcal{F}(T/4) \mathcal{R}(\theta_{\text{in}}, 0) \quad (5.23)$$

whereby, matrix multiplication, dropping terms  $\mathcal{O}(\Gamma_0^2 T^2)$ , gives

$$\langle \hat{Z}_a \mathcal{U} \rangle_0 = n_a \sin(\theta_{\text{in}}) e^{-\gamma T/2} [\sin(\phi_{\text{out}} + \Phi) J_a + \cos(\phi_{\text{out}} + \Phi) (1 - K_a)] \quad (5.24)$$

with

$$\begin{aligned}
J_a &= \sum_{\mathbf{b} \neq \mathbf{a}} n_{\mathbf{b}} \operatorname{Re}(V_{\mathbf{ba}} F_{\mathbf{ba}}^+) \\
&= \cos(\theta_{\text{in}}) T \sum_{\mathbf{b} \neq \mathbf{a}} n_{\mathbf{b}} \operatorname{Re}(V_{\mathbf{ba}}) + \mathcal{O}(\Gamma_0 \gamma T^2, \Gamma_0 \Delta \omega T^2) \\
K_a &= \frac{\Gamma_0 T}{2} + \sum_{\mathbf{b} \neq \mathbf{a}} n_{\mathbf{b}} \operatorname{Im}(V_{\mathbf{ba}} F_{\mathbf{ba}}^-) \\
&= \frac{\Gamma_0 T}{2} + \mathcal{O}(\Gamma_0 \gamma T^2, \Gamma_0 \Delta \omega T^2) \\
F_{\mathbf{ba}}^\pm &= \frac{T}{4} \left( e^{-\gamma T} \cos \theta_{\text{in}} - \left(1 - e^{-\gamma T/4}\right)^3 \left(1 + e^{-\gamma T/4}\right) \right. \\
&\quad \left. + \left\{ e^{-\gamma T/4} (1 + \cos \theta) - 1 \pm 2 \left[ e^{-3\gamma T/4} (1 + \cos \theta) - 2e^{-\gamma T/2} + 1 \right] \right\} e^{i(\Delta \omega_{\mathbf{b}} - \Delta \omega_{\mathbf{a}}) T/4} \right) \\
&= \frac{T}{4} \left\{ e^{-\gamma T} (1 + \cos \theta) - 2e^{-3\gamma T/4} + e^{-\gamma T/4} (3 + \cos \theta) - 2 \right. \\
&\quad \left. \pm 2 \left[ e^{-3\gamma T/4} (1 + \cos \theta) - 2e^{-\gamma T/2} + 1 \right] + \mathcal{O}(\Delta \omega T) \right\} \\
\Phi &= \Delta \phi(T) - 2\Delta \phi(3T/4) + 2\Delta \phi(T/4) - \Delta \phi(0)
\end{aligned} \tag{5.25}$$

and where  $\Delta \phi(t)$  is the instantaneous laser phase noise at time  $t$ . Averaging over shot-to-shot fluctuations in  $\Phi$ , which are normally distributed, for  $\cos \phi_{\text{out}} = 0$ , the mean  $\bar{D}_{\mathbf{A}}$  and standard deviation  $\Delta \bar{D}_{\mathbf{A}}$  of  $\sum_{\mathbf{a} \parallel \mathbf{A}} \langle \hat{Z}_{\mathbf{a}} \mathcal{U} \rangle_0 / C$  are

$$\begin{aligned}
\bar{D}_{\mathbf{A}} &= e^{-\langle \Phi^2 \rangle / 2} \sum_{\mathbf{a} \parallel \mathbf{A}} n_{\mathbf{a}} J_{\mathbf{a}} \\
&= \sum_{\mathbf{a} \parallel \mathbf{A}} n_{\mathbf{a}} J_{\mathbf{a}} + \mathcal{O}(\langle \Phi^2 \rangle) \\
\Delta \bar{D}_{\mathbf{A}} &= e^{-\langle \Phi^2 \rangle / 2} \sum_{\mathbf{a} \parallel \mathbf{A}} n_{\mathbf{a}} \sqrt{[\cosh(\langle \Phi^2 \rangle) - 1] J_{\mathbf{a}}^2 + \sinh(\langle \Phi^2 \rangle) (1 - K_{\mathbf{a}})^2} \\
&= \sqrt{\langle \Phi^2 \rangle} \sum_{\mathbf{a} \parallel \mathbf{A}} n_{\mathbf{a}} (1 - K_{\mathbf{a}}) + \mathcal{O}(\langle \Phi^2 \rangle).
\end{aligned} \tag{5.26}$$

In modeling the experimental results in the following section we use the full time dependencies in Eq. 5.26 with  $\sqrt{\langle \Phi^2 \rangle} = \sqrt{3 \langle \Delta \phi^2(T) \rangle / 8} \approx 110$  mrad., and  $\Delta \omega_{\mathbf{a}} = \Delta \omega_{\mathbf{b}} = 0$ . The noise-induced suppression of the mean difference signal  $\bar{D}_{\mathbf{a}}$ ,  $1 - e^{-\langle \Phi^2 \rangle / 2} \approx 6 \times 10^{-3}$ , is insignificant with respect to the measurement precision of the presented data.

### 5.1.6 Bragg enhancement of cooperative Lamb shifts

While  $V_{ba}$  asymptotically decays with increasing separation as  $1/kr_{ba}$ , the contained phase-factors  $e^{-i(kr_{ba} + \mathbf{k}_0 \cdot \mathbf{r}_{ba})}$  average to zero for incommensurate  $ka_{lat} \approx 7\pi/6$  and  $\psi = 0^\circ$ , resulting in effectively nearest neighbor interactions scaling with the local filling fractions, *i.e.*  $J_a \propto n_a$ . However, the sub-wavelength lattice spacing  $ka_{lat} < 2\pi$  guarantees the unique existence of the Bragg resonance at  $\psi = \arccos(\pi/ka_{lat}) \approx 30.8^\circ$  satisfying  $\mathbf{k}_0 \cdot a\hat{\mathbf{y}} = \pi$  such that the radiated fields add constructively along  $\mathbf{k}_R = \mathbf{k}_0 - 2(\mathbf{k}_0 \cdot \hat{\mathbf{y}})\hat{\mathbf{y}}$ . Numerically, we find that the ensemble-averaged interaction strengths are maximized, and scale with the system size as  $N_{tot}^{1/3}$ , at angular detunings from exact Bragg resonance set by the diffraction limit  $\pi/2k(w_x^2 + w_y^2)^{1/2} \approx 1.9^\circ$  [93, 101]. The shift's scaling with system size is shown in Fig. 5.4 and the shift's sensitivity to changes in the initial tipping angle  $\langle \Delta\tilde{\delta}/\Delta \cos\theta_{in} \rangle$ , averaged over all observed  $\theta_{in}$ , is plotted against  $\psi$  in Fig. 5.7.

## 5.2 Measurement of cooperative Lamb shifts

Inspecting Eq. 5.24 and as depicted in Fig. 5.5, we have at least three experimental knobs which we can vary in order to characterize the validity of our model. First, the probed transition  $q$  effects both the overall coupling strength via a Clebsch-Gordan coefficient, and the far-field radiation pattern by conservation of angular momentum. Second, the angle of incidence  $\psi$  effects the relative drive phases of the atomic dipoles and thus the spatial profile and overall magnitude of the cooperative Lamb shifts. And third, the initial tipping angle  $\theta_{in}$  simply rescales the shifts by a factor  $\cos(\theta_{in})$ .

### 5.2.1 Analysis of results

Over a period of two weeks, approximately 100 hours of data were collected while cyclically varying  $\theta_{in}$ ,  $\psi$ , and  $q$ . Given the recorded images of the final ground  $\tilde{N}_A^g$  and excited  $\tilde{N}_A^e$  state populations, we compute the sum  $\tilde{N}_A = \tilde{N}_A^e + \tilde{N}_A^g$  and difference  $\tilde{D}_A = (\tilde{N}_A^e - \tilde{N}_A^g)/\mathcal{C}$  signals where  $\mathcal{C}$  is the independently measured phase sensitivity of the difference signal. Fig. 5.6 shows the subset of acquired data associated with the control parameters which maximize the signal-to-noise ratio of the cooperative Lamb shift signal:

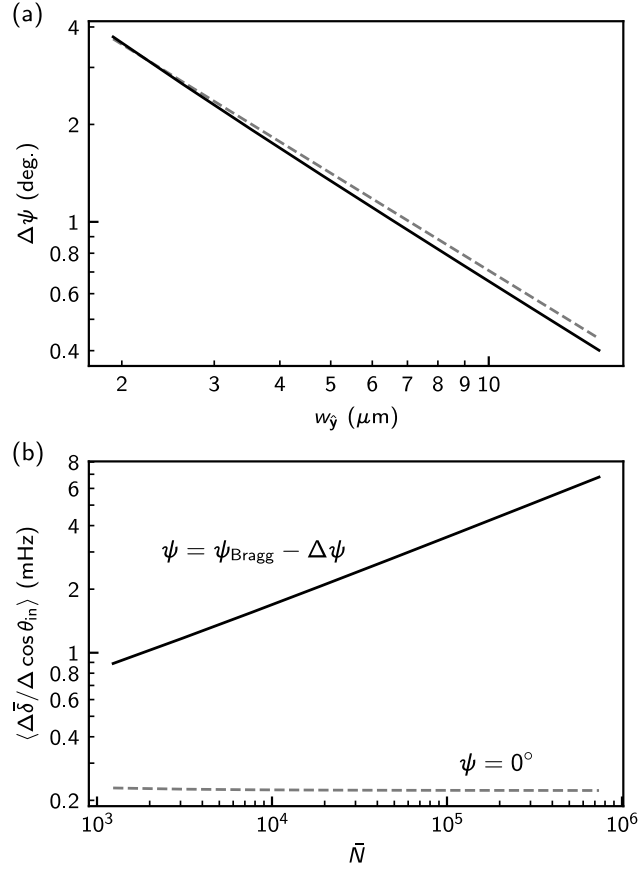


Figure 5.4: Scaling of cloud-averaged cooperative Lamb shift with system size. (a) Angular detuning  $\Delta\psi = \psi_{\text{Bragg}} - \psi$  from the Bragg resonance at  $\psi_{\text{Bragg}} \approx 30.8^\circ$  at which the ensemble-averaged cooperative lamb shift is maximized. Values obtained via numerical optimization after global rescaling of the cloud widths  $w_{\hat{n}}$  with fixed  $\mu_0 = 1.44$  are shown as the solid black line. The diffraction limit  $\Delta\psi \approx \pi/2k(w_x + w_y)^{-1/2}$  is shown as the grey dashed line. (b) Scaling of ensemble-averaged cooperative Lamb shift sensitivity  $\langle \Delta\bar{\delta}/\Delta \cos\theta_{in} \rangle$  versus summed counts  $\bar{N}$  for  $\psi = \psi_{\text{Bragg}} - \Delta\psi$  (solid black line) and  $\psi = 0^\circ$  (grey dashed line).

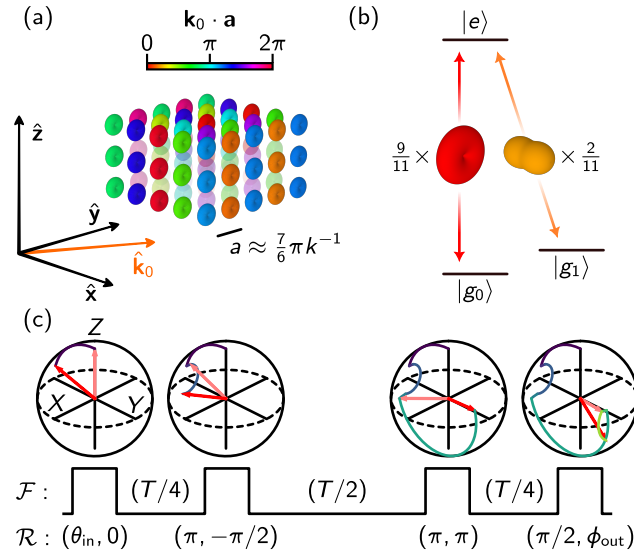


Figure 5.5: Experimental parameters for measuring cooperative Lamb shifts. (a) Atomic dipoles on a cubic lattice, indexed by their positions  $\mathbf{a}$ , are excited with a spatially dependent phases  $\mathbf{k}_0 \cdot \mathbf{a}$ . Proximity to the Bragg condition  $\mathbf{k}_0 \cdot a\hat{\mathbf{y}} = \pi$  leads to long-range phase ordering along the  $\hat{\mathbf{y}}$ -axis. (b) Far-field single-atom radiation patterns  $I^q(\hat{\mathbf{r}}_{ba})$  for the two spectroscopically resolved  $|e\rangle \leftrightarrow |g_q\rangle$  transitions used in this work, as defined in the main text. (c) Resonant laser pulses  $\mathcal{R}(\theta, \phi)$  rotate the atomic states by an angle  $\theta$  about the  $(X_a \cos \phi + Y_a \sin \phi)$ -axis. The various pulses and free-evolution periods  $\mathcal{F}(t)$  are chosen such that the output-state projection  $\langle \hat{Z}_a \mathcal{U} \rangle_0$  is proportional only to terms in  $\mathcal{L}_{\text{free}}$  which scale anti-symmetrically with  $\cos \theta_{in}$ , namely those due to resonant dipole-dipole interactions.

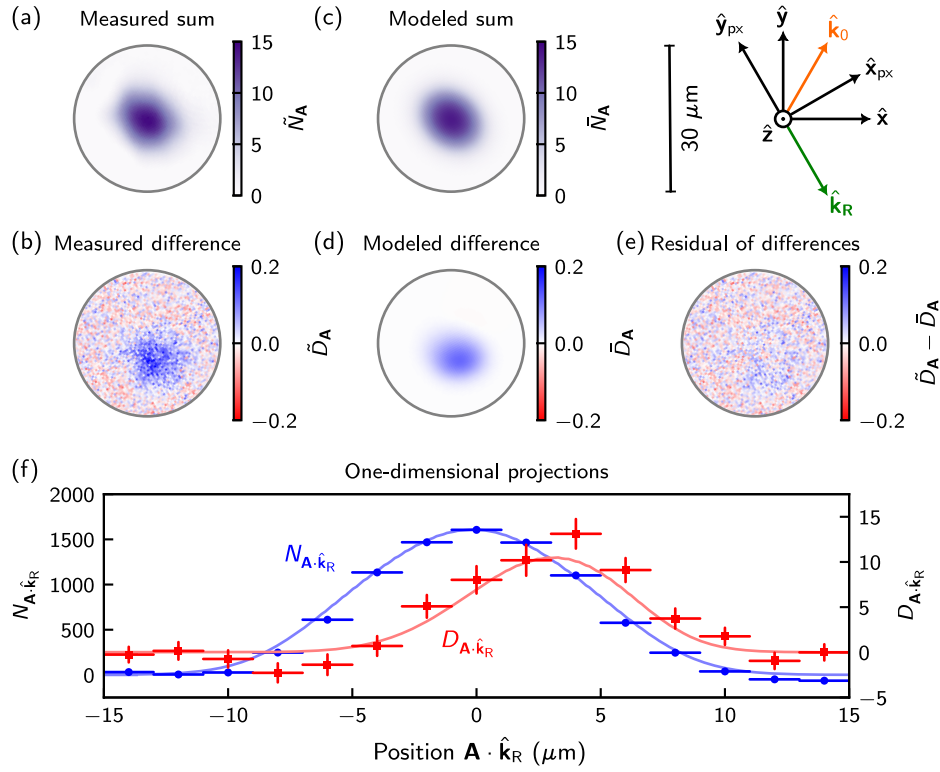


Figure 5.6: Imaging cooperative Lamb shifts at  $\psi = \psi_{\text{res}} = 29.5(5)^\circ$ ,  $\cos\theta_{\text{in}} = \pm 1/\sqrt{2}$  and  $q = 0$ . Differences in the measured spatial profiles of the sum  $\tilde{N}_A$  (a) and difference  $\tilde{D}_A$  (b) signals indicate the presence of long-range, anisotropic interactions which scale anti-symmetrically with  $\cos\theta_{\text{in}}$ . The maximum of  $\tilde{D}_A$  is spatially offset from the maximum of  $\tilde{N}_A$  due to constructive interference of the radiated fields along  $\hat{\mathbf{k}}_R = \mathbf{k}_0 - 2(\mathbf{k}_0 \cdot \hat{\mathbf{y}})\hat{\mathbf{y}}$ . The modeled signals  $\tilde{N}_A$  (c) and  $\tilde{D}_A$  (d) show qualitative agreement with the measured signals upon visual inspection. The residuals of the subtraction  $\tilde{D}_A - \bar{D}_A$  are shown in (e). The modeled signals are obtained by fitting  $\tilde{N}_A$  to a Fermi-Dirac distribution and contain no other free parameters. (f) One-dimensional projections  $I_{\mathbf{A} \cdot \hat{\mathbf{k}}_R}$  of the above signals are obtained by projecting the images  $I_{\mathbf{A}}$  in panels (a-d) onto  $\hat{\mathbf{k}}_R$ , *i.e.*  $I_{\mathbf{A} \cdot \hat{\mathbf{k}}_R} = \sum_{\mathbf{A}' \parallel (\mathbf{A} \cdot \hat{\mathbf{k}}_R) \hat{\mathbf{k}}_R} I_{\mathbf{A}'}$ . The data points display the measured signals with  $\tilde{N}_A$  as blue circles and  $\tilde{D}_A$  as red squares. Vertical error bars represent  $1\sigma$  standard errors and horizontal bars show the  $2 \mu\text{m}$  bin-width of the projections onto  $\hat{\mathbf{k}}_R$ . The red (blue) solid line shows the modeled signal  $\tilde{N}_{\mathbf{A} \cdot \hat{\mathbf{k}}_R}$  ( $\tilde{D}_{\mathbf{A} \cdot \hat{\mathbf{k}}_R}$ ).

$q = 0$ ,  $\cos(\theta) = \pm 1/\sqrt{2}$  and  $\psi = \psi_{\text{res.}} = 29.5^\circ$ .

Fig. 5.7 displays the ensemble-averaged Lamb shifts as functions of both  $\theta_{\text{in}}$  and  $\psi$ , again showing accurate modeling of the observed shifts.

For the resonant angle-of-incidence, clock shifts are easily large enough to produce clock shifts significant as compared to the  $\delta\nu/\nu = 10^{-18}$  level. Fig. 5.8 shows the shift uncertainty as a function of averaging time in determining the collective Lamb shift  $\delta \approx -1.5(7) \times 10^{-19}$  for  $q = 0$ ,  $\psi = \psi_{\text{res}}$  and  $\theta_{\text{in}} \rightarrow 0$ . For the normal angle of incidence, all shifts are consistent with zero at the  $10^{-19}$ -level. We then may conclude that collective Lamb shifts are unlikely to contribute significant systematic shifts for at least the next decade in clock accuracy. It is interesting to note that these shifts should naturally be at an order of magnitude larger in ytterbium-171 atomic clocks where the excited clock state lifetime is correspondingly shorter, and beyond leading order in  $\Gamma t$  effects can easily become significant.

### 5.3 Future directions

While we have demonstrated a quantitative understanding of leading-order resonant dipole-dipole interactions in an cubic lattice optical atomic clock, there is much more work to be done in the context of long-time dynamics [93, 99, 103], It seems that significant engineering of trapping potentials must be done in order to access timescales  $\Gamma t \sim 1$  without Raman scattering of lattice photons destroying the atomic coherences. It is thus interesting to consider probing other atomic transitions with significantly shorter excited state lifetimes as a proxy.

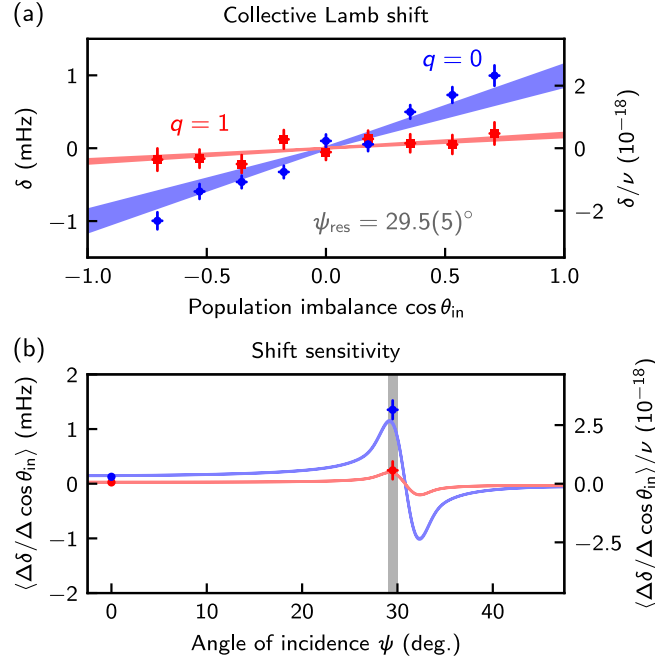


Figure 5.7: Controlling cooperative Lamb shifts. (a) Scaling of the ensemble-averaged shift  $\delta$  versus the initial spin projection  $\cos \theta_{in}$  for  $\psi = \psi_{res}$  and both  $q = 0$  (blue) and  $q = 1$  (red). Data points show the measured shifts  $\tilde{\delta}$  with vertical error bars representing  $1\sigma$  standard errors and horizontal error bars representing 2% observed fluctuations in the initial pulse area  $\theta_{in}$ . Shaded regions show the modeled shifts  $\bar{\delta}$ , propagating the experimental uncertainty in  $\psi_{res}$ . (b) Angle of incidence dependence of the shift sensitivity to changes in the initial spin projection. The vertical gray bar represents the angle of incidence used in (a).

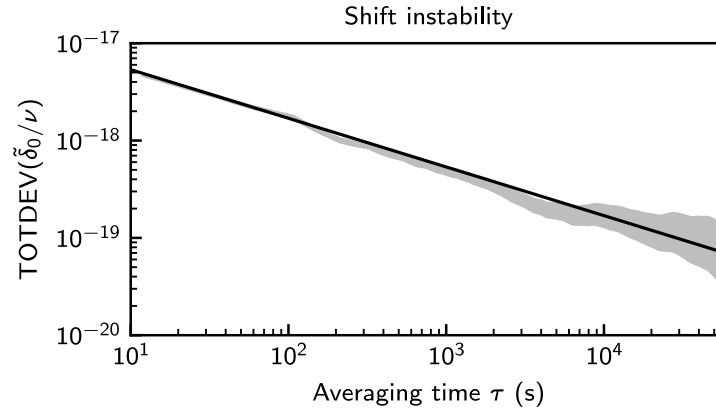


Figure 5.8: Instability of cooperative Lamb shift measurement. The shaded gray region shows the  $1\sigma$  confidence interval of the total deviation [102] of the clock shift  $\tilde{\delta}_0/\nu$  for the resonant angle of incidence as a function of averaging time  $\tau$ . The black line shows a fit to the data for  $\tau < 100$  s, assuming a white noise floor, giving an inferred instability of  $1.7 \times 10^{-17}/\sqrt{\text{Hz}}$ .

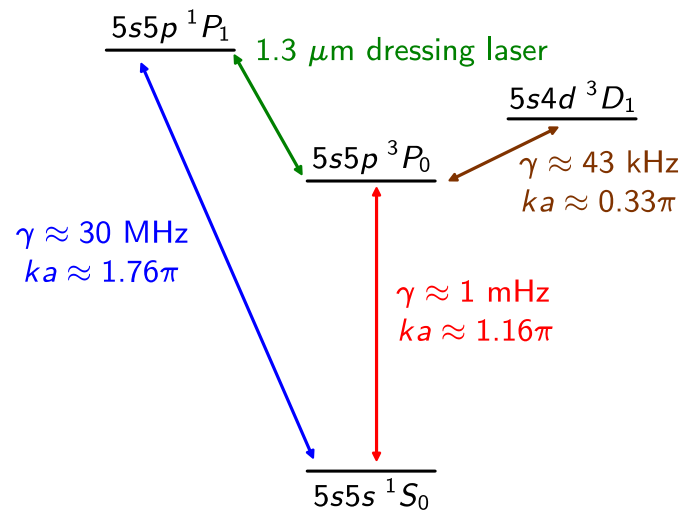


Figure 5.9: Enhancing resonant dipole-dipole interactions. Shown are two electronic levels relevant to future studies of the dynamics of resonant dipole-dipole interactions in the long-time limit. While probing long-time dynamics  $\gamma_{eg}t \sim 1$  seems presently challenging on the strontium-87 clock transition due to Raman scattering of optical lattice photons limiting coherence times to the 10 s-level, there are additional electronic states with significantly shorter excited state lifetimes which can be probed. One particularly attractive transition is the  $5s5p\ ^3P_0 \leftrightarrow 5s4d\ ^3D_1$  transition at 115 THz. Given the relatively long transition wavelength  $ka \approx \pi/3$ , coherent interactions can be significantly dominant over single-particle decay rates. Or alternatively, optically dressing the excited clock state with the  $5s5p\ ^1P_1$  level opens up the possibility of being able to dynamically tune dipole-dipole coupling strengths (1 mHz – 1 Hz) with modest optical powers ( $\mathcal{O}(5\ \text{mW})$ ).

## Chapter 6

### Conclusion

So what does this all mean for the future of atomic clocks? While one wants to simultaneously interrogate multiple atoms while also maintaining the notion that each atom acts as if it were a single particle floating forever in free space, the very fact that one can interact with an atom also means that atoms can also interact amongst themselves. The future of atomic clocks is then to peel back, layer-by-layer, all the implications of the light-matter interaction  $\hat{H}_1$ .

Previous generations of optical lattice clocks found limitations to both achievable coherence times and accuracy due to contact interactions between atoms within shared lattice sites. While these effects can be sufficiently mitigated by ever increasing the mode volume of the optical traps, one is then forced to sample ever larger inhomogeneities of external perturbations.

This thesis has described how three-dimensional optical lattices offer a promising alternative in eliminating the deleterious effects of contact interactions. In Ch. 2-3 we described how contact interactions are effectively eliminated by carefully controlling the external degrees of freedom of an atomic gas in order to prepare a single-spin-component band insulator of  $\mathcal{O}(10^4)$  atoms in the atomic limit with peak filling fractions exceeding 90%, and inter-site tunneling rates below 1 mHz. By making significant advances in the preparation of degenerate Fermi gases, we demonstrated the ability to achieve duty-cycles of coherent-interrogation times to those of state-preparation greater than 50%, the required threshold for which two identical clocks operating in an anti-synchronous fashion become immune to local-oscillator noise. Furthermore, we demonstrated how spatially resolving spectroscopic signals can be an incredibly powerful tool for determining systematic effects.

In Ch. 4 we discussed how the interplay between Raman scattering in deep optical lattices and tunneling induced dephasing in shallow optical lattices, requires a modification of the trapping potentials in order to further improve optical coherence times. Our proposal to increase the spatial separation between lattice sites has subsequently been realized in optical tweezer arrays containing hundreds of atoms to great success, and dynamically adjustable optical lattices seem to be a realistic upgrade to the presented apparatus, potentially enabling coherent interrogation of tens-of-thousands of atoms on timescales as long as the excited clock state's nearly two minute natural lifetime.

In Ch. 5, the spectroscopic imaging technique was used to observe clock shifts due to collective light-matter interactions intrinsic to the finite (though very small) electric dipole moment of the clock transition. The magnitude of these cooperative Lamb shifts was shown to be highly sensitive to controllable experimental parameters, such that they could be made resonantly enhanced or undetectably small. While cooperative Lamb shifts in non-resonant geometries scale with the atomic density on timescales short as compared to the spontaneous emission rate  $\gamma_{eg}t \ll 1$ , one generically expects the  $1/r$  far-field interactions to result in shifts scaling with system size at longer coherent evolution times [103]. Anticipating continued improvements in achievable sensitivities of this and other optical clock experiments, it then is worth considering if these interactions will impose some limit on maximally feasible system sizes for the cubic lattice clock, or, more generally, any atomic clock? Perhaps there are at least a few strategies worth discussing in terms of the more immediate future, before speculating more on potential fundamental limits.

One strategy involves our proposal in Ch. 4 regarding lattice spacings matched to the clock photon wavelength, which we might refer to as a "Bragg lattice" for brevity. As described in Ch. 5 it turned out that operating the clock exactly at Bragg resonance should result in ensemble-averaged shifts equal to zero (while slight deviations from resonance lead to dramatically enhanced shifts). This is somewhat of a fortuitous situation, lattice constants satisfying  $k_{\text{clk}}a_{\text{B}} = 2\pi$  are doubly motivated! Fig. 6.1 shows that leading order cooperative Lamb shifts can be made asymptotically zero (for  $\Gamma t \ll 1$ ) in a Bragg lattice, given the lattice constant in the directions transverse to the probe laser deviate slightly from exact resonance  $|a_{\perp}/a_{\text{B}} - 1| \ll 1$ . In addition to negating the cooperative shifts, cooperative decay

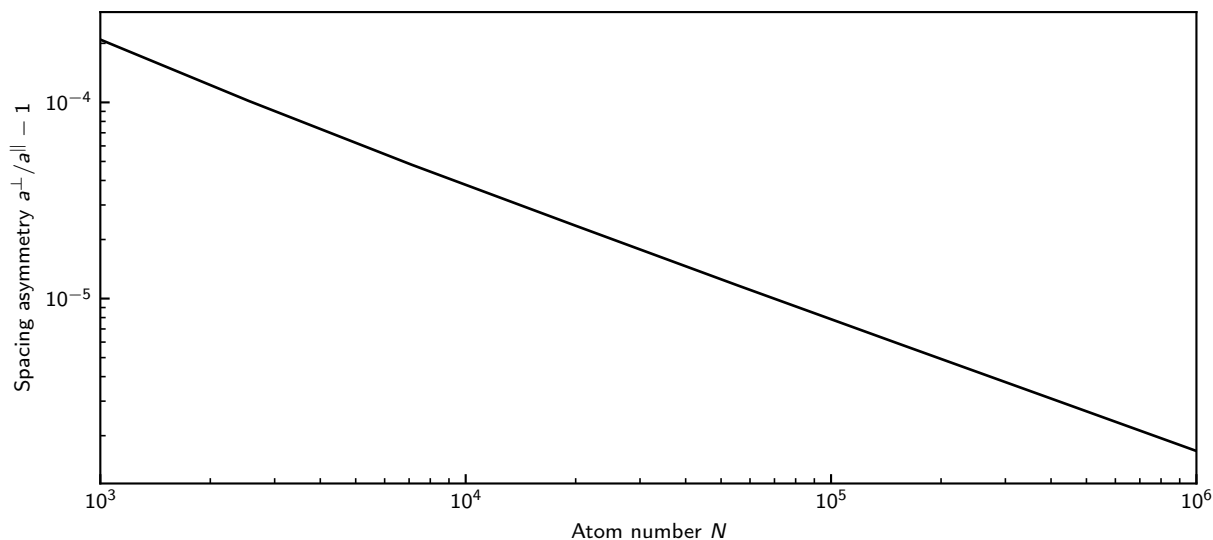


Figure 6.1: Zeroing leading order cooperative Lamb shifts in cubic “Bragg” lattice. In a cubic lattice where both the transverse ( $a_{\perp}$ ) and longitudinal ( $a_{\parallel}$ ) lattice constants are matched to the clock photon wavelength  $k_{\text{clock}}a_{\parallel} = k_{\text{clock}}a_{\perp} = 2\pi$ , the leading order corrections to the mean clock frequency and decay rate are zero, given the transverse lattice spacings deviate slightly from the exact Bragg condition:  $a_{\perp}/a_{\parallel} < 1$ . The required asymmetry asymptotically approaches 1 with increasing system size.

rates should also be asymptotically equal to single-atom spontaneous emission rates.

Another option moving forward could involve choosing clock states with significantly reduced, or even vanishingly small intrinsic couplings via the electromagnetic field. For instance, bosonic isotopes of alkaline-earth(-like) atoms have no nuclear spin and thus all single-photon transitions  $J = 0 \rightarrow J' = 0$  are strictly forbidden in the absence of external perturbations, e.g. a magnetic bias field, or optical state dressing. One might then envision an optical clock operating much like what was proposed in Ref. [104] where a coherent superposition between the two clock states can be manipulated via two-photon transitions before the coupling is turned off during the free-evolution period. Then, to second order in the light-atom coupling  $\hat{H}_1$ , the atoms should evolve as independent systems. But of course there are higher-order effects!

In Ch. 2, we found the van der Waals interaction  $U_{ij}^{\text{vdW}} = C_{ij}^{(6)}/r_{ij}^6$  appearing at fourth order in the coupling  $\hat{H}_1$ . While this (plus additional Coulomb interactions at shorter ranges) could be replaced, in the low-energy limit, by a pseudo contact interaction when describing atoms with spatially overlapped distributions, this approximation fails to capture the interaction when the spatial overlap is vanishingly small. Fig. 6.2 shows the van der Waals interaction energy experienced by an atom in both clock states, due to the presence of an additional atom in the same internal state, as a function of the inter-atomic separation. It turns out that, in the case of the retro-reflected cubic optical lattice, van der Waals interactions should correspond to clock shifts at the  $100 \mu\text{Hz}$  ( $10^{-19}$ ) level. The strong dependence on separation results in the shift being suppressed by a factor of 30 for the Bragg lattice as compared to the retro lattice. It is also worth noting that the interaction energies are independent of the clock transition dipole moment, rather it is dominated all dipole allowed transitions out of either clock state. This then motivates the use of atomic species with small DC polarizabilities, which is consistent with what one wants in minimizing clock shifts from black body radiation.

It is also worth discussing what more can be done with regards to studying resonant dipole-dipole interactions in periodic arrays as interesting many-body systems in their own right. The data presented in Ch. 5 demonstrated that atoms act much like classical dipoles in the  $\Gamma t \ll 1$  limit. Uniquely quantum mechanical effects become significant only for long interrogation times  $\Gamma t \sim 1$ . It has long

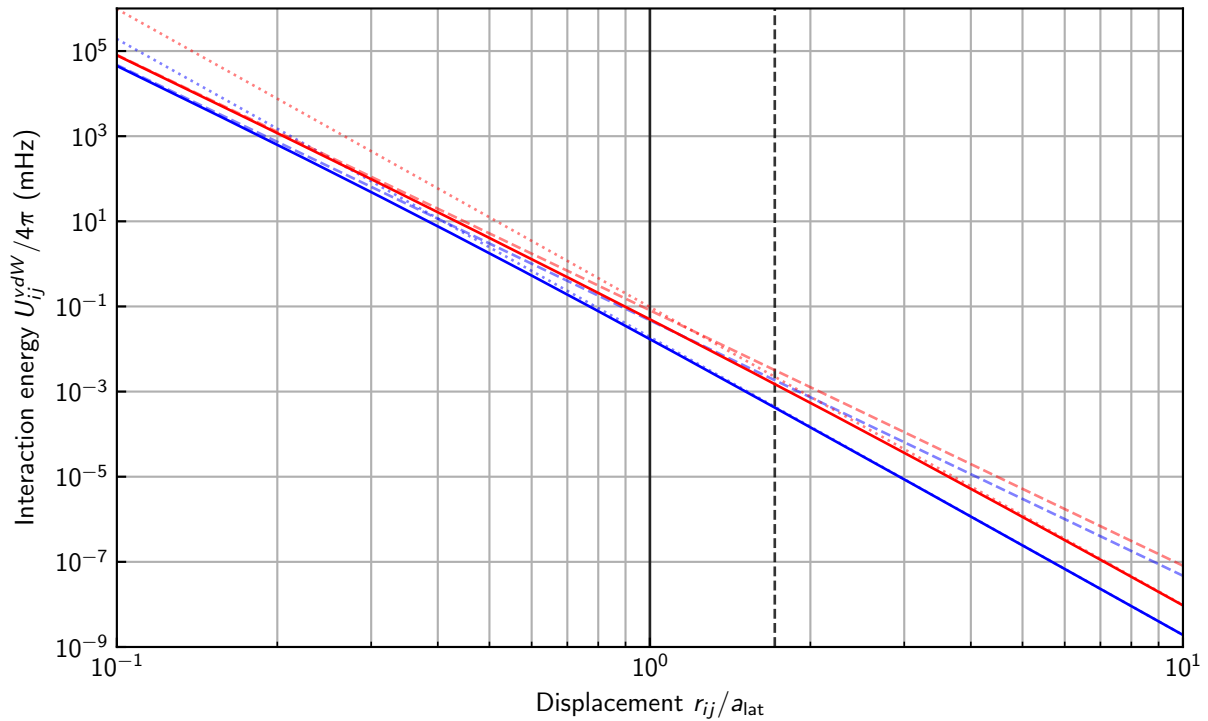


Figure 6.2: Van der Waals interaction energies at finite inter-atomic separation. Using the transition energies and natural decay rates in Tab. 2.1-2.2, in order to solve Eq. 2.31 beyond the near-field limit, the interaction energy experienced by a strontium atom in either clock state, due to the presence of a second, identical atom at separated by a distance  $r_{ij}$  which we have normalized by the retroreflected lattice constant  $a_0 \approx 407$  nm. The Solid lines show the full, analytic solutions for both atoms in the ground (blue) and excited (red) states, while the dashed (dotted) lines show the  $r_{ij}^{-6}$  ( $r_{ij}^{-7}$ ) asymptotics in the near-field (far-field) limit. The vertical solid (dashed) line shows the mean displacement of nearest neighbors for a retro-reflected (Bragg) lattice.

been predicted that a two-level atom spontaneously emitting into a vacuum will exhibit non-exponential decay at sufficiently long times [105]. The timescale at which this behavior is to be expected is set by the relation  $(2\pi\omega_{eg}/\gamma_{eg})^2(\omega_{eg}t)^4 \exp(-\gamma_{eg}t) \sim 1$  which for the strontium-87 clock transition occurs at  $\gamma_{eg}t \approx 267$  corresponding to an excited state survival probability of  $\exp(-\gamma_{eg}t) \approx 10^{-117}$ , far beyond modern experimental detectability. However, there appears to be numerical evidence that ordered arrays of atoms might exhibit similar effects on significantly shorter time scales [99]. Practically speaking, it seems that dressing the excited clock state with either the  $5s5p\ ^1P_1$  or  $5s4d\ ^3D_1$  states could enable coherent evolution times long enough to observe manifestly quantum dynamics in the current apparatus.

The coherent interactions generated by the dipole-dipole couplings also provide opportunities to generate interesting many-body states. The Hermitian part of the evolution  $\hat{H}_{dd} = \sum_{ij} V_{ij} \hat{S}_{eg}^{(i)} \hat{S}_{ge}^{(j)}$  takes the form of an  $XX + YY \sim SS - ZZ$  interaction which is known to generate spin squeezing [106, 107]. In order for the entanglement to be meterologically useful, the coherent interactions must be dominant  $\text{Re}(V_{ij}) \gg \text{Im}(V_{ij})$  which can be achieved for sub-wavelength lattice spacings  $ka \ll 2\pi$  making the  $5s5p\ ^3P_0 \leftrightarrow 5s4d\ ^3D_1$  particularly attractive.

All together, it seems hard to imagine that the community is anywhere near approaching a hard limit to the ultimate precision of atomic clocks, but rather faces an exciting journey in probing ever deeper into the jungle of light matter interactions.

## Bibliography

- [1] M. A. Lombardi, *IEEE Instrumentation & Measurement Magazine* **14**, 45 (2011).
- [2] L. Essen and J. V. L. Parry, *Nature* **176**, 280 (1955).
- [3] T. Andreae, W. König, R. Wynands, D. Leibfried, F. Schmidt-Kaler, C. Zimmermann, D. Meschede, and T. W. Hänsch, *Phys. Rev. Lett.* **69**, 1923 (1992).
- [4] S. A. Diddams, T. Udem, J. C. Bergquist, E. A. Curtis, R. E. Drullinger, L. Hollberg, W. M. Itano, W. D. Lee, C. W. Oates, K. R. Vogel, and D. J. Wineland, *Science* **293**, 825 (2001), <https://www.science.org/doi/pdf/10.1126/science.1061171> .
- [5] B. J. Bloom, T. L. Nicholson, J. R. Williams, S. L. Campbell, M. Bishof, X. Zhang, W. Zhang, S. L. Bromley, and J. Ye, *Nature* **506**, 71 (2014).
- [6] T. L. Nicholson, S. L. Campbell, R. B. Hutson, G. E. Marti, B. J. Bloom, R. L. McNally, W. Zhang, M. D. Barrett, M. S. Safronova, G. F. Strouse, W. L. Tew, and J. Ye, *Nature Communications* **6**, 6896 (2015).
- [7] W. F. McGrew, X. Zhang, R. J. Fasano, S. A. Schäffer, K. Beloy, D. Nicolodi, R. C. Brown, N. Hinkley, G. Milani, M. Schioppo, T. H. Yoon, and A. D. Ludlow, *Nature* **564**, 87 (2018).
- [8] S. M. Brewer, J.-S. Chen, A. M. Hankin, E. R. Clements, C. W. Chou, D. J. Wineland, D. B. Hume, and D. R. Leibbrandt, *Phys. Rev. Lett.* **123**, 033201 (2019).
- [9] T. Bothwell, D. Kedar, E. Oelker, J. M. Robinson, S. L. Bromley, W. L. Tew, J. Ye, and C. J. Kennedy, *Metrologia* **56**, 065004 (2019).
- [10] T. P. Heavner, E. A. Donley, F. Levi, G. Costanzo, T. E. Parker, J. H. Shirley, N. Ashby, S. Barlow, and S. R. Jefferts, *Metrologia* **51**, 174 (2014).
- [11] P. H. Boucheron, *The Bulletin of the National Association of Watch and Clock Collectors* **27**, 165 (1985).
- [12] W. F. Snyder, *IEEE Transactions on Instrumentation and Measurement* **22**, 99 (1973).
- [13] H. Dehmelt, *Physica Scripta* **1988**, 102 (1988).
- [14] W. M. Itano, J. C. Bergquist, J. J. Bollinger, J. M. Gilligan, D. J. Heinzen, F. L. Moore, M. G. Raizen, and D. J. Wineland, *Phys. Rev. A* **47**, 3554 (1993).

- [15] R. N. F., Molecular Beams (Oxford University Press, Oxford, 1956).
- [16] M. A. Kasevich, E. Riis, S. Chu, and R. G. DeVoe, *Phys. Rev. Lett.* **63**, 612 (1989).
- [17] C. A., G. S., S. G., L. Ph., L. S., B. M., S. E., W. S., and S. K., Proceedings of the 5th Symposium on Frequency Standards and Metrology (World Scientific, Singapore, 1996) pp. 49–59.
- [18] S. Jefferts, D. Meekhof, L. Hollberg, D. Lee, R. Drullinger, F. Walls, C. Nelson, F. Levi, and T. Parker, in Proceedings of the 1998 IEEE International Frequency Control Symposium (Cat. No.98CH36165) (1998) pp. 2–5.
- [19] J. Reichert, M. Niering, R. Holzwarth, M. Weitz, T. Udem, and T. W. Hänsch, *Phys. Rev. Lett.* **84**, 3232 (2000).
- [20] D. J. Jones, S. A. Diddams, J. K. Ranka, A. Stentz, R. S. Windeler, J. L. Hall, and S. T. Cundiff, *Science* **288**, 635 (2000), <https://www.science.org/doi/pdf/10.1126/science.288.5466.635> .
- [21] J. C. Hafele and R. E. Keating, *Science* **177**, 168 (1972), <https://www.science.org/doi/pdf/10.1126/science.177.4044.168> .
- [22] C. W. Chou, D. B. Hume, T. Rosenband, and D. J. Wineland, *Science* **329**, 1630 (2010), <https://www.science.org/doi/pdf/10.1126/science.1192720> .
- [23] T. Bothwell, C. J. Kennedy, A. Aeppli, D. Kedar, J. M. Robinson, E. Oelker, A. Staron, and J. Ye, *Nature* **602**, 420 (2022).
- [24] M. J. Martin, M. Bishof, M. D. Swallows, X. Zhang, C. Benko, J. von Stecher, A. V. Gorshkov, A. M. Rey, and J. Ye, *Science* **341**, 632 (2013), <https://www.science.org/doi/pdf/10.1126/science.1236929> .
- [25] M. Bishof, M. J. Martin, M. D. Swallows, C. Benko, Y. Lin, G. Quéméner, A. M. Rey, and J. Ye, *Phys. Rev. A* **84**, 052716 (2011).
- [26] M. D. Swallows, M. Bishof, Y. Lin, S. Blatt, M. J. Martin, A. M. Rey, and J. Ye, *Science* **331**, 1043 (2011), <https://www.science.org/doi/pdf/10.1126/science.1196442> .
- [27] G. K. Campbell, M. M. Boyd, J. W. Thomsen, M. J. Martin, S. Blatt, M. D. Swallows, T. L. Nicholson, T. Fortier, C. W. Oates, S. A. Diddams, N. D. Lemke, P. Naidon, P. Julienne, J. Ye, and A. D. Ludlow, *Science* **324**, 360 (2009), <https://www.science.org/doi/pdf/10.1126/science.1169724> .
- [28] J. A. Muniz, D. J. Young, J. R. K. Cline, and J. K. Thompson, *Phys. Rev. Res.* **3**, 023152 (2021).
- [29] T. Middelmann, S. Falke, C. Lisdat, and U. Sterr, *Phys. Rev. Lett.* **109**, 263004 (2012).
- [30] K. Kim, A. Aeppli, T. Bothwell, and J. Ye, *Phys. Rev. Lett.* **130**, 113203 (2023).
- [31] S. L. Campbell, R. B. Hutson, G. E. Marti, A. Goban, N. Darkwah Oppong, R. L. McNally, L. Sonderhouse, J. M. Robinson, W. Zhang, B. J. Bloom, and J. Ye, *Science* **358**, 90 (2017).
- [32] S. L. Campbell, A Fermi-degenerate three-dimensional optical lattice clock, Ph.D. thesis, University of Colorado (2017).

- [33] G. E. Marti, R. B. Hutson, A. Goban, S. L. Campbell, N. Poli, and J. Ye, *Phys. Rev. Lett.* **120**, 103201 (2018).
- [34] L. Sonderhouse, C. Sanner, R. B. Hutson, A. Goban, T. Bilitewski, L. Yan, W. R. Milner, A. M. Rey, and J. Ye, *Nature Physics* **16**, 1216 (2020).
- [35] L. Sonderhouse, Quantum gas engineering for atomic clocks, Ph.D. thesis, University of Colorado (2021).
- [36] W. R. Milner, L. Yan, R. B. Hutson, C. Sanner, and J. Ye, High-fidelity imaging of a band insulator in a three-dimensional optical lattice clock (2023).
- [37] H. A. Bethe, *Phys. Rev.* **72**, 339 (1947).
- [38] W. E. Lamb and R. C. Retherford, *Phys. Rev.* **72**, 241 (1947).
- [39] T. A. Welton, *Phys. Rev.* **74**, 1157 (1948).
- [40] M. S. Safronova, M. G. Kozlov, W. R. Johnson, and D. Jiang, *Phys. Rev. A* **80**, 012516 (2009).
- [41] D. G. Matei, T. Legero, S. Häfner, C. Grebing, R. Weyrich, W. Zhang, L. Sonderhouse, J. M. Robinson, J. Ye, F. Riehle, and U. Sterr, *Phys. Rev. Lett.* **118**, 263202 (2017).
- [42] E. Oelker, R. B. Hutson, C. J. Kennedy, L. Sonderhouse, T. Bothwell, A. Goban, D. Kedar, C. Sanner, J. M. Robinson, G. E. Marti, D. G. Matei, T. Legero, M. Giunta, R. Holzwarth, F. Riehle, U. Sterr, and J. Ye, *Nature Photonics* **13**, 714 (2019).
- [43] T. Curtright, D. Fairlie, and C. Zachos, A Concise Treatise on Quantum Mechanics in Phase Space (2016).
- [44] L. D. Landau and L. M. Lifshitz, Quantum Mechanics Non-Relativistic Theory, Third Edition: Volume 3, 3rd ed. (Butterworth-Heinemann, 1981).
- [45] G. F. Gribakin and V. V. Flambaum, *Phys. Rev. A* **48**, 546 (1993).
- [46] S. G. Porsev and A. Derevianko, *Journal of Experimental and Theoretical Physics* **102**, 195 (2006).
- [47] Y. N. Martinez de Escobar, P. G. Mickelson, P. Pellegrini, S. B. Nagel, A. Traverso, M. Yan, R. Côté, and T. C. Killian, *Phys. Rev. A* **78**, 062708 (2008).
- [48] A. Goban, R. B. Hutson, G. E. Marti, S. L. Campbell, M. A. Perlin, P. S. Julienne, J. P. D’Incao, A. M. Rey, and J. Ye, *Nature* **563**, 369 (2018).
- [49] X. Zhang, M. Bishof, S. L. Bromley, C. V. Kraus, M. S. Safronova, P. Zoller, A. M. Rey, and J. Ye, *Science* **345**, 1467 (2014), <https://www.science.org/doi/pdf/10.1126/science.1254978> .
- [50] T. Busch, B.-G. Englert, K. Rzazewski, and M. Wilkens, *Foundations of Physics* **28**, 549 (1998).
- [51] D. Blume and C. H. Greene, *Phys. Rev. A* **65**, 043613 (2002).
- [52] V. V. Flambaum, G. F. Gribakin, and C. Harabati, *Phys. Rev. A* **59**, 1998 (1999).
- [53] P. R. Johnson, E. Tiesinga, J. V. Porto, and C. J. Williams, *New Journal of Physics* **11**, 093022 (2009).

- [54] M. A. Perlin and A. M. Rey, *New Journal of Physics* **21**, 043039 (2019).
- [55] A. Aeppli, A. Chu, T. Bothwell, C. J. Kennedy, D. Kedar, P. He, A. M. Rey, and J. Ye, *Science Advances* **8**, eadc9242 (2022), <https://www.science.org/doi/pdf/10.1126/sciadv.adc9242> .
- [56] P. He, M. A. Perlin, S. R. Muleady, R. J. Lewis-Swan, R. B. Hutson, J. Ye, and A. M. Rey, *Phys. Rev. Res.* **1**, 033075 (2019).
- [57] M. Mamaev, I. Kimchi, R. M. Nandkishore, and A. M. Rey, *Phys. Rev. Res.* **3**, 013178 (2021).
- [58] M. A. Perlin, D. Barberena, M. Mamaev, B. Sundar, R. J. Lewis-Swan, and A. M. Rey, *Phys. Rev. A* **105**, 023326 (2022).
- [59] M. Mamaev, T. Bilitewski, B. Sundar, and A. M. Rey, *PRX Quantum* **3**, 030328 (2022).
- [60] R. B. Hutson, A. Goban, G. E. Marti, L. Sonderhouse, C. Sanner, and J. Ye, *Phys. Rev. Lett.* **123**, 123401 (2019).
- [61] H. Katori, M. Takamoto, V. G. Pal'chikov, and V. D. Ovsiannikov, *Phys. Rev. Lett.* **91**, 173005 (2003).
- [62] H. Uys, M. J. Biercuk, A. P. VanDevender, C. Ospelkaus, D. Meiser, R. Ozeri, and J. J. Bollinger, *Phys. Rev. Lett.* **105**, 200401 (2010).
- [63] S. Kolkowitz, S. L. Bromley, T. Bothwell, M. L. Wall, G. E. Marti, A. P. Koller, X. Zhang, A. M. Rey, and J. Ye, *Nature* **542**, 66 (2017).
- [64] S. L. Bromley, S. Kolkowitz, T. Bothwell, D. Kedar, A. Safavi-Naini, M. L. Wall, C. Salomon, A. M. Rey, and J. Ye, *Nature Physics* **14**, 399 (2018).
- [65] M. A. Norcia, A. W. Young, W. J. Eckner, E. Oelker, J. Ye, and A. M. Kaufman, *Science* **366**, 93 (2019), <https://www.science.org/doi/pdf/10.1126/science.aay0644> .
- [66] A. W. Young, W. J. Eckner, W. R. Milner, D. Kedar, M. A. Norcia, E. Oelker, N. Schine, J. Ye, and A. M. Kaufman, *Nature* **588**, 408 (2020).
- [67] A. L. Shaw, R. Finkelstein, R. B.-S. Tsai, P. Scholl, T. H. Yoon, J. Choi, and M. Endres, Multi-ensemble metrology by programming local rotations with atom movements (2023), [arXiv:2303.16885 \[quant-ph\]](https://arxiv.org/abs/2303.16885) .
- [68] R. Jördens, N. Strohmaier, K. Günter, H. Moritz, and T. Esslinger, *Nature* **455**, 204 (2008).
- [69] S. Dörscher, R. Schwarz, A. Al-Masoudi, S. Falke, U. Sterr, and C. Lisdat, *Phys. Rev. A* **97**, 063419 (2018).
- [70] P. Lemonde and P. Wolf, *Phys. Rev. A* **72**, 033409 (2005).
- [71] M. Glück, F. Keck, A. R. Kolovsky, and H. J. Korsch, *Phys. Rev. Lett.* **86**, 3116 (2001).
- [72] R. H. Dicke, *Phys. Rev.* **93**, 99 (1954).
- [73] Fain, *JETP* **9**, 562 (1959).
- [74] R. Friedberg, S. Hartmann, and J. Manassah, *Physics Reports* **7**, 101 (1973).

- [75] N. Skribanowitz, I. P. Herman, J. C. MacGillivray, and M. S. Feld, *Phys. Rev. Lett.* **30**, 309 (1973).
- [76] M. Gross, C. Fabre, P. Pillet, and S. Haroche, *Phys. Rev. Lett.* **36**, 1035 (1976).
- [77] M. Gross, P. Goy, C. Fabre, S. Haroche, and J. M. Raimond, *Phys. Rev. Lett.* **43**, 343 (1979).
- [78] D. Pavolini, A. Crubellier, P. Pillet, L. Cabaret, and S. Liberman, *Phys. Rev. Lett.* **54**, 1917 (1985).
- [79] P. V. Zinov'ev, S. V. Lopina, Y. V. Naboikin, M. B. Silaeva, V. V. Samartsev, and Y. E. Sheibut, *JETP* **58**, 1129 (1983).
- [80] O. P. Varnavskii, A. N. Kirkin, A. M. Leontovich, R. F. Malikov, A. M. Mozharovskii, and E. D. Trifonov, *JETP* **59**, 716 (1984).
- [81] R. G. DeVoe and R. G. Brewer, *Phys. Rev. Lett.* **76**, 2049 (1996).
- [82] M. D. Barnes, P. S. Krstic, P. Kumar, A. Mehta, and J. C. Wells, *Phys. Rev. B* **71**, 241303 (2005).
- [83] M. Scheibner, T. Schmidt, L. Worschech, A. Forchel, G. Bacher, T. Passow, and D. Hommel, *Nature Physics* **3**, 106 (2007).
- [84] A. Goban, C.-L. Hung, J. D. Hood, S.-P. Yu, J. A. Muniz, O. Painter, and H. J. Kimble, *Phys. Rev. Lett.* **115**, 063601 (2015).
- [85] B. H. McGuyer, M. McDonald, G. Z. Iwata, M. G. Tarallo, W. Skomorowski, R. Moszynski, and T. Zelevinsky, *Nature Physics* **11**, 32 (2015).
- [86] M. Houde, A. Mathews, and F. Rajabi, *Monthly Notices of the Royal Astronomical Society* **475**, 514 (2017).
- [87] W. R. Garrett, R. C. Hart, J. E. Wray, I. Datskou, and M. G. Payne, *Phys. Rev. Lett.* **64**, 1717 (1990).
- [88] R. Röhlsberger, K. Schlage, B. Sahoo, S. Couet, and R. Ruffer, *Science* **328**, 1248 (2010).
- [89] J. Keaveney, A. Sargsyan, U. Krohn, I. G. Hughes, D. Sarkisyan, and C. S. Adams, *Phys. Rev. Lett.* **108**, 173601 (2012).
- [90] A. F. van Loo, A. Fedorov, K. Lalumière, B. C. Sanders, A. Blais, and A. Wallraff, *Science* **342**, 1494 (2013).
- [91] Z. Meir, O. Schwartz, E. Shahmoon, D. Oron, and R. Ozeri, *Phys. Rev. Lett.* **113**, 193002 (2014).
- [92] G. Ferioli, A. Glicenstein, L. Henriët, I. Ferrier-Barbut, and A. Browaeys, *Phys. Rev. X* **11**, 021031 (2021).
- [93] D. E. Chang, J. Ye, and M. D. Lukin, *Phys. Rev. A* **69**, 023810 (2004).
- [94] H. Zoubi and H. Ritsch, *Phys. Rev. A* **83**, 063831 (2011).
- [95] S. D. Jenkins and J. Ruostekoski, *Phys. Rev. A* **86**, 031602 (2012).
- [96] D. E. Chang, L. Jiang, A. V. Gorshkov, and H. J. Kimble, *New Journal of Physics* **14**, 063003 (2012).

- [97] R. J. Bettles, S. A. Gardiner, and C. S. Adams, *Phys. Rev. A* **92**, 063822 (2015).
- [98] A. Asenjo-Garcia, M. Moreno-Cardoner, A. Albrecht, H. J. Kimble, and D. E. Chang, *Phys. Rev. X* **7**, 031024 (2017).
- [99] L. Henriet, J. S. Douglas, D. E. Chang, and A. Albrecht, *Phys. Rev. A* **99**, 023802 (2019).
- [100] J. Rui, D. Wei, A. Rubio-Abadal, S. Hollerith, J. Zeiher, D. M. Stamper-Kurn, C. Gross, and I. Bloch, *Nature* **583**, 369 (2020).
- [101] J. T. Manassah, *Physics Letters A* **374**, 1985 (2010).
- [102] D. Howe, *IEEE Transactions on Ultrasonics, Ferroelectrics, and Frequency Control* **47**, 1102 (2000).
- [103] A. Cidrim, A. Piñeiro Orioli, C. Sanner, R. B. Hutson, J. Ye, R. Bachelard, and A. M. Rey, *Phys. Rev. Lett.* **127**, 013401 (2021).
- [104] R. Santra, E. Arimondo, T. Ido, C. H. Greene, and J. Ye, *Phys. Rev. Lett.* **94**, 173002 (2005).
- [105] P. Knight and P. Milonni, *Physics Letters A* **56**, 275 (1976).
- [106] M. Kitagawa and M. Ueda, *Phys. Rev. A* **47**, 5138 (1993).
- [107] C. Qu and A. M. Rey, *Phys. Rev. A* **100**, 041602 (2019)

## Appendix A

### Symbolic conventions

symbol	definition
$\mathcal{H}(\hat{O})$	Hermitian part of operator $\hat{O}$ : $\mathcal{H}(\hat{O}) = \hat{O} + \text{H.c.}$
$\bar{\mathcal{H}}(\hat{O})$	Anti-Hermitian part of operator $\hat{O}$ : $\bar{\mathcal{H}}(\hat{O}) = i\hat{O} + \text{H.c.}$
$\mathcal{T}(\hat{O})$	Time integral of operator $\hat{O}$ : $\mathcal{T}(\hat{O}) = \int_{\tau}^0 dt' \hat{O}(t - t')$
$O_{ij,p}$	Quantity $O$ indexed by internal states $i$ and $j$ coupled by photonic mode $p$
$O_{eg,c}$	Quantity $O$ indexed by internal states $e$ (excited) and $g$ (ground) coupled by (coherent) photonic mode $c$
$\langle\langle O(\mathbf{r}, \mathbf{k}) \rangle\rangle$	Expectation value of quantity $O$ over phase-space variables $\mathbf{r}$ (position) and $\mathbf{k}$ (momentum)
$\langle \hat{O} \rangle$	Expectation value of operator $\hat{O}$
$\hat{P}_i$	Atomic projection operator onto state $i$
$\hat{N}_p$	Photonic number operator for mode $p$

Table A.1: Definitions of symbols used throughout the thesis.

## Appendix B

### Heating processes in optical traps

#### B.0.1 Time Dependent Perturbation Theory

We begin by assuming we can write a time dependent Hamiltonian in the specific form,

$$H(t) = H_0 + \epsilon(t)H', \quad (\text{B.1})$$

where the second term may be considered a perturbation about the first. Time evolution in the basis of eigenstates of  $H_0$ ,  $\psi_m$ , is then given by

$$i\hbar\partial_t\psi_m = \sum_n \epsilon(t)H'_{mn}e^{i\omega_{mn}t}\psi_n, \quad (\text{B.2})$$

which may be integrated to obtain

$$\psi_m(t) = -i\hbar^{-1} \sum_n H'_{mn} \int_0^t dt' \epsilon(t') e^{i\omega_{mn}t'} \psi_n. \quad (\text{B.3})$$

The rates at which the populations  $\rho_{mm} = |\psi_m|^2$  change in time are then

$$\frac{\Delta\rho_{mm}}{\Delta T} = \hbar^{-2} \sum_n |H'_{mn}|^2 \left[ \frac{1}{\Delta T} \int_0^{\Delta T} dt dt' \epsilon(t)\epsilon(t') e^{i\omega_{mn}(t-t')} \right] \rho_{nn} \quad (\text{B.4})$$

$$= \pi\hbar^{-2} \sum_n |H'_{mn}|^2 S_\epsilon(\omega_{mn}) \rho_{nn} \quad (\text{B.5})$$

$$\equiv \sum_n \Gamma_{mn} \rho_{nn} \quad (\text{B.6})$$

where we have identified  $S_\epsilon(\omega) = \frac{1}{\pi} \int_{-\Delta T}^{\Delta T} d\tau e^{i\omega\tau} \frac{1}{\Delta T} \int_0^{\Delta T} dt \epsilon(t)\epsilon(t+\tau)$  as the single sided power spectral density of fluctuations in  $\epsilon$ , assuming the interval  $\Delta T$  is long compared to the timescale over which  $\epsilon$  varies, yet short compared to that of changes in  $\rho_{mm}$ . As such, we are interested in calculating the quantities  $\Gamma_{mn} \equiv \pi\hbar^{-2}|H'_{mn}|^2 S_\epsilon(\omega_{mn})$  for experimentally relevant  $H_0$  and  $H'$

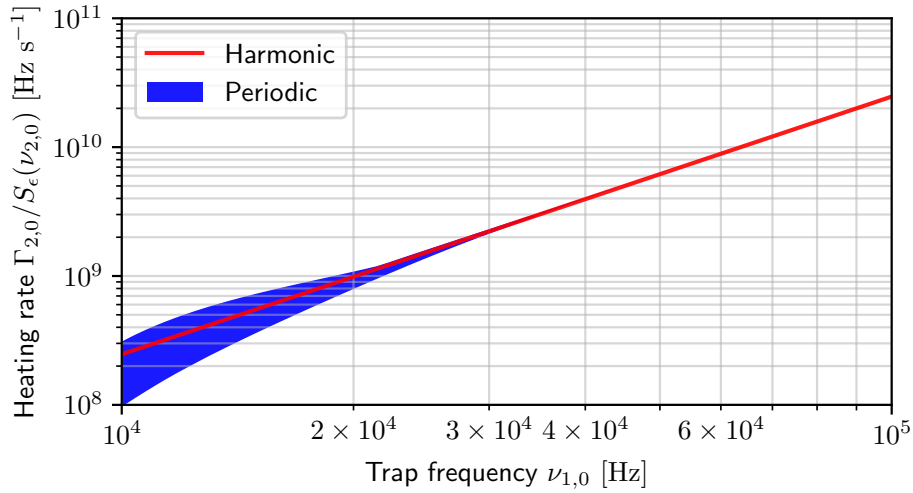


Figure B.1: Intensity noise-induced heating of  $^{87}\text{Sr}$  from ground to second excited states of Harmonic (red), and Periodic (blue) potentials. Rates are given as a function of first motional sideband frequency  $\nu_{1,0}$  and normalized by the power spectral density of relative intensity noise,  $S_\epsilon(\nu_{2,0})$  [ $\text{Hz}^{-1}$ ], evaluated at the second motional sideband frequency.

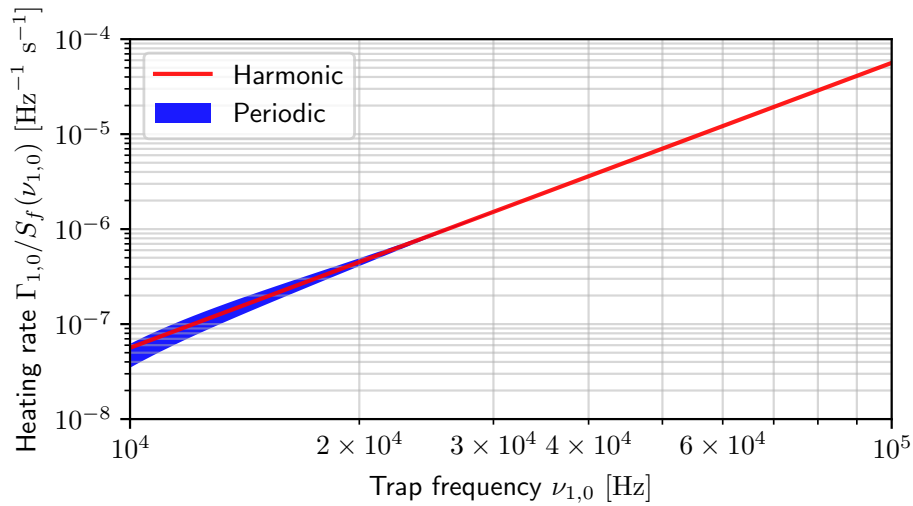


Figure B.2: Frequency noise-induced heating of  $^{87}\text{Sr}$  from ground to first excited states of Harmonic (red), and Periodic (blue) potentials. Rates are given as a function of first motional sideband frequency  $\nu_{1,0}$  and normalized by the power spectral density of laser frequency noise,  $S_f(\nu_{1,0})$  [ $\text{Hz}^{-1}$ ], evaluated at the first motional sideband frequency.

## B.0.2 Sinusoidal Potential

### B.0.2.1 Intensity Noise

We first consider the following scenario

$$H_0 = \frac{1}{2} \frac{p^2}{m} + V_0 \cos^2 kx, \quad H' = V_0 \cos^2 kx. \quad (\text{B.7})$$

Finding,

$$|H'_{mn}|^2 = V_0^2 \langle \cos^2 kx \rangle_{mn}^2 \quad (\text{B.8})$$

and

$$\Gamma_{mn} = \pi \frac{V_0^2}{\hbar^2} \langle \cos^2 kx \rangle_{mn}^2 S_\epsilon(\omega_{mn}) \quad (\text{B.9})$$

$$= 2\pi^2 \frac{V_0^2}{h^2} \langle \cos^2 kx \rangle_{mn}^2 S_\epsilon(\nu_{mn}) \quad (\text{B.10})$$

The elements  $\langle \cos^2 kx \rangle_{mn}^2$  must be computed numerically. The largest rate affecting ground band atoms,  $\Gamma_{2,0}$ , is plotted in Fig. B.1.

### B.0.2.2 Pointing Noise

We may also consider the following perturbation

$$H' = -kV_0 \sin 2kx \quad (\text{B.11})$$

whose squared elements are

$$|H'_{mn}|^2 = k^2 V_0^2 \langle \sin 2kx \rangle_{mn}^2 \quad (\text{B.12})$$

giving the following heating rates

$$\Gamma_{mn} = \pi \frac{V_0^2}{\hbar^2} \langle \sin 2kx \rangle_{mn}^2 k^2 S_\epsilon(\omega_{mn}) \quad (\text{B.13})$$

$$= 2\pi^2 \frac{V_0^2}{h^2} \langle \sin 2kx \rangle_{mn}^2 S_\phi(\nu_{mn}) \quad (\text{B.14})$$

where  $\phi = 2\pi(L + \epsilon)/\lambda$ .

### B.0.2.3 Frequency Noise

An infinitesimal change of the lattice laser's frequency,  $\delta f$ , is converted to phase noise via  $\delta\phi \approx 2\pi\frac{L}{c}\delta f$  where  $L$  is distance from the atoms to the phase reference. This gives

$$\Gamma_{mn} = 8\pi^4 \frac{V_0^2 L^2}{\hbar^2 c^2} \langle \sin 2kx \rangle_{mn}^2 S_f(\nu_{mn}) \quad (\text{B.15})$$

Again, the exact values of  $\langle \sin 2kx \rangle_{mn}$  must be computed numerically. The largest rate affecting ground band atoms in a  $L = 300$  mm lattice,  $\Gamma_{1,0}$ , is plotted in Fig. B.2.

## B.0.3 The Harmonic Limit

### B.0.3.1 Intensity Noise

The following scenario is numerically simpler and reasonably accurate for most experimentally relevant trapping frequencies,

$$H_0 = \frac{1}{2} \frac{p^2}{M} + \frac{1}{2} M\omega^2 x^2, \quad H' = \frac{1}{2} M\omega^2 x^2. \quad (\text{B.16})$$

Correspondingly,

$$|H'_{mn}|^2 = \frac{1}{4} M^2 \omega^4 \langle x^2 \rangle_{mn}^2 = \frac{1}{16} \hbar^2 \omega^2 \langle (a + a^\dagger)^2 \rangle_{mn}^2, \quad (\text{B.17})$$

and

$$\Gamma_{mn} = \frac{1}{16} \pi \omega^2 \langle (a + a^\dagger)^2 \rangle_{mn}^2 S_\epsilon(\omega_{mn}) \quad (\text{B.18})$$

$$= \frac{1}{8} \pi^2 \nu^2 \langle (a + a^\dagger)^2 \rangle_{mn}^2 S_\epsilon(\nu_{mn}). \quad (\text{B.19})$$

Specifically,

$$\Gamma_{2,0} = \frac{1}{4} \pi^2 \nu^2 S_\epsilon(2\nu) \quad (\text{B.20})$$

is plotted in Fig. B.1.

### B.0.3.2 Pointing Noise

Next,

$$H_0 = \frac{1}{2} \frac{p^2}{m} + \frac{1}{2} m\omega^2 x^2, \quad H' = m\omega^2 x. \quad (\text{B.21})$$

Gives

$$|H'_{mn}|^2 = m^2 \omega^4 \langle x \rangle_{mn}^2 = \frac{1}{2} \hbar m \omega^3 \langle a + a^\dagger \rangle_{mn}^2 \quad (\text{B.22})$$

and

$$\Gamma_{mn} = \frac{\pi \omega^3}{4 \omega_r} \langle a + a^\dagger \rangle_{mn}^2 k^2 S_\epsilon(\omega_{mn}) \quad (\text{B.23})$$

$$= \frac{\pi^2 \nu^3}{2 \nu_r} \langle a + a^\dagger \rangle_{mn}^2 S_\phi(\nu_{mn}) \quad (\text{B.24})$$

Where we have substituted  $\omega_r = \hbar k^2 / (2M)$ .

### B.0.3.3 Frequency Noise

As in the previous section on frequency noise, this is equivalent to

$$\Gamma_{mn} = 2\pi^4 \frac{\nu^3 L^2}{\nu_r c^2} \langle a + a^\dagger \rangle_{mn}^2 S_f(\nu_{mn}) \quad (\text{B.25})$$

In particular,

$$\Gamma_{1,0} = 2\pi^4 \frac{\nu^3 L^2}{\nu_r c^2} S_f(\nu_{1,0}) \quad (\text{B.26})$$

is plotted in is plotted in Fig. B.2.

ProQuest Number: 30631723

INFORMATION TO ALL USERS

The quality and completeness of this reproduction is dependent on the quality and completeness of the copy made available to ProQuest.



Distributed by ProQuest LLC (2023).

Copyright of the Dissertation is held by the Author unless otherwise noted.

This work may be used in accordance with the terms of the Creative Commons license or other rights statement, as indicated in the copyright statement or in the metadata associated with this work. Unless otherwise specified in the copyright statement or the metadata, all rights are reserved by the copyright holder.

This work is protected against unauthorized copying under Title 17, United States Code and other applicable copyright laws.

Microform Edition where available © ProQuest LLC. No reproduction or digitization of the Microform Edition is authorized without permission of ProQuest LLC.

ProQuest LLC  
789 East Eisenhower Parkway  
P.O. Box 1346  
Ann Arbor, MI 48106 - 1346 USA